EXPERIMENTAL ANALYSIS OF THE INTERACTION OF WATER WAVES WITH FLEXIBLE STRUCTURES

By

Dimitrios G. Stamos

a dissertation submitted to the faculty of

Virginia Polytechnic Institute and State University

in partial fulfillment of the requirements for the degree of

Doctor of Philosophy

in

Engineering Mechanics

Dr. D. P. Telionis, Co-Chairman

Dr. M. R. Hajj, Co-Chairman

Dr. R. H. Plaut

Dr. S. L. Hendricks

Dr. P. Diplas

May 2000

Blacksburg, Virginia

Experimental Analysis of the Interaction of Water Waves with Flexible Structures

Dimitrios G. Stamos

(ABSTRACT)

An experimental investigation of the interaction of water waves with flexible structures acting as breakwaters was carried out. Wave profiles, mapped out by water level measuring transducers, were studied to provide information on the performance of different breakwater models. A new signal analysis procedure for determining reflection coefficients based on wavelet theory was developed and compared to a conventional method. The reliability of using wavelet analysis to separate a partial standing wave into incident and reflected wave components was verified with a numerical example. It was also verified by the small variance in the estimates of the incident wave height from independent experimental measurements. Different geometries of rigid and flexible structures were constructed and examined. Reflection, transmission and energy loss coefficients were obtained over them. The influence of various properties of the models, such as the width and the internal pressure, on the effectiveness in reflecting or absorbing the incident wave energy was determined. Various factors which affect the performance of the breakwater, including the water depth, the wave length and the wave amplitude, were measured and documented. Suspended and bottom-mounted models were considered. The flow field over and near a hemi-cylindrical breakwater model was also examined using a flow visualization technique. An overall comparison among the models has also been provided. The results showed that the rectangular models, rigid and flexible, are the most effective structures to dissipate wave energy. The flow visualization technique indicated that the flow conforms with the circular geometry of a hemi-cylindrical breakwater model, yielding no flow separation.

Dedication

To the teachers who patiently transfer their knowledge to me all these years and

στη μνημη του θειου μου Ιωαννη Σταθοπουλου

Acknowledgments

First of all, my most sincere appreciation goes to Dr. Demetri Telionis and Dr. Muhammad Hajj, for sharing long working days, having many meaningful conversations and making deadlines less stressful. I also thank my dissertation committee members, Dr. Hendricks, Dr. Plautt and Dr. Diplas for taking the time to provide valuable suggestions on this work.

I would like to express my gratitude to National Science Foundation (Grant# BES-9521425-004) that supported this research effort.

A lot of thanks go to all of my colleagues in the ESM Fluid Mechanics Laboratory. Especially, I would like to thank Luis Chalmeta for sharing his technical and laboratory experience. I also express my heartfelt thanks to Jason Burdett for his patient help in performing some of the experiments. I appreciated their friendship and understanding in many difficult times.

Finally, I would like to express my warmest love and gratitude to my family, my father Georgios, my mother Nikoleta, my brother Vassilios and my sister Christina for their moral support and their true love. Also, I would like to thank three friends, Apostolos Orfanidis, Michalis Belessis and Iossif Mugtussidis for their moral support, encouragement and true friendship.

Contents

1 Introduction and Literature Review **1**

1.1 Bottom-mounted Breakwaters 2

1.2 Suspended Breakwaters 4

1.3 Wave Barriers 6

1.4 Wave Reflection, Wave Transmission and Wave Energy Dissipation Coefficients . 7

1.5 Present Aim and Approach 8

2 Experimental Methods and Facilities **10**

2.1 Introduction 10

2.2 ESM Wave Tank 11

2.3 Water Level Measuring Transducers 15

2.3.1 Description and Specifications 15

2.3.2 Calibration 16

2.4 Pressure-head Device 18

2.5 Breakwater Models 19

2.6 The Improvement of the Wave Interception by Flexible Breakwaters 23

2.7 Experimental Methods 26

2.7.1 Methods of Resolving Incident and Reflection Wave Components . . . 26
2.7.2 Flow Visualization and Digital Processing . . . 26
2.8 Representation in Non-dimensional Variables . . . 27

3 Signal Analysis Procedures for Determining Reflection Coefficients 29

3.1 Introduction . . . 29
3.2 Standing and Partial-Standing Waves . . . 32
3.3 Wavelet Analysis . . . 36
3.3.1 Characteristics and Implementation of Morlet Wavelet . . . 39
3.3.2 Numerical Algorithm for the Continuous Morlet Wavelet Transform . . . 46
3.3.3 Numerical Example . . . 49
3.4 Resolution Technique . . . 55
3.5 Typical Results for One Set of Measurements . . . 56
3.5.1 Wavelet Analysis . . . 56
3.5.2 Resolution Technique . . . 60
3.6 Comparison between Wavelet Analysis and Resolution Technique . . . 63

4 Wave Coefficients Over Suspended Flexible Breakwater 66

4.1 Introduction . . . 66
4.2 Experimental Setup and Testing Conditions . . . 67
4.3 Results and Discussion . . . 74
4.4 Conclusions . . . 83

5 Wave Coefficients Over Bottom-Mounted Breakwaters 84

5.1 Introduction 84
5.2 Wave Coefficients Over Rectangular Flexible and Rigid Breakwaters 85
5.2.1 Experimental Setup and Testing Conditions 85
5.2.2 Results and Discussion 93
5.2.3 Conclusions 102
5.3 Wave Coefficients Over Hemi-Cylindrical Flexible and Rigid Breakwaters 103
5.3.1 Experimental Setup and Testing Conditions 103
5.3.2 Results and Discussion 110
5.3.3 Conclusions 115
5.4 Wave Coefficients Over First Hemi-Cylindrical Flexible Composite Breakwater . 116
5.4.1 Experimental Setup and Testing Conditions 116
5.4.2 Results and Discussion 119
5.4.3 Conclusions 124
5.5 Wave Coefficients Over Second Hemi-Cylindrical Flexible Composite Breakwater 125
5.5.1 Experimental Setup and Testing Conditions 125
5.5.2 Results and Discussion 126
5.5.3 Flow Visualization 133
5.5.4 Conclusions 140

6 Conclusions and Recommendations **141**

List of Figures

2.1 Wavemaker setup diagram. 12

2.2 Calibration of ESM plunger type wavemaker. Symbols represent different water depths. 13

2.3 Top-view of wave-absorbing beach. 14

2.4 Water level transducer. 16

2.5 Wave probes setup diagram. 17

2.6 Pressure-head device. 19

2.7 Front-view of hemi-cylindrical, rigid, second and first flexible composite breakwater models, seen from the left. 21

2.8 Side-view of hemi-cylindrical, rigid, second and first flexible composite breakwater models. 21

2.9 Front-view of rectangular rigid and flexible breakwater models. 22

2.10 Wave interception by rigid breakwater. 24

2.11 Wave interception by flexible breakwater. 25

2.12 Dimensional parameters of the problem. 28

3.1 Envelope of standing wave in front of reflective wall at water depth of 25 cm. . . 33

3.2 Envelope of partial-standing wave in front of the beach at water depth of 25 cm. 33

3.3 Envelope of partial-standing wave of 1 Hz in front of the rigid hemi-cylindrical breakwater model at water depth of 25 cm. 34

3.4 Envelope of partial-standing wave of 1.1 Hz in front of the rigid hemi-cylindrical breakwater model at water depth of 25 cm. 34

3.5 Envelope of partial-standing wave of 1.3 Hz in front of the rigid hemi-cylindrical breakwater model at water depth of 25 cm. 35

3.6 Complex-valued Morlet wavelet: (a) real part, (b) imaginary part. 38

3.7 Frequency domain representation of the Morlet mother wavelet presented in Figure 3.6. 38

3.8 Frequency domain representation of three members of Morlet wavelet family, given in (3.13), with $\gamma = 6$. 41

3.9 Frequency domain representation of three members of Morlet wavelet family, given in (3.13), with $\gamma = 20$. 41

3.10 Frequency domain representation of two Morlet mother wavelets, one with frequency parameter f_μ of 0.7 Hz and another of 1.4 Hz at the same $\gamma = 6$. 42

3.11 Real part of the Morlet mother wavelets presented in Figure 3.10. 42

3.12 Frequency domain representation of two Morlet mother wavelets, one with frequency parameter f_μ of 0.7 Hz and another of 1.4 Hz at the same $\gamma = 20$. 43

3.13 Real part of the Morlet mother wavelets presented in Figure 3.12. 43

3.14 Frequency domain representation of Morlet mother wavelet with frequency parameter f_μ of 0.7 Hz when $\gamma = 6$ and $\gamma = 20$. 44

3.15 Real parts of the Morlet mother wavelets presented in Figure 3.14. 44

3.16 Frequency domain representation of Morlet mother wavelet with frequency parameter f_μ of 1.4 Hz when $\gamma = 6$ and $\gamma = 20$. 45

3.17 Real parts of the Morlet mother wavelets presented in Figure 3.16. 45

3.18 Diagram of digital continuous Morlet wavelet transform algorithm. 46

3.19 Cosine function $g(t)$ and magnitude of the mother wavelet coefficient at $f_\mu = 0.7Hz$ with $\gamma = 6$. 48

3.20 Phase of the mother wavelet coefficient at $f_\mu = 0.7Hz$ with $\gamma = 6$. 48

3.21 Signal generated by the numerical example given by (3.14) and magnitude of the wavelet coefficient at $f_\mu = 0.7Hz$ for $\gamma = 6$ and $\gamma = 20$. 50

3.22 Phase of the wavelet coefficient at $f_\mu = 0.7Hz$ for $\gamma = 6$ and $\gamma = 20$. 51

3.23 (a) Signal generated by the numerical example given by (3.14) and magnitude of the wavelet coefficient at $f_\mu = 0.7Hz$ and (b) phase of the wavelet coefficient at $f_\mu = 0.7Hz$. 52

3.24 Vector representation of incident and reflected wave components. 53

3.25 (a) Amplitude and (b) phase of the reflected wave component-Numerical example. 54

3.26 Typical regular wave profiles at two locations: (a) ahead of and (b) behind the suspended breakwater model. 58

3.27 Magnitude (a) and phase (b) of the wavelet coefficient at the frequency of the fundamental wave component in the record shown in Figure 3.26-a. 58

3.28 Real part of the estimated incident wave component (solid line) and real part (dashed line) of the wavelet coefficient at the frequency of the fundamental wave component. 59

3.29 Typical regular wave profiles at three locations: (a) and (b) ahead of and (c) behind of the suspended breakwater model. 61

3.30 Typical plots (a) of composite and (b) of transmitted wave spectra. 61

3.31 Typical plots of resolved incident (solid line) and reflected (dashed line) wave spectra. 62

3.32 Comparison of reflection coefficients between wavelet analysis and resolution method for the suspended breakwater model. Water depth 80 cm. 64

3.33 Comparison of reflection coefficients between wavelet analysis and resolution method for the suspended breakwater model. Water depth 90 cm. 65

3.34 Comparison of reflection coefficients between wavelet analysis and resolution method for the suspended breakwater model. Water depth 100 cm. 65

4.1 Experimental set up of the suspended flexible sack breakwater model. 68

4.2 Dimensions and construction details of deflated flexible sack breakwater model. . 69

4.3 Bottom-front-view of flexible sack breakwater model. 70

4.4 Bottom-view of flexible sack breakwater model. 70

4.5 Bottom-back-view of flexible sack breakwater model. 71

4.6 Connections and deformation of flexible sack's cables. 72

4.7 Oscillation of flexible sack during wave action. 73

4.8 Variation of wave steepness with kh for the flexible sack. Water depth 80 cm. . . 76

4.9 Variations of wave coefficients with kh for the flexible sack. Water depth 80 cm. 76

4.10 Interaction of water waves with the flexible sack grazing the surface without breaking. 77

4.11 Wave breaking over the flexible sack grazing the surface. 77

4.12 Oscillation along the longitudinal direction of the flexible sack grazing the surface. 78

4.13 Variation of wave steepness with kh for the flexible sack. Water depth 90 cm. . . 80

4.14 Variations of wave coefficients with kh for the flexible sack. Water depth 90 cm. For legend see Figure 4.13. 80

4.15 Variation of wave steepness with kh for the flexible sack. Water depth 100 cm. . 82

4.16 Variations of wave coefficients with kh for the flexible sack. Water depth 100 cm. For legend see Figure 4.15. 82

5.1 Experimental setup of the rectangular flexible breakwater model. 87

5.2 Dimensions of the rectangular rigid breakwater model. 88

5.3 Front-view of the rectangular rigid breakwater model. 89

5.4 Side-view of the rectangular rigid breakwater model. 89

5.5 Dimensions of the rectangular flexible breakwater model. 90

5.6 Front-view of the PVC sheet attached to the rubber sheet. 91

5.7 Side-view of the PVC sheet attached to the rubber sheet. 91

5.8 Front-view of the rectangular flexible breakwater model. 92

5.9 Side-view of the rectangular flexible breakwater model. 92

5.10 Typical regular wave profiles at two locations: (a) ahead of and (b) behind the rectangular rigid breakwater model. 95

5.11 (a) Magnitude and (b) phase of the wavelet coefficient at the frequency of the fundamental wave component in the record shown in Fig. 5.10-a. 95

5.12 Real part of the estimated incident wave component (solid line) and real part (dashed line) of the wavelet coefficient at the frequency of the fundamental wave component. 96

5.13 Magnitude of the wavelet coefficient at the frequency of the fundamental wave component in the record shown in Figure 5.10-b. 96

5.14 Variation of wave steepness with kh for the rectangular rigid and flexible models. Water depth 22.5 cm. 98

5.15 Variations of wave coefficients with kh for the rectangular rigid and flexible models. Water depth 22.5 cm. For legend see Figure 5.14. 98

5.16 Variation of wave steepness with kh for the rectangular rigid and flexible models. Water depth 27.5 cm. 101

5.17 Variations of wave coefficients with kh for the rectangular rigid and flexible models. Water depth 27.5 cm. For legend see Figure 5.16. 101

5.18 Experimental setup of the hemi-cylindrical flexible breakwater model. 105

5.19 Dimensions of hemi-cylindrical rigid breakwater model. 106

5.20 Front-view of hemi-cylindrical rigid breakwater model. 107

5.21 Side-view of hemi-cylindrical rigid breakwater model. 107

5.22 Dimensions of hemi-cylindrical flexible breakwater model. 108

5.23 Front-view of hemi-cylindrical flexible breakwater model. 109

5.24 Side-view of hemi-cylindrical flexible breakwater model. 109

5.25 Hemi-cylindrical rigid breakwater model anchored rigidly at the wave tank floor. 110

5.26 Variation of wave steepness with kh for the hemi-cylindrical rigid and flexible models. Water depth 22.5 cm. 113

5.27 Variations of wave coefficients with kh for the hemi-cylindrical rigid and flexible models. Water depth 22.5 cm. For legend see Figure 5.26. 113

5.28 Variation of wave steepness with kh for the hemi-cylindrical rigid and flexible models. Water depth 27.5 cm. 114

5.29 Variations of wave coefficients with kh for the hemi-cylindrical rigid and flexible models. Water depth 27.5 cm. For legend see Figure 5.28. 114

5.30 Dimensions of rubber sheet and composite strips along its longitudinal direction. 117

5.31 Front-view of the first hemi-cylindrical flexible composite breakwater model. . . 118

5.32 Side-view of the first hemi-cylindrical flexible composite breakwater model. . . . 118

5.33 Variation of wave steepness with kh for the hemi-cylindrical rigid and first flexible composite models. Water depth 22.5 cm. 122

5.34 Variations of wave coefficients with kh for the hemi-cylindrical rigid and first flexible composite models. Water depth 22.5 cm. For legend see Figure 5.33. . . 122

5.35 Variation of wave steepness with kh for the hemi-cylindrical rigid and first flexible composite models. Water depth 27.5 cm. 123

5.36 Variations of wave coefficients with kh for the hemi-cylindrical rigid and first flexible composite models. Water depth 27.5 cm. For legend see Figure 5.35. . . 123

5.37 Dimensions of rubber sheet and composite strips along its longitudinal and hoop directions. 126

5.38 Front-view of the second hemi-cylindrical flexible composite breakwater model. . 127

5.39 Side-view of the second hemi-cylindrical flexible composite breakwater model. . 127

5.40 Front-view of the hemi-cylindrical rigid and second flexible composite breakwater models. 128

5.41 Variation of wave steepness with kh for the rigid and second flexible composite models. Water depth 22.5 cm. 131

5.42 Variations of wave coefficients with kh for the rigid and second flexible composite models. Water depth 22.5 cm. For legend see Figure 5.41. 131

5.43 Variation of wave steepness with kh for the rigid and second flexible composite models. Water depth 27.5 cm. 132

5.44 Variations of wave coefficients with kh for the rigid and second flexible composite models. Water depth 27.5 cm. For legend see Figure 5.43. 132

5.45 Light sheet generation setup. 134

5.46 Light sheet in front of the second composite breakwater model. 136

5.47 Light sheet behind the second composite breakwater model. 136

5.48 Light sheet through the water. 137

5.49 Area of interest behind and over the second composite breakwater model. 137

5.50 Particles' streaks behind and over the second flexible composite breakwater model over half period of 1 Hz wave. 138

5.51 Particles' streaks behind and over the second flexible composite breakwater model over the remaining half period of 1 Hz wave. 139

List of Tables

2.1 Specifications of a wave probe. 18

2.2 Breakwater models. 20

4.1 Experimental runs for the suspended flexible sack breakwater model. 74

5.1 Experimental runs for the rigid and flexible rectangular breakwater models. . . . 93

5.2 Experimental runs for the hemi-cylindrical rigid and flexible breakwater models. 110

5.3 Experimental runs for the hemi-cylindrical rigid and first flexible composite breakwater models. 119

5.4 Experimental runs for the hemi-cylindrical rigid and second flexible composite breakwater models. 128

6.1 Average wave coefficients of rigid bottom-mounted models. 142

6.2 Average wave coefficients of flexible bottom-mounted models at lower pressure. . 143

Chapter 1

Introduction and Literature Review

Hurricanes or severe storms moving over the ocean near the shore may greatly change beaches. Strong winds of a storm often create a storm surge, which raises the water level and exposes to wave attack higher parts of the beach not ordinarily vulnerable to waves. Such storms also generate large, steep waves. These waves carry large quantities of sand from the beach to the near shore bottom. Land structures, inadequately protected and located too close to the water, are then subjected to the forces of waves and may be damaged or destroyed. Beaches and dunes can be protected by an offshore breakwater that reduces the wave energy reaching the shore. However, offshore breakwaters are usually more costly than onshore structures and are seldom built solely for shore protection. Offshore breakwaters are constructed mainly for navigation purposes. A breakwater protecting a harbor area provides shelter for ships and boats. Fluid-filled flexible structures can be used efficiently to control storm waves and beach erosion by attenuating the wave energy.

Fluid-filled flexible structures have been proposed as a more effective alternative to rigid structures to control floodwaters acting as dams or to absorb or reflect wave energy acting as breakwaters. For the second case, which is investigated in this work, such structures have several advantages over the conventional rigid breakwaters. One advantage is that they can be utilized as temporary sacrificial breakwaters to reduce the size of storm waves impacting harbors, coastal areas or fixed breakwaters. Another advantage is that flexible breakwaters could provide an inexpensive means of protecting beaches and shorelines exposed to small or moderate

waves and offer fast and relatively easy installation for temporary offshore work. They have a lower construction cost and little weight compared to the conventional large massive structures. Their cost does not increase substantially with depth, while the cost of a fixed structure, such as a rubble-mound breakwater, increases exponentially with depth.

Fluid-filled flexible structures are also attractive because they require little maintenance, they can handle extreme temperatures and they do not corrode. In view of the significant increase of activity in the ocean and coastal environment, inflatable structures could support a number of operations at sea, including oil and gas extraction, fish farming, ocean mining and recreation.

Flexible structures are made of strong reinforced rubber and may be filled with water, air or a combination of air and water. An inflatable structure acting as a breakwater can be deflated in calm weather and inflated only in the event of a severe storm. This can be done in a relatively short time, so that assembly and disassembly may be more efficient than for other types of structures. Thus, marine life or navigation will not be obstructed. Such structures can be compressed into a small volume for ease of transport by ship, helicopter, airplane, or other means when deflated. They can either be suspended or mounted to the ocean floor. For the first case they can be fully-submerged or floating on the water surface. For the second case they are usually fully-submerged.

1.1 Bottom-mounted Breakwaters

Rigid breakwaters extending to the sea-surface have been constructed in the past twenty years to protect pleasure beaches and shorelines against beach erosion, especially in Japan. Recently, the human desire to protect the beauty of shore landscape and the interest for development of marine recreational areas convinced people to think and apply different and more environmentally-friendly solutions. One solution, which can meet these needs, is submerged dikes instead of detached breakwaters. Submerged dikes, however, require vast cross-sectional areas and therefore demand high construction cost. Submerged, fluid-filled flexible structures offer an alternative solution. Flexible, bottom-mounted structures reduce the construction cost much more than the conventional submerged dikes. Moreover, because of their deep submer-

gence, ships may pass over them and also the sea-area is available for recreational purposes. Such structures also could be rapidly deployed to protect a harbor or moored vessels from the destructive effects of water waves.

Extensive experimental and theoretical investigations have been conducted to examine the performance of different geometries of sea-bed mounted rigid structures. Rey et al. [27] conducted wave tank experiments over a rectangular submerged bar. Beji and Battjes [2] also conducted laboratory experiments to study the generation of higher harmonics by a submerged trapezoidal bar. Mallayachari and Sundar [22] investigated numerically the wave reflection characteristics over submerged rectangular steps of finite length. They compared reflection characteristics of rectangular structures with half cylinder and trapezoidal obstacles. Ertekin and Becker (1996) [10] applied a finite difference method to examine diffraction of waves by a submerged bottom-mounted trapezoidal obstacle.

As for fluid-filled structures, Frederiksen [11] discussed the effectiveness of a pneumatic mattress as a submerged breakwater. He proposed a device that incorporates an air-filled duct inside a bag made of rubber positioned beneath the surface. Ijima et al. [13], [14] proposed and studied numerically and experimentally a "sea-balloon" system as a submerged bottom-seated flexible breakwater. It consists of a number of flexible bags filled with air and connected pneumatically to each other by a pipe. As they deflect due to incident waves, air moves from one bag to another. The latter deformation of the "sea-balloon" system produces a radiation wave, which is composed of two component waves. The one proceeding seaward constitutes the main part of the reflected wave at the breakwater and the other moving leeward ends as the transmitted wave. The radiation wave has a dominant effect on the interception by the "sea-balloon" system. They estimated basically transmission coefficients and a few reflection coefficients considering the effect of different parameters such as the number and the size of the balloons and the distance between the fore and rear balloon.

Experiments on a "flexible-mound" breakwater were conducted by Ohyama et al. [26] and Tanaka et al. [30]. This is a horizontal, hemi-cylindrical thin flexible membrane bag filled with water and attached to the sea-bed. The influences of several parameters, such as the internal added pressure, the elasticity of the membrane and the submergence ratio upon the wave reflection and transmission were discussed. The experimental results indicated that the

response motion of the "flexible-mound" to the incident waves generates radiation waves, which reduce the transmitted wave heights in a wide range of wave frequency. These authors also presented some numerical results obtained with a linear two-dimensional boundary element code. Two units of the "flexible-mound" 9 m wide, 40 m long and 3 m high have been installed at an entrance of a small harbor to protect it. During a storm surge, the mounds are inflated by water and serve as emergency breakwaters (Tanaka et al. [31]).

Liapis et al. [21] analyzed a structure similar to the "flexible-mound". The study was two-dimensional and considered waves over a submerged, bottom-mounted, water-filled, hemi-cylindrical membrane. The transmission coefficient was computed for this structure and also for a rigid structure of the same shape. The results showed the flexible breakwater to be more effective. Dewi [9] extended the previous study to three-dimensional analysis. The same type of structure was modeled as a shell, rather than a membrane, so that its flexural rigidity was included. In the latter study, both normal as well as oblique waves were considered. The structure was found to be effective in reducing the incident wave intensity over a wide range of frequencies.

1.2 Suspended Breakwaters

The suspended flexible fluid-filled structures have an advantage over those attached to the sea bottom, since they can be used for larger depths and therefore are not limited to small distances from the beach. These type of breakwaters often provide a cost-effective and efficient solution of protection from wave attack in semi-protected regions. They may be preferred in deeper waters, in areas where poor foundation conditions or environmental constraints exist or where protection is required only on a temporary basis, such as pollution control, salvage operations and construction and maintenance of offshore platforms. Such structures could also protect floating airports or portable ports. They also have advantages over suspended rigid structures. For instance, they are portable and easy to install. They can be inflated only in the event of a severe storm and be deflated otherwise, so as not to disturb or obstruct marine life and navigation. Because the attachment to the ocean floor can be done only with cables, the layer of bed-load, where plants and live organisms grow can be preserved.

Different types of suspended breakwater models have been tested experimentally and investigated theoretically. Wave attenuation by moored rigid cylinders acting as breakwaters was investigated numerically by Mays [24] for both normal and oblique monochromatic waves. Free surface elevations were obtained for a single cylinder and for two cylinders in series. Two-dimensional and three-dimensional experimental studies of the interaction of fluid-filled floating bags with water waves were carried out by Wiegel et al. [35] and Frederiksen [11]. Parametric studies were conducted, assessing the importance of the bag length, bag thickness and elasticity of the material on wave attenuation. When the wave attenuation was high, the transmitted wave was observed to have multiple crests, indicating the importance of nonlinearity. Also, the three-dimensional aspects of the diffraction of waves were found to be very important. Wiegel et al. [35] reported on a field study of the effectiveness of water-filled mattresses hovering in the random wave environment of the ocean. The advantage of such a device is that it may be transported to the site as a collapsed form in a roll, then unrolled, lashed to other sections, moored and pumped full of sea water. The structure performed very well in the ocean environment and in some instances even better than in the laboratory experiments, owing to the relative instability of the wind waves compared with the swell type waves of the laboratory. The mechanisms by which the hovering breakwater attenuated the waves were not determined. Frederiksen's [11] laboratory experiments indicated that a bag filled with a fluid floating on the water surface offers a potential means of attenuating waves. Although he mentioned the mechanisms of energy dissipation, he estimated only attenuation coefficients. Another idea, which uses flexible structures, was a wave blanket. This is a membrane made of permeable material and designed to float just below the free surface. The wave blanket absorbs the energy of the waves by deforming. Ripken [28] experimentally studied the influence of the length, width, thickness and material of the blanket on the wave attenuation.

Recently, Broderick [3], Broderick and Leonard [4], [5], Broderick and Jenkins [6], and Jenkins and Leonard [16], [17] conducted large-scale two-dimensional experiments on the interaction of water waves and a water-filled membrane. The membrane formed a 4 m long circular cylinder and was placed beneath the free surface. The membrane material was plasticized PVC. The elevation of the free surface was recorded fore, aft, and on top of the cylinder. String pots were also used to measure the displacements at three locations on the cylinder. The results show

that there is a range of wave periods where the fluid-filled membrane is an effective breakwater. Their work also contains two-dimensional numerical calculations using an inviscid boundary element formulation for the fluid flow and a finite element membrane model for the structure.

A combination of submerged and floating breakwaters can be fine-tuned for maximum benefit at a location. The submerged flexible structures can be placed seaward of the floating breakwater, improving the efficiency of both structures. Larger waves would break on the submerged ones, changing the sea-state to one that the floating structure is more effective at reducing.

1.3 Wave Barriers

Another type of suspended breakwaters is a wave barrier. These are rigid cylinders or buoys that support vertical membranes. They have been considered in a number of papers. Milgram [25] investigated the problems of determining the motion as well as the structural and hydrodynamic forces on a flexible, floating barrier. Such barriers are frequently used as containment devices for floating pollutants such as oil. A wave barrier was also investigated analytically by Thompson et al. [33]. It consists of a thin flexible membrane suspended from a moored cylindrical buoy pipe on the free surface and fixed to a hinge at the seafloor. The theoretical model is verified experimentally. The flexible membrane was constructed of a vinyl-coated material used in the construction of inflatable rafts. The cylindrical buoy was a 0.61 m (2 ft) diameter PVC pipe.

Williams [36] developed a numerical model to investigate the behavior of a pair of flexible, floating breakwaters consisting of beam-like structures anchored to the sea-bed. Each structure is kept under tension by a small buoyancy chamber at the tip. Additional stiffness is provided by mooring lines attached to the chamber. Numerical results are presented to illustrate the effects of various wave and structural parameters on the efficiency of the system as a barrier to wave action. It was found that by adjusting the spacing between the breakwaters, acceptable wave reflection characteristics may be obtained even with relatively flexible structures. Abul-Azm [1] presented an analytical method for the wave reflection and dynamic displacement of a submerged flexible breakwater. The breakwater is assumed to be thin, flexible, moored to the bed through tethers and kept in tension by means of a floating buoy at its tip. Numerical

results based on the eigenfunction expansion technique are presented, mainly to show the effect of the breakwater rigidity and the method of fixation on the wave reflection and the structural displacement over a wide range of wave frequencies.

Recently, Kim and Kee [19] presented analytical and numerical solutions for the interaction of water waves with a tensioned, unstretchable, vertical flexible membrane extended to the sea-bed. It is found that almost complete reflection of incident waves by a flexible-membrane wave barrier is possible despite appreciable fluctuating motions of the membrane in a vertically sinusoidal manner. Based on this analysis, Kim and Kee [20] investigated theoretically and experimentally the interaction of water waves with a tensioned, inextensible membrane hinged at the sea floor and attached to a solid cylindrical buoy at its top. From the numerical results, it can be concluded that the buoy/membrane wave barrier can function as a very effective breakwater if it is properly designed. The numerical results were further verified by checking several limiting cases and through comparison with the experiments conducted in a 2D wave tank. Both submerged and floating (or surface-piercing) buoy-membrane wave barriers were considered. The flexible membrane was made of a thin stretch-resistible plastic material resembling a plastic tarpaulin. The cylindrical buoy was a 21.3 cm diameter PVC pipe. The efficiency of such breakwaters depends critically on the buoy-radius to water-depth ratio and on the mooring-line stiffness.

1.4 Wave Reflection, Wave Transmission and Wave Energy Dissipation Coefficients

Water waves may be either partially or totally reflected for both natural and man-made breakwaters. Wave reflection may often be as important a consideration as refraction and diffraction in the design of coastal structures, particularly for structures associated with development of harbors. Reflection of waves implies a reflection of wave energy as opposed to energy dissipation. Consequently, multiple reflections and absence of sufficient energy dissipation within a harbor complex can result in a buildup of energy which appears as wave agitation and surging in the harbor. These surface fluctuations may cause excessive motion of moored ships and other

floating facilities and result in the development of great strains on mooring lines. Therefore breakwaters inside of harbors should dissipate rather than reflect incident wave energy whenever possible. A measure of how much a breakwater reflects waves is given by the ratio of the reflected wave height, H_r, to the incident wave height, H_i, which is termed the reflection coefficient, C_r, hence $C_r = H_r/H_i$. The magnitude of C_r varies from 1.0 for total reflection to 0 for no reflection. However, a small value of C_r does not necessarily imply that wave energy is dissipated by a structure, since it may be tranmitted over such structures. A transmission coefficient may be defined as the ratio of transmitted wave height, H_t, to the incident wave height, H_i, hence $C_t = H_t/H_i$. In general, both the reflection and transmission coefficients will depend upon the geometry and composition of a structure and the incident wave characteristics such as wave steepness and relative depth at the structure site. Moreover, when waves interact with breakwaters, a portion of the wave energy is dissipated, resulting in further reduction of wave transmission. A measure of how much a breakwater dissipates waves is given by the ratio of the loss in wave height, H_L, to the incident wave height, H_i, which is termed the energy loss coefficient, C_L, hence $C_L = H_L/H_i$. Based on wave energy conservation, the energy loss coefficient, C_L, can be calculated from the following relation (Thornton and Calhoun [34]):

$$C_r^2 + C_t^2 + C_L^2 = 1 \tag{1.1}$$

1.5 Present Aim and Approach

In this study we investigate extensively both wave reflection and transmission processes of regular non-breaking water waves over several types of rigid and flexible breakwater models. Different geometries of rigid and flexible structures were constructed and examined. A detailed presentation of these structures is given in Chapter 2. Most of the flexible structures have been treated as membranes by researchers. They used "membrane theory", which neglects flexural rigidity to analyze their performance. However, the structures envisaged here are made of strong reinforced rubber and must be modeled as "shells". The influence of various properties of the models, such as the width and the internal pressure, on the effectiveness in reflecting or absorbing the incident wave energy is determined. Various factors which affect the performance of the breakwater, including the water depth, the wave length and the wave amplitude, are

measured and documented. Suspended and bottom-mounted models are considered.

A conventional signal analysis procedure for determining reflection coefficients is compared to a new method based on wavelet theory. The first method is based on linear wave theory and uses two fixed wave probes to obtain a reflection coefficient. The accuracy of this method depends on the spacing between the probes and the amplitude of the incident waves, which should be small. The method based on wavelet theory shows how the amplitude and phase of the reflected wave component vary with the time. Wavelet analysis is not constrained to linear wave theory or Stokes' 2nd order wave theory, which are valid only for small-amplitude waves. Wavelet analysis can provide accurate estimates of reflection coefficients also for high-amplitude incident waves, which theoretically are covered by higher-order wave theories. Furthermore, this method does not depend on any probe spacing since it uses only one fixed probe ahead of a breakwater model to obtain a reflection coefficient. It is presented analytically in Chapter 3. The reflection, transmission and energy loss coefficients of regular non-breaking incident waves over a suspended flexible sack are presented in Chapter 4. In Chapter 5 the wave coefficients of regular non-breaking incident waves over bottom-mounted models of different geometries are presented. A flow visualization technique is also used in this research effort to study the structure of the flow over and near a hemi-cylindrical bottom-mounted breakwater model. Finally, an overall comparison among the models and a recommended research as a natural continuation of the present work, are discussed in Chapter 6.

Chapter 2

Experimental Methods and Facilities

2.1 Introduction

In this chapter we describe the facilities and breakwater models used in the experiments. The experimental model studies were carried out in the Engineering Science and Mechanics (ESM) Department wave tank at Virginia Tech. The wave tank consists of a basin, a towing carriage, a wavemaker and a wave absorbing beach. Description and further information for each of these components are given below. Three wave probes were used to measure the water elevation in the wave tank. In order to supply the flexible breakwater models with water and recover any water losses during the experiments, a pressure-head device was constructed and installed behind the breakwaters. Rectangular and hemi-cylindrical rigid and flexible models were tested. In this chapter, we also explain the mechanisms of the wave interception over rigid and flexible breakwaters. Finally, we present the experimental methods for determining reflection and transmission coefficients. A new method based on the principles of wavelet analysis is used to resolve the composite wave in front of the breakwaters into incident and reflected wave components. A flow visualization setup is also used in order to capture the flow over and near a hemi-cylindrical flexible breakwater model.

2.2 ESM Wave Tank

The basin of the wave tank is made of reinforced concrete, painted with chemical and moisture resistant enamel. The width of the basin is 1.83 m (6 ft). The height of the tank is 1.56 m (5 ft 3/2 in) with maximum water depth of 1.22 m (4 ft). The overall length of the basin is 27.93 m (91.63 ft), and 25.23 m (82.77 ft) is the distance from the wavemaker foot to the end of the tank. The first 1.24 m (4 ft) are used for braking the carriage. There is one glass walled observation pit along the side of the tank, located approximately in the middle of the test region.

The towing carriage and rails were designed by the firm of Kempf and Remmers of Hamburg, Germany and were shipped in sub-assemblies to Virginia Tech. The allowable tolerance on rail height was 0.1 mm. Wedges were used to give final straight alignment of each rail. The allowable tolerance on alignment was 0.2 mm. Final alignment was done optically. After final adjustments in height were made, the space between the bearing plates and the bottom of the rail was filled with concrete. A 400 V DC motor drives the carriage through a gear reduction box. The DC power is supplied from a 220 V AC motor-generator set. With the gear box lever set in position I, the maximum speed the carriage can reach is 0.22 m/sec at 3000 RPM. With the lever set in position II, a maximum speed of 3 m/sec at 3000 RPM can be achieved. For more precise control in the low speed range, the DC motor can be switched to a maximum 1500 RPM at full voltage. The carriage braking is done automatically using trips installed at both ends. An emergency brake button is also located on the console. The brake is applied if the power to the carriage is interrupted. Braking deceleration is 0.7 m/sec.

A plunger type wavemaker made of a flat stainless steel plate is installed at one end of the wave tank. A set of wave absorbers is placed behind the wavemaker to reduce end reflections. The wavemaker is driven by an electric-hydraulic motor. The wavemaker is capable of producing surface waves with frequencies ranging from 0.2 to 2 Hz. A 275 Wavetek model digital function generator is used to run the wavemaker through a BNC connector, as shown in Figure 2.1. In order to find the upper limits, where the wavemaker generates regular, well-shaped and non-breaking incident waves before their interaction with the breakwater models, we tested progressive waves in different amplitudes at the same wavemaker driving frequency

for different water depths. Based on our observations, the wavemaker can generate well-shaped waves between 0.6 and 1.4 Hz for water depths between 22.5 and 30 cm. Outside of this range the wavemaker needs some time period to establish a non-transient wave sequence train. The results of this calibration process are presented in Figure 2.2. This shows the non-breaking operation upper limits at each water depth. Below each measured parabolic curve the wavemaker generates regular, non-breaking incident waves. As also shown in Figure 2.2, the wavemaker needs a minimum voltage amplitude around a frequency of 0.9 Hz at each water depth. The voltage amplitude applied to the wavemaker for all breakwater models was chosen to be below these measured curves.

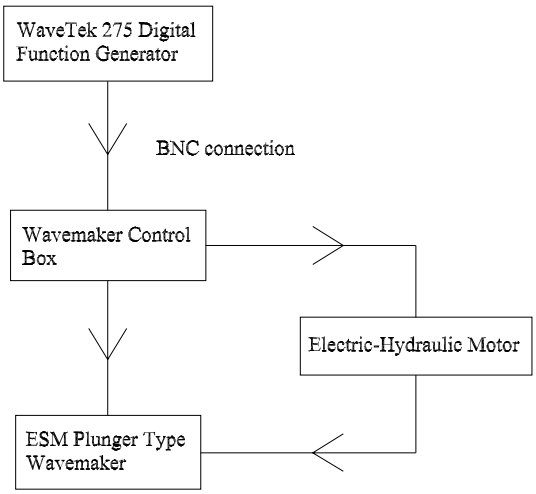

Figure 2.1: Wavemaker setup diagram.

The wave tank is also equipped with a permeable wave-absorbing beach at the downstream end in order to reduce end reflections. It consists of two heavy rectangular stainless-steel flat plates 1.83m x 1.37m (6ft x 4.5ft) having 2.54 cm (1 in) diameter holes spaced by 2.54 cm (1 in) in each direction to destruct and dissipate the incoming water waves. As shown in Figure 2.3,

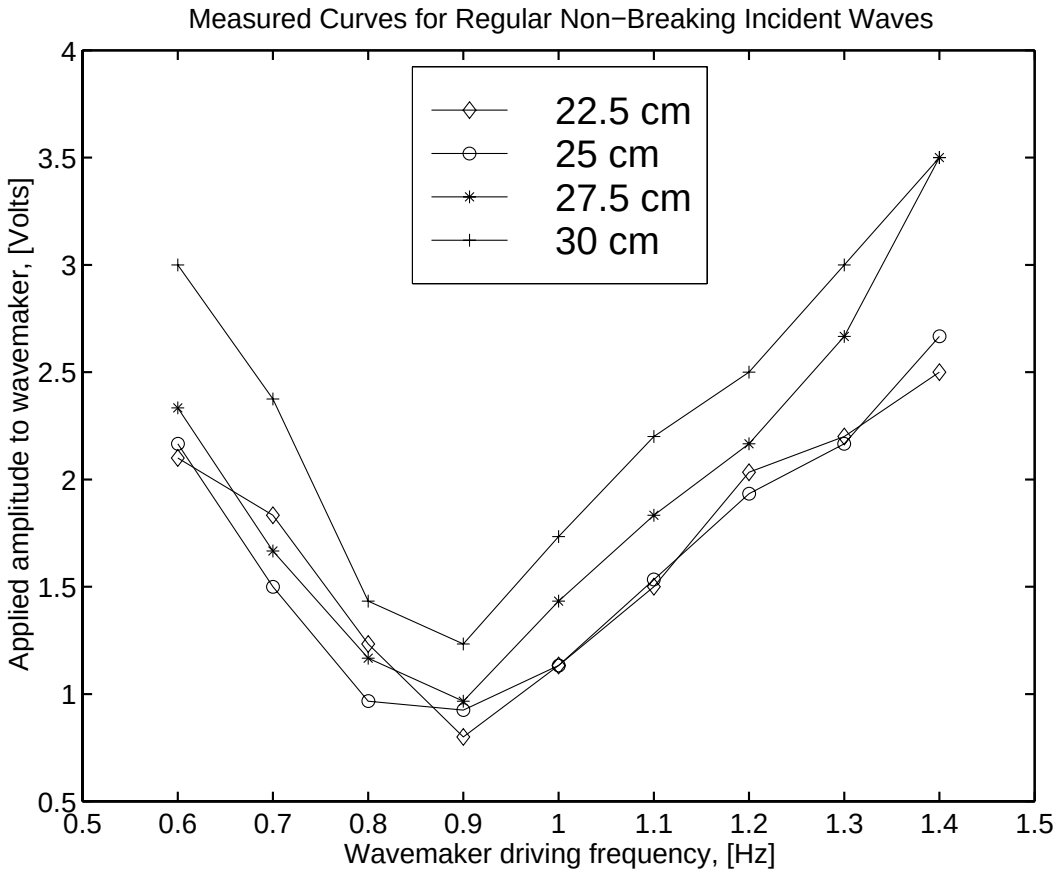

Figure 2.2: Calibration of ESM plunger type wavemaker. Symbols represent different water depths.

one plate is connected with hinges at the top of the other plate. The bottom plate is rigidly mounted on the wave tank's end. The angle, θ, between the two plates is adjustable. The slope angle, ϕ, between the top plate and the wave tank basin was adjusted to be 28^o for all experimental runs involving the anchored breakwater models. As for the suspended breakwater model, the slope angle was adjusted to be 51^o.

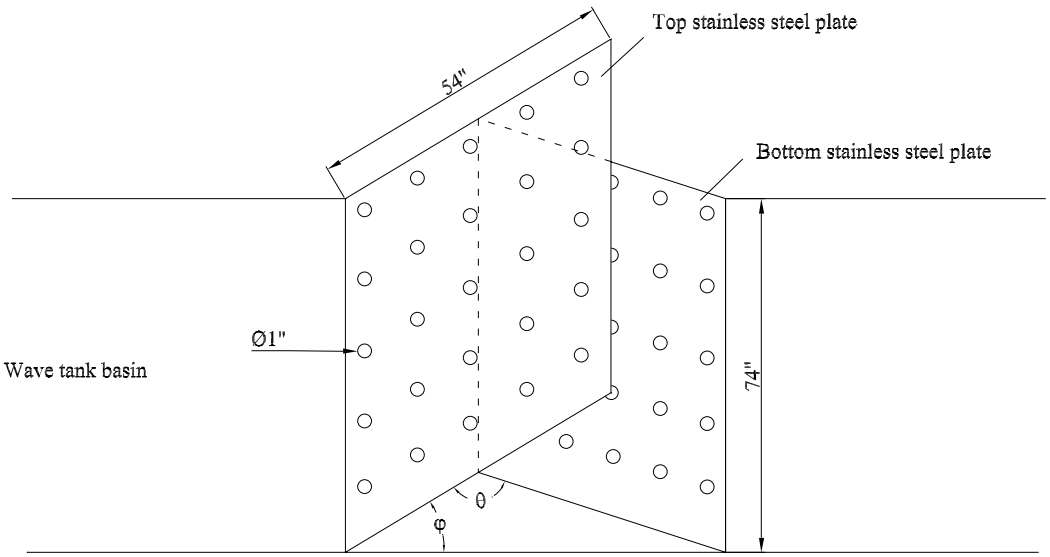

Figure 2.3: Top-view of wave-absorbing beach.

2.3 Water Level Measuring Transducers

2.3.1 Description and Specifications

Three WL/WP 03 wave probes with capacitance transducers, designed by Davis Engineering Company, were used to measure the water surface elevation. The water level transducers translate water depth to a high level analog DC output voltage. They are well suited to absolute water level measurements such as reservoir applications and/or relative water level measurements such as wave applications. The transducer, shown in Figure 2.4, consists of a sensor element and signal conditioning electronics. The sensor element is a special capacitor whose capacitance increases linearly with depth of submersion. The circuitry includes a capacitance to voltage converter, followed by several filters. The final stage amplifies the gain on the output signal. The filters may be configured so that the system ignores slow level changes or fast level changes or both when only a restricted range of wave frequencies is of interest.

The wave probe is designed to be mounted using four mounting clips in an accompanying instrument wood carriage by means of the support rod. This will orient the wave probe vertically to the incoming water waves. Other angles may be used as long as both the stainless steel probe's support rod and capacitance wire portions are partially submerged during the measurement. They do not have to be equally immersed. The capacitance wire is 22 gauge copper with a lacquer coating. The capacitance wire element is connected to the binding posts and strung around a grooved nylon bushing at the bottom of the ground rod. The wire should have no kinks or twists and must not make electrical contact to the water. This implies that the binding posts must remain above the water for valid measurements. The tension in the wire was kept at approximately 1 kg force by adjusting the wire length at the binding posts.

The wave probes are connected to the same power supply and their outputs are driven through BNC connectors to a data acquisition board in a laboratory computer. This is an AT-MIO-16E-2 National Instruments' data acquisition board with 12-bit A/D sampling resolution and sampling rate up to 500 kHz. Both the data acquisition board and the computer are configured by a LabView commercial program. The total setup is shown in diagram 2.5. The specifications of the wave probe are gathered and listed in Table 2.1.

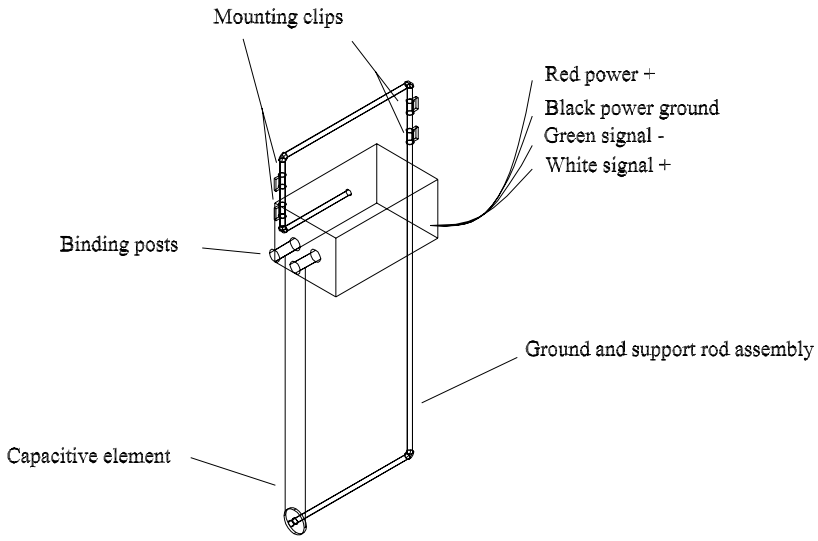

Figure 2.4: Water level transducer.

2.3.2 Calibration

Calibration of each of the wave probes was carried out before each set of experiments. Each of the probes was mounted on a traversing scale and partially submerged in a bucket full of water. The traversing scale is a Velmex MA2500 series 36 in low-profile scale. It is linear and it has 20 threads per inch. The scale, which is driven by a stepper motor on its top end, moves the probe into the bucket. The motor is a Vexta PK245-02AA two-phase stepper motor (6 Volts, 1.2 amps per phase) with 1.8^o per step. With the above scale, that translates to 1/4000 inches linear traverse per motor step. The motor is controlled by a stepper motor controller. This is an Aeroprobe M-2CON stepper motor controller. It translates weak signals from the computer into high-current signals that make the motor turn. The controller is connected to the computer through a data acquisition board. We use a Computer Boards DAS-08 data acquisition board with 12-bit A/D sampling resolution and sampling rate up to 20 kHz. A Turbo-Pascal program

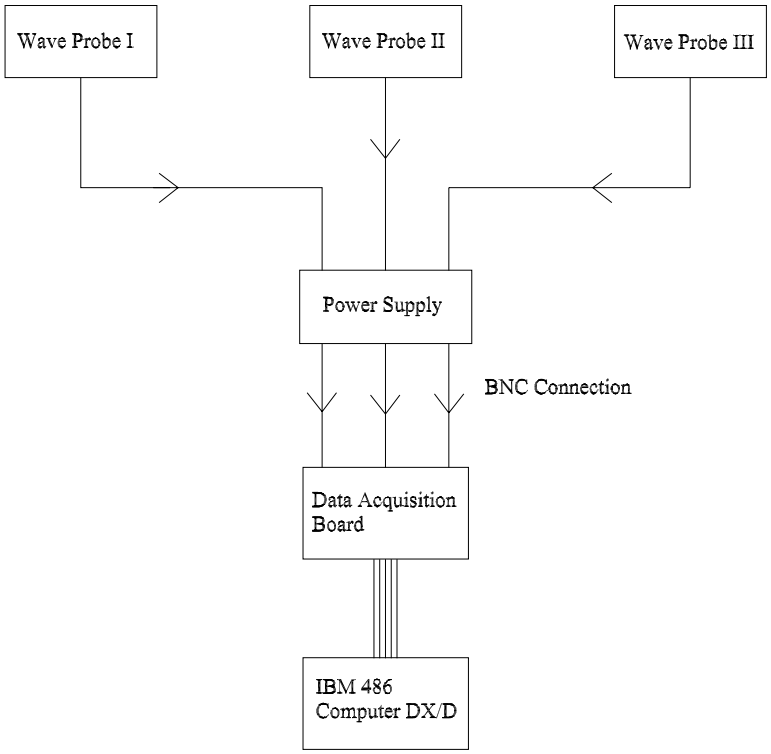

Figure 2.5: Wave probes setup diagram.

was written to move the motor and acquire the data at each water level point. The software sends out digital pulses with the DAS-08 to control the motor and to use the A/D converter on the DAS-08 to sample the voltage from the wave probe at each calibration point. At each point, data are obtained for a 4 second interval at a sampling rate of 250 Hz (1000 samples total) and are averaged. According to the calibration for all three wave probes, it is found that in a region of 5 cm close to the grooved nylon bushing at the bottom of the probe ground rod, the relation between the output voltage and the water height is not exactly linear. Since the water depth used for the anchored breakwater models was below 30 cm, we tried to avoid that region of the wave probes by setting them as deeply submerged as we could.

Table 2.1: Specifications of a wave probe.

Accuracy	± 1% of Full Scale
Resolution	± 0.2% of Full Scale
Linearity	± 0.5% of Full Scale
Ripple and Noise	± 5 mV p-p
Output	± 0 - 5.0 Volts DC
Measurement Range	0 - 1 m
Low Pass Filter Cut-off Frequency	20 Hz
Power Supply	14V DC to 24V DC 25mA

2.4 Pressure-head Device

A pressure-head device was constructed and used to keep the internal pressure constant and recover any water losses in the flexible breakwater models during the experimental runs. As shown in Figure 2.6, this device consists of a cylindrical PVC pipe and a water supply pump. This system was placed 7.33 m behind the flexible models and 4.22 m behind the downstream wave probe in order not to influence the measured transmitted waves. The cylindrical pipe is closed at its bottom end and open at its top. It is attached with brackets to the tank wall. The pump is attached to the bottom of the wave tank and supplies the pipe continuously with water through a plastic hose from its top when an experiment runs. The pipe is also equipped with two plastic tubes closed at the bottom. The lowest tube is connected to flexible breakwater models through a plastic hose and supplies them with water. The plastic hose is attached to the bottom of the wave tank close to the wall with brackets in order not to float. The other tube, positioned on the other side of the pipe, drains the water out of the pipe in the wave tank, keeping the height of the water inside the flexible model at the desired level. A piezometric tube with a scale on it is attached to the flexible models in order to read the water head. It is possible to adjust the vertical position of the pipe and increase or decrease the internal pressure in the flexible model. In this way, we fill a flexible model with water and set its internal pressure at a desired value before an experimental run starts. During the run, this device recovers any

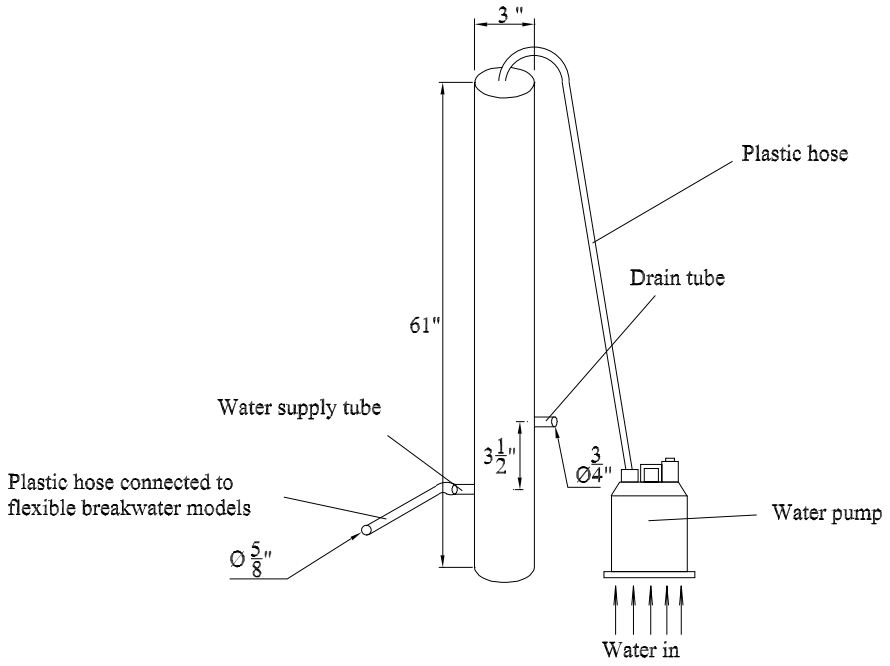

Figure 2.6: Pressure-head device.

water losses and automatically sustains the desired internal pressure.

2.5 Breakwater Models

We performed experimental tests to examine the effectiveness of rectangular and hemi-cylindrical, rigid and flexible models, as breakwaters. All the rigid models are made of PVC mounted on aluminum plates. The rectangular flexible model is made of rubber and is also reinforced inside at the top with a PVC sheet. The hemi-cylindrical flexible model is also made of rubber. Both of them are fastened on aluminum plates. With the use of modern composite materials, the flexible structures could withstand significant wave forces without serious damage. Thus, we use some composite material strips attached to the rubber along the longitudinal direction for one hemi-cylindrical model (first flexible-composite model) and along the longitudinal and hoop

direction for another hemi-cylindrical model (second flexible-composite model). The features of all these models are summarized in Table 2.2. Photos of hemi-cylindrical, rigid and flexible-composite breakwater models are presented in Figures 2.7 and 2.8. A photo of the rectangular, rigid and flexible breakwater models is presented in Figure 2.9. The latter breakwater models were all inflated with water and mounted on the bottom of the wave tank at Virginia Tech. A flexible-sack model suspended in the wave tank was also tested. It is made of rubber and inflated basically with water. It is also equipped with a narrow flotation air-tube made of rubber to provide the appropriate buoyancy to the flexible sack.

Table 2.2: Breakwater models.

Bottom-mounted Breakwater Models			
Type	**Geometry**	**Filled**	**Dimensions**
Rigid	Rectangular		6ft x 1ft x 6.75in
Flexible	Rectangular	Water	6ft x 1ft x 6.75in (inflated)
Rigid	Hemi-Cylinder		6ft x 6in (diameter)
Flexible	Hemi-Cylinder	Water	6ft x 6in (diameter) (inflated)
First Flexible Composite	Hemi-Cylinder	Water	6ft x 6in (diameter) (inflated)
Second Flexible Composite	Hemi-Cylinder	Water	6ft x 6in (diameter) (inflated)
Suspended Breakwater Model			
Flexible-sack	Raindrop	Water & Air	6ft x 16.5in (deflated)

Figure 2.7: Front-view of hemi-cylindrical, rigid, second and first flexible composite breakwater models, seen from the left.

Figure 2.8: Side-view of hemi-cylindrical, rigid, second and first flexible composite breakwater models.

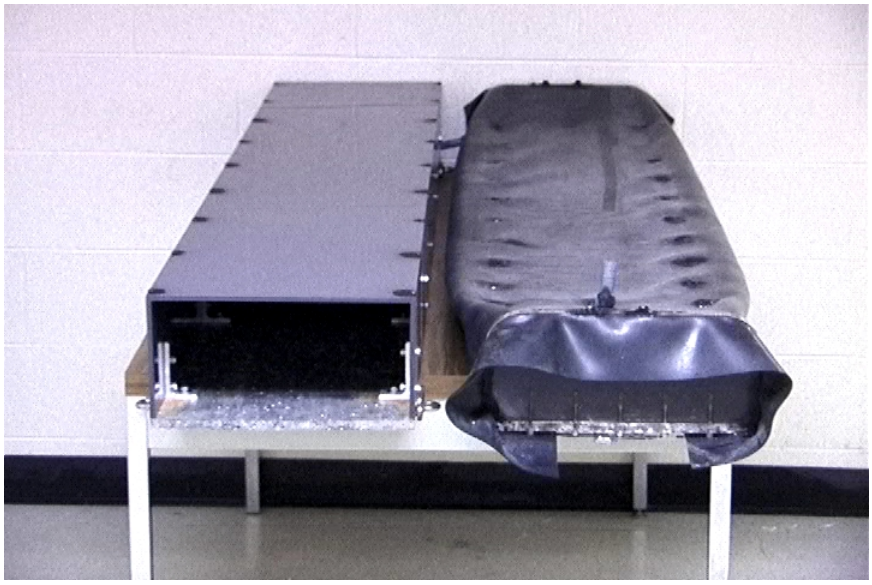

Figure 2.9: Front-view of rectangular rigid and flexible breakwater models.

2.6 The Improvement of the Wave Interception by Flexible Breakwaters

When a rigid breakwater interacts with surface waves, part of the incident wave energy travels over the rigid structure, forming the transmitted wave, and the remaining part, if there is no wave breaking, is reflected back, as shown in Figure 2.10. The incident and reflected wave components can be considered as two progressive waves moving in opposite directions. The superposition of the incident and reflected wave trains in front of the breakwater forms a partial standing-wave system (composite wave). While the wave periods of the incident and reflected waves remain the same, a phase lag, induced by the reflection process, is added to this system.

When a flexible fluid-filled breakwater is placed in a water environment and subjected to waves, it undergoes motions and deformations. There are different mechanisms present in the interaction of this compliant structure with the fluid motion. Particularly, when an incident wave interacts with a flexible breakwater without wave breaking, initially a part of it is reflected and another is transmitted without energy losses, as shown in Figure 2.11. However, the flexible structure is also able to oscillate and causes water surface fluctuation. The periodic repetition of such a fluctuation of the free surface produces the radiation wave, as also shown in Figure 2.11. The radiation wave is composed of two component waves with the same amplitude, one proceeding ahead of the structure and the other behind the structure. The component wave to the left constitutes part of the reflected wave by the motion of the breakwater and the one to the right either reduces or amplifies the transmitted wave depending on their phase relation. If the initial transmitted wave and the radiation wave, generated by the flexible breakwater's motion, have the same height but in inverse phase, then the transmission coefficient is almost zero.

The wave reflection and transmission in the presence of a rigid or a flexible fluid-filled breakwater structure would occur with the loss of some portion of the incident wave energy by the following processes: losses due to wave breaking over the structure, losses due to turbulence induced by flow separation, developed over and near the structure and internal losses due to turbulence

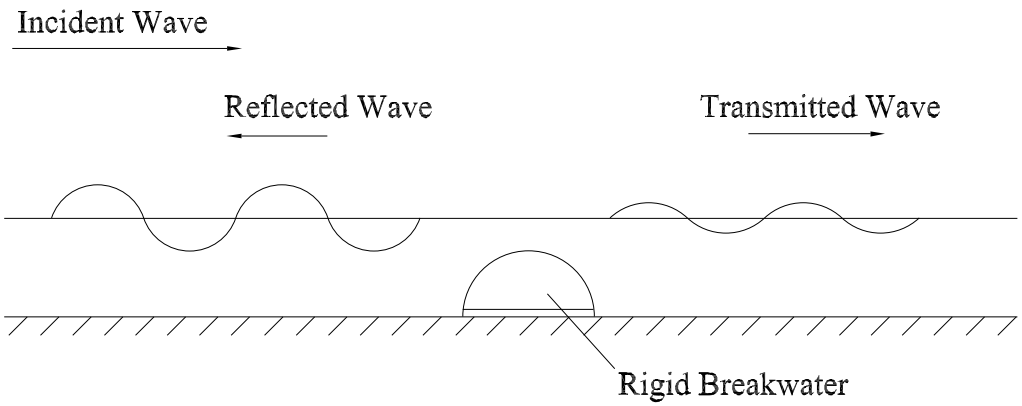

Figure 2.10: Wave interception by rigid breakwater.

of the fluid contained inside the structure as well as non-elastic deformations of the structure itself. These losses mentioned above are considered in the energy loss coefficient, C_L, defined in section 2.8.

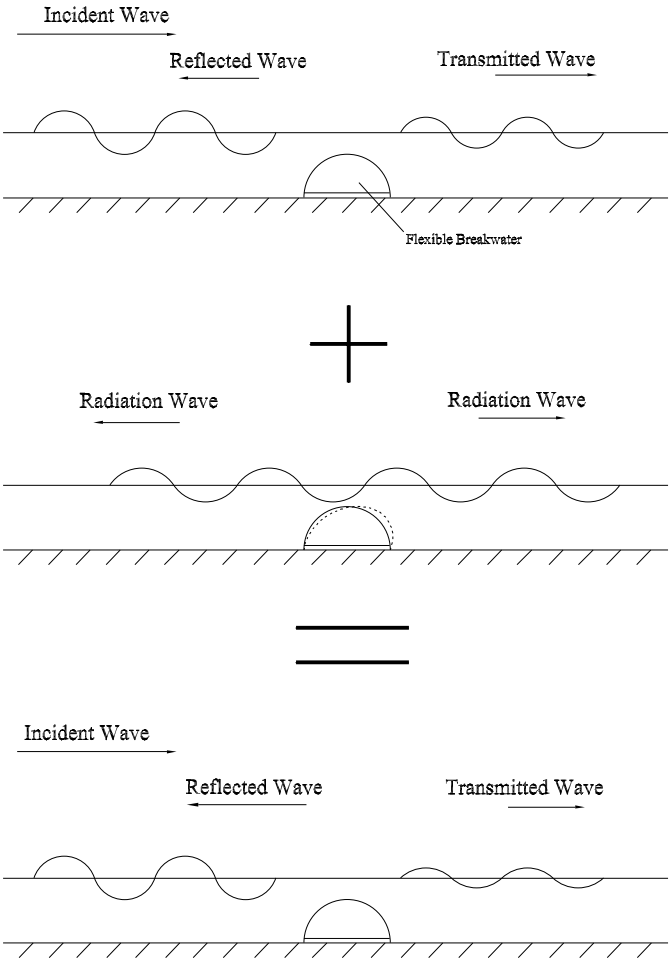

Figure 2.11: Wave interception by flexible breakwater.

2.7 Experimental Methods

2.7.1 Methods of Resolving Incident and Reflection Wave Components

Two methods are employed to decompose the composite wave into reflected and incident wave components. The first method, namely "resolution technique", involves two fixed wave probes ahead of the breakwater model. This has been described by Thornton and Calhoun [34] and is based on linear wave theory. According to this technique, two measured wave heights and one phase angle are enough to decompose the composite wave and give the incident wave height and the height and phase of the reflected wave component. The former method is described briefly in section 3.4. A new method developed on the basis of wavelet theory is presented in detail in Chapter 3. It uses the measurements from one fixed wave probe to yield the temporal evolution of both the amplitude and phase of the reflected wave component. A comparison between the two methods will been given, calculating reflection coefficients for some of the records of the suspended flexible-sack breakwater model, in section 3.6.

2.7.2 Flow Visualization and Digital Processing

In the experimental field, flow visualization is clearly the first step in identifying the key feature of the flow. However, such information is often lost, because it is not documented in quantitative form. Good documentation of flow visualization is necessary, preferably in the form of digital data. Flow visualization is used in this research effort to study the structure of the flow over the second flexible composite breakwater model. Particle trajectories were obtained in a progressive water wave of specific frequency by seeding particles in the area behind the model. A SONY Digital Video Camera Recorder was used to convert the flow visualizations to numerical data. The flow visualization technique is presented in section 5.5.3.

2.8 Representation in Non-dimensional Variables

The relationship between the characteristics of wave reflection, wave transmission and energy dissipation for the rigid and flexible breakwater models can best be presented in terms of dimensionless parameters. The dimensional parameters characterizing the problem and presented in Figure 2.12 are the incident H_i, reflected H_r and transmitted H_t wave heights, the loss in wave height H_L due to the processes of energy loss, the depth of submergence z, the internal pressure-head in the flexible model y, the incident wave length L, the water depth h and the model width b. These variables can be grouped in dimensionless form $(\frac{H_r}{H_i}, \frac{H_t}{H_i}, \frac{H_L}{H_i}, \frac{H_i}{L}, kh, \frac{z}{h}, \frac{y}{h}, \frac{b}{L})$ where $k = \frac{2\pi}{L}$ is the wave number. Note that $\frac{H_i}{L}$ is the wave steepness, $\frac{H_r}{H_i} = C_r$ is the reflection coefficient, $\frac{H_t}{H_i} = C_t$ is the transmission coefficient and $\frac{H_L}{H_i} = C_L$ is the energy loss coefficient.

The coefficient of reflection, C_r, coefficient of transmission, C_t and coefficient of energy loss, C_L, are functions of five variables:

$$C_r = f_r(\frac{H_i}{L}, kh, \frac{z}{h}, \frac{y}{h}, \frac{b}{L}) \tag{2.1}$$

$$C_t = f_t(\frac{H_i}{L}, kh, \frac{z}{h}, \frac{y}{h}, \frac{b}{L}) \tag{2.2}$$

$$C_L = f_L(\frac{H_i}{L}, kh, \frac{z}{h}, \frac{y}{h}, \frac{b}{L}) \tag{2.3}$$

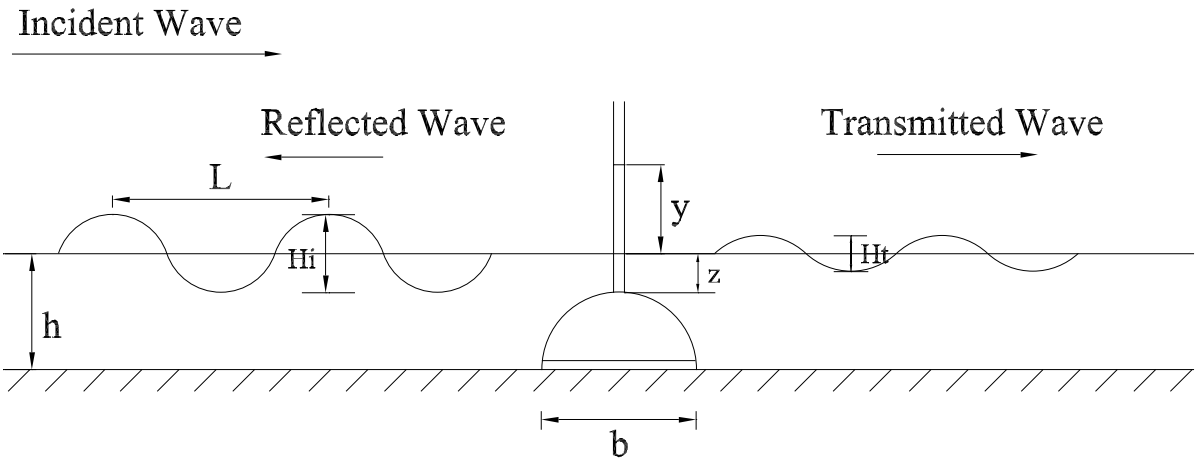

Figure 2.12: Dimensional parameters of the problem.

Chapter 3

Signal Analysis Procedures for Determining Reflection Coefficients

3.1 Introduction

In coastal and ocean engineering laboratory studies, incident and reflected wave parameters are usually obtained from experiments on regular waves. The situation is however complicated from end reflections and their effects on the propagating wave. Several methods have been proposed to obtain the reflection coefficient of regular waves over breakwaters. One method was proposed by Dean and Dalrymple [8] and involves traversing one wave probe in the direction of the wave propagation in order to measure the maximum H_{max} and minimum H_{min} wave heights of the composite wave field. The incident wave height H_i and reflection wave height H_r are then obtained from the formulas

$$H_i = \frac{H_{max} + H_{min}}{2} \tag{3.1}$$

$$H_r = \frac{H_{max} - H_{min}}{2} \tag{3.2}$$

H_{max} and H_{min} correspond to wave heights at a quasi-antinode and a node of the corresponding composite wave system, respectively. As a simplification to this approach, it has also been proposed by Dean and Dalrymple [8] to place two wave probes at fixed distances of $L/4$ and

$L/2$ from the reflecting structure, where L is the wave length. Both of these methods have slight difficulties and disadvantages. The first method has the disadvantage of being cumbersome to execute when many measurements are required. The second method may be inaccurate because of uncertainty of the locations $L/4$ and $L/2$ from the structure, particularly for a perforated or sloping structure. The latter method is also cumbersome when tests are carried out at a series of wave lengths. Furthermore, these methods do not provide the reflection phase angle.

For regular waves, there are three parameters that are to be determined: the incident wave height, the reflected wave height and the reflected phase. Several methods involving the use of two and three fixed wave probes ahead of the breakwater have also been developed so as to provide explicit solutions for the incident wave height and the height and phase of the reflected wave component. One of these methods, called the "resolution technique", uses two fixed wave probes at adjacent locations in front of the structure. It has been described by Thornton and Calhoun [34] and modified by Goda and Suzuki [12]. For this method, the measured wave parameters are two wave heights and one phase angle. The method has reasonable accuracy, except when the spacing between adjacent probes approaches an integer number of half wave lengths. In the present study, this method is adopted to obtain reflection coefficients for the suspended breakwater model and also is compared with the method developed here based on the wavelet theory. Another method, developed by Mansard and Funke [23], uses three fixed wave probes in front of the breakwater. It involves a least-squares fit to the measured wave parameters, which are three heights and two phase angles. This method fails for the case of equal probe spacing, when the spacing approaches an integer number of half wave lengths. As for the case of unequal probe spacing, the method fails at fewer, shorter wave lengths. Isaacson [15] described yet another method to obtain only the incident and reflected wave heights using three fixed wave probes to measure three wave heights. This method fails for the case of equal probe spacing, when the spacing approaches an integer number of quarter wave lengths. These three techniques are developed on the basis of linear wave theory to separate a two-dimensional wave field into incident and reflected wave components. A comparison of the range of application and accuracy of the latter methods, by Isaacson [15], revealed that a least-squares fit to the measured wave parameters from three fixed wave probes is the most accurate.

Some problems in conducting model experimental testing of breakwaters include the narrow

range of wave conditions and the difficulty to obtain long records. One major issue in conducting experimental model studies to determine reflection and transmission characteristics is the geometric limitations. These tests are usually conducted in a wave tank of limited size with end reflections. Also the techniques mentioned above are accurate for small amplitude incident waves where the wave dispersion relation, which estimates the wave number k, is valid. This is not the case in nature where waves with higher amplitude exist. High amplitude waves are also generated in a wave tank. A primary contribution of the present study involves the use of wavelet analysis to process the experimental data. The reflection wave component is determined by examining the temporal variations in the amplitude as well as phase of the wave over a time record from one fixed wave probe located ahead of the breakwater model. Wavelet analysis is used to separate the two parts of the record, which are then used to determine the reflection coefficient. The transmission coefficient is measured using a second wave probe that is placed behind the breakwater model.

The technique is based on the following experimental procedure. First, the wavemaker is brought into motion, generating waves of a prescribed amplitude and frequency. The waves propagate towards the breakwater model. The probe recording starts almost at the time when the experiment is initiated. Thus, the probe located ahead of the model would initially measure the incident wave component. Soon after, the waves interact with the breakwater, which reflects some of the wave energy. The reflected waves propagate backwards while the transmitted waves move on and reach the probe located behind the model. After a certain time lapse, the first probe would measure the total wave due to incidence and reflection from the breakwater model. Using the amplitudes and phases of the incident and composite waves, the reflection coefficient is determined.

In this chapter, the principles of the continuous wavelet transform and the basic characteristics of the Morlet wavelet are presented and discussed. The reliability of using wavelet analysis to separate a composite wave record is verified by a numerical example. We also discuss briefly the resolution technique. Typical reflection, transmission and energy loss coefficients for one set of measurements are obtained using both methods. At the end, a comparison between the two methods indicates the advantages of the method based on the wavelet analysis.

3.2 Standing and Partial-Standing Waves

To confirm the accuracy of the experimental methods, some experiments were carried out with no interfering model. The aim was to recover the classical patterns of a standing wave for total reflection and a partial-standing wave for partial reflection. Figure 3.1 is an example of an envelope of a regular standing wave in front of the vertical wall at the end of the wave tank. These data were obtained by traversing one wave probe in small increments of 8.89 cm (3.5 in) in the direction of the wave propagation. The η_{min} and η_{max} points of the envelope are the nodes and antinodes of the standing wave.

Figure 3.2 is an example of the envelope of a regular partial-standing wave in front of the absorbing beach when the slope angle was adjusted to be 28^o. One wave probe was traversed in small increments of 8.89 cm (3.5 in) in the direction of the wave propagation to measure the maximum H_{max} and minimum H_{min} wave heights of the composite wave field. The η_{min} and η_{max} points of the envelope are the quasi-nodes and quasi-antinodes of the partial-standing wave. The reflection coefficient, C_r, is calculated to be 0.20 using (3.1) and (3.2). This small value of C_r means that the beach does not absorb all the wave energy, but a small portion is reflected back from the vertical wall.

Experiments were also carried out with a breakwater model in order to recover a partial standing wave pattern in front of it. Figures 3.3, 3.4 and 3.5 are examples of envelopes of regular partial-standing waves of three different wave frequencies in front of the rigid hemi-cylindrical breakwater model. One wave probe was traversed in small increments of 8.89 cm (3.5 in) in the direction of the wave propagation to measure the maximum H_{max} and minimum H_{min} wave heights of the composite wave field. The reflection coefficients, C_r, are calculated to be 0.18, 0.22 and 0.23, for the three cases, respectively, using (3.1) and (3.2). Thus, some wave energy is reflected back from the breakwater model.

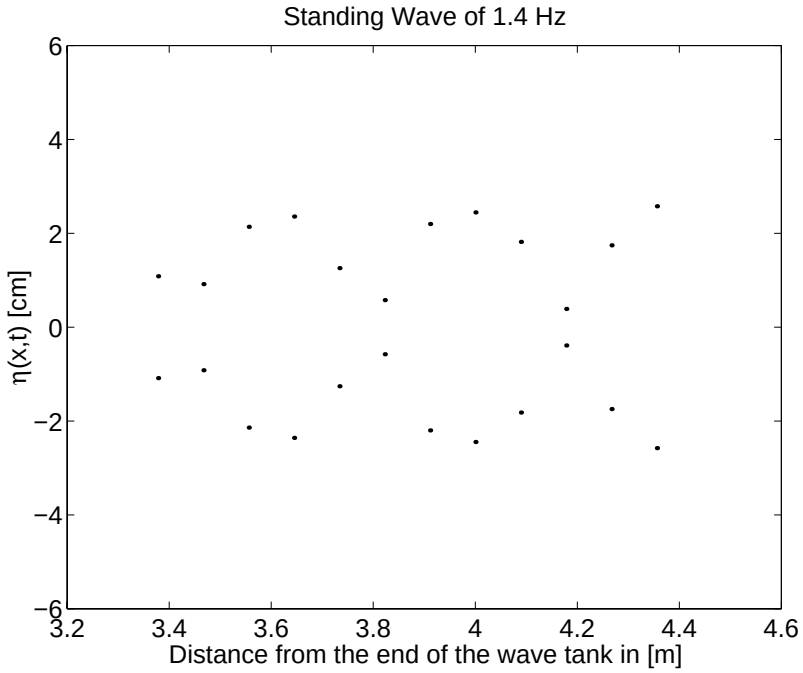

Figure 3.1: Envelope of standing wave in front of reflective wall at water depth of 25 cm.

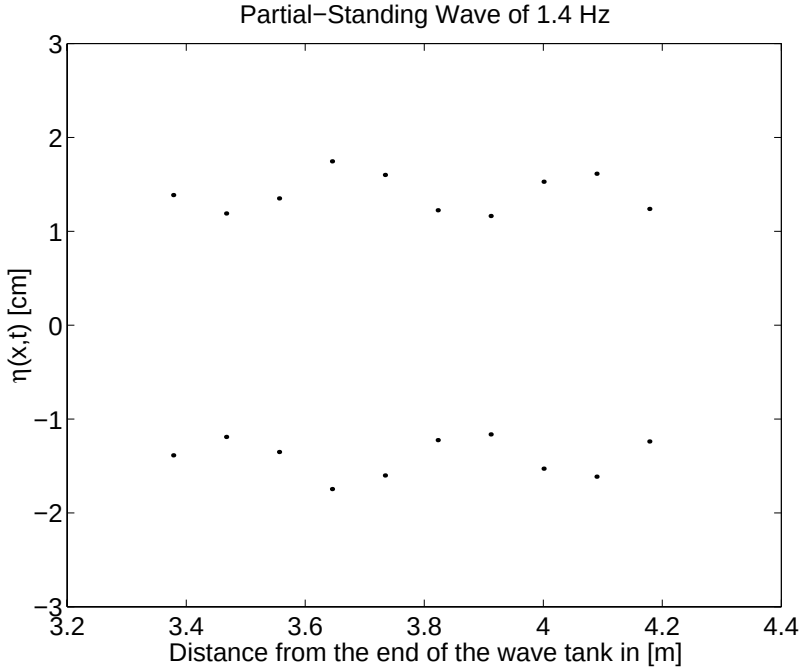

Figure 3.2: Envelope of partial-standing wave in front of the beach at water depth of 25 cm.

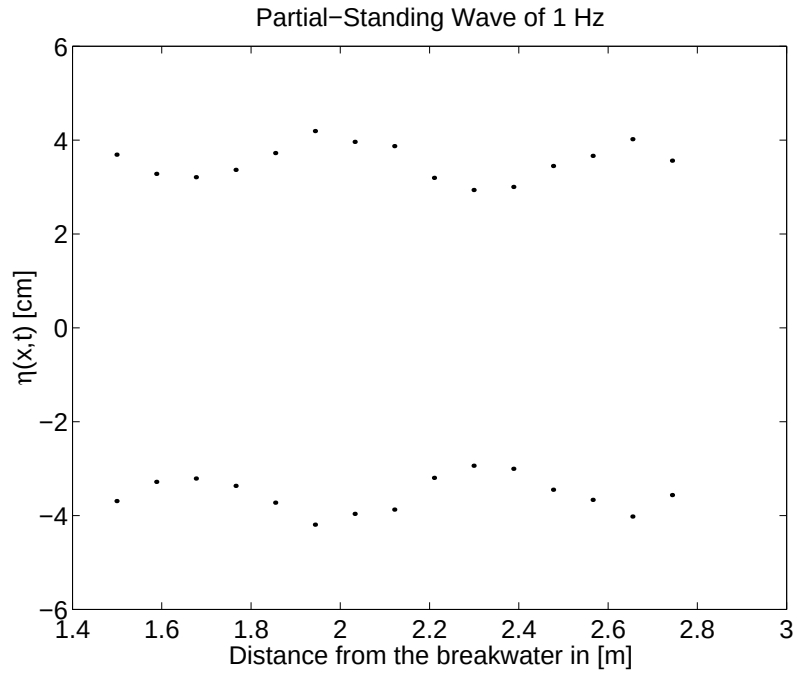

Figure 3.3: Envelope of partial-standing wave of 1 Hz in front of the rigid hemi-cylindrical breakwater model at water depth of 25 cm.

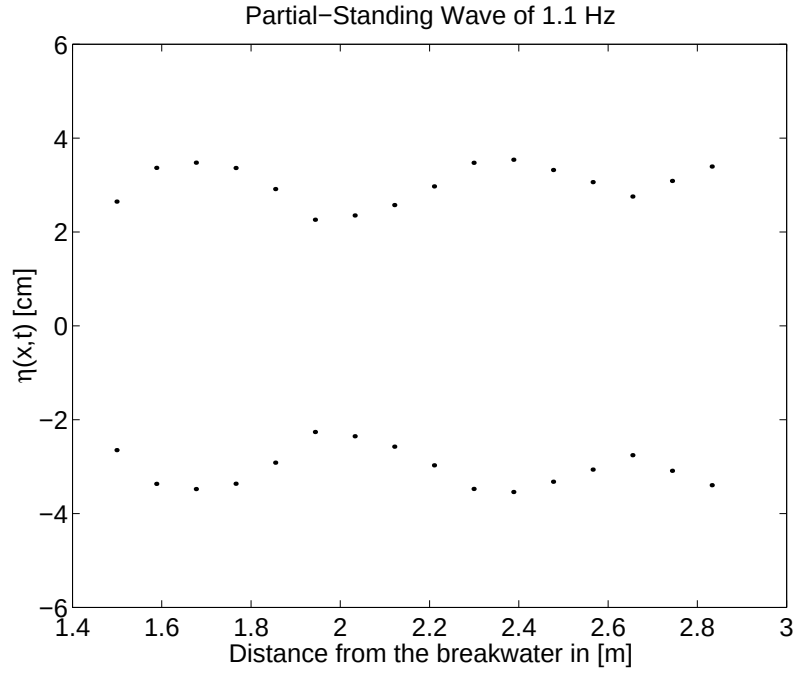

Figure 3.4: Envelope of partial-standing wave of 1.1 Hz in front of the rigid hemi-cylindrical breakwater model at water depth of 25 cm.

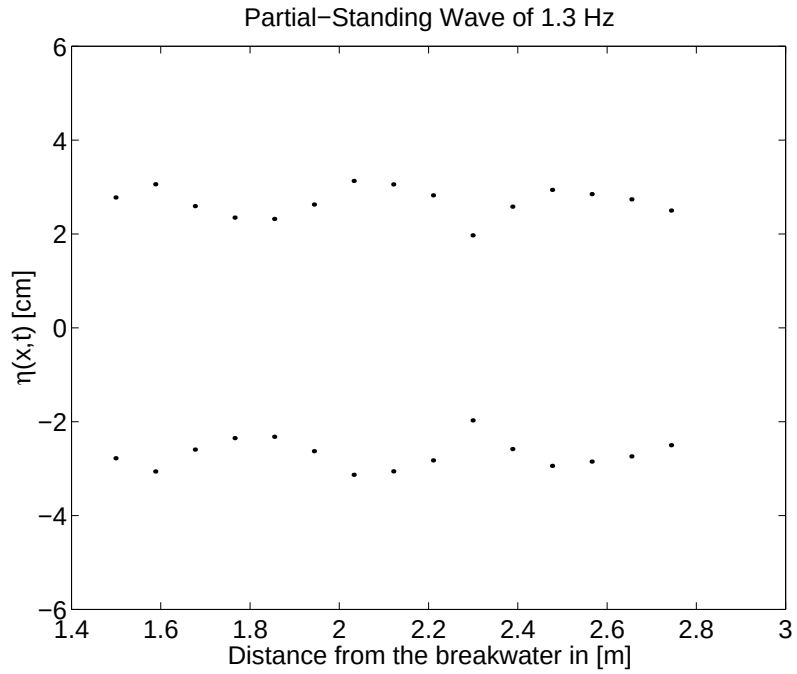

Figure 3.5: Envelope of partial-standing wave of 1.3 Hz in front of the rigid hemi-cylindrical breakwater model at water depth of 25 cm.

3.3 Wavelet Analysis

The separation of a wave record to identify incident and reflected wave components is performed with the use of a continuous wavelet. Here we chose the Morlet wavelet. The continuous wavelet transform, $W(a,\tau)$, of a function $g(t)$ is defined as the inner product integral between $g(t)$ and the complex conjugate of a wavelet family, $\Psi(a,t)$. It is given by

$$W(a,\tau) = \int_{-\infty}^{\infty} g(t)\Psi^*(a,t-\tau)\,dt \tag{3.3}$$

The wavelet family, $\Psi(a,t)$, is given by continuous translations and dilations of a mother wavelet, $\Psi(t)$, according to

$$\Psi(a,t-\tau) = p(a)\Psi(\frac{t-\tau}{a}) \tag{3.4}$$

where a is a dilation parameter, τ is a translation parameter and $p(a)$ is a scale weighting function. In this work, $p(a)$ is chosen as

$$p(a) = 2(\frac{\sqrt{2\pi}}{a}) \tag{3.5}$$

This choice makes the magnitude of the wavelet coefficients independent of the peak frequency of the mother wavelet (Teolis [32]). Transforming the convolution integral in (3.3) to the frequency domain and applying the Inverse Fourier Transform, the wavelet coefficients can be calculated as

$$W(a,\tau) = \frac{1}{2\pi}\int_{-\infty}^{\infty} \hat{g}(f)(\hat{\Psi}^*(a,f))e^{i2\pi f\tau}\,df \tag{3.6}$$

where $\hat{\Psi}^*(a,f)$ is the Fourier transform of $\Psi^*(\frac{t-\tau}{a})$ and $\hat{g}(f)$ is the Fourier transform of $g(t)$. The wavelet coefficient, $W(a,\tau)$, represents the contribution to $g(t)$ of scale a at time τ. Equation (3.6) is very useful for efficient numerical computation of the wavelet coefficients, which can be real or complex. For the Inverse Fourier Transform to exist, the wavelet function, $\Psi(t)$, must satisfy the admissibility condition (Kaiser [18]). For an integrable wavelet function, this condition implies that the function must have a zero mean.

One common complex wavelet is the Morlet wavelet, where the mother wavelet is given by a sinusoidal wave with a frequency of f_μ multiplied by a Gaussian function centered at $t = 0$ and

a standard deviation, σ_t, equal to $\frac{1}{2\pi f_\psi}$. The Morlet wavelet is given by

$$\Psi(t) = e^{i2\pi f_\mu t} e^{-\frac{(2\pi f_\psi t)^2}{2}} \tag{3.7}$$

The ratio $\frac{f_\mu}{f_\psi}$ is a dimensionless parameter, denoted here by γ. An example of a Morlet mother wavelet of $\gamma = 6$ and $f_\mu = 0.7$ is presented in Figure 3.6, which shows the real and imaginary parts of (3.7). Note that the Morlet wavelet is only marginally admissible since it has a zero mean only when a correction term is added. However, when γ is set to 6, the correction term is unnecessary since it is of the same order as a computer round-off error. The Fourier transform of the complex conjugate of the Morlet wavelet is real and is given by

$$\hat{\Psi}^*(f) = \frac{1}{\sqrt{2\pi}} e^{-\frac{(f-f_\mu)^2}{2{f_\psi}^2}} \tag{3.8}$$

Based on (3.4) and (3.5), the Morlet wavelet family is given by

$$\Psi(a,t) = 2\frac{\sqrt{2\pi}}{a} e^{\frac{i2\pi f_\mu t}{a}} e^{-\frac{(2\pi f_\psi t)^2}{2a^2}} \tag{3.9}$$

The Morlet wavelet family in the frequency domain is then given by

$$\hat{\Psi}^*(a,f) = 2e^{-\frac{(af-f_\mu)^2}{2{f_\psi}^2}} f \geq 0 \tag{3.10}$$

and

$$\hat{\Psi}^*(a,f) = 0 f < 0 \tag{3.11}$$

Alternative forms of (3.9) and (3.10) in terms of γ are

$$\Psi(a,t) = 2\frac{\sqrt{2\pi}}{a} e^{\frac{i2\pi f_\mu t}{a}} e^{-\frac{(2\pi f_\mu t)^2}{2(a\gamma)^2}} \tag{3.12}$$

$$\hat{\Psi}^*(\gamma,a,f) = 2e^{-\frac{\gamma^2(af-f_\mu)^2}{2{f_\mu}^2}} \tag{3.13}$$

In the frequency domain, the Morlet wavelet presents a band-pass filter. The magnitude of the Fourier transform of the Morlet wavelet, presented in Figure 3.6, is shown in Figure 3.7.

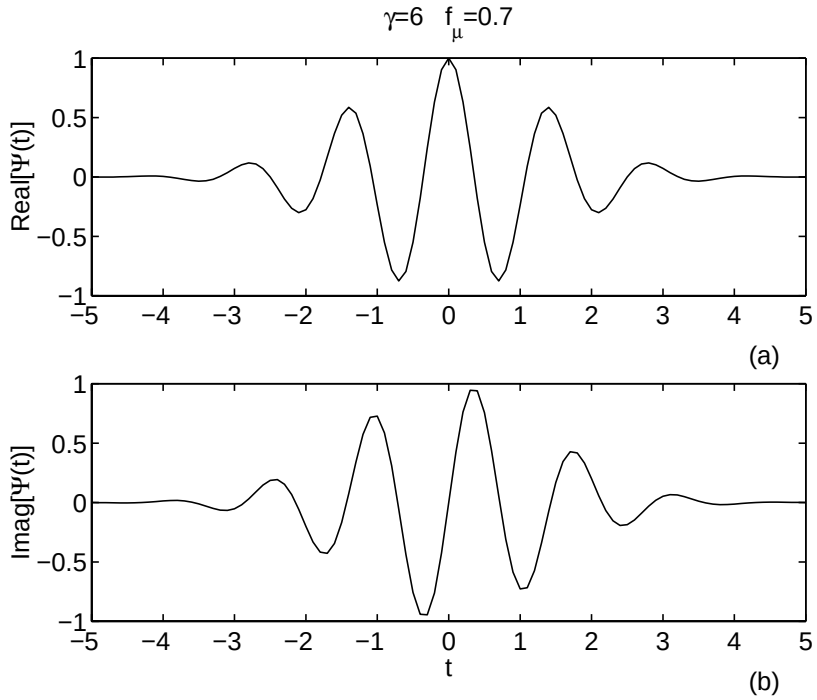

Figure 3.6: Complex-valued Morlet wavelet: (a) real part, (b) imaginary part.

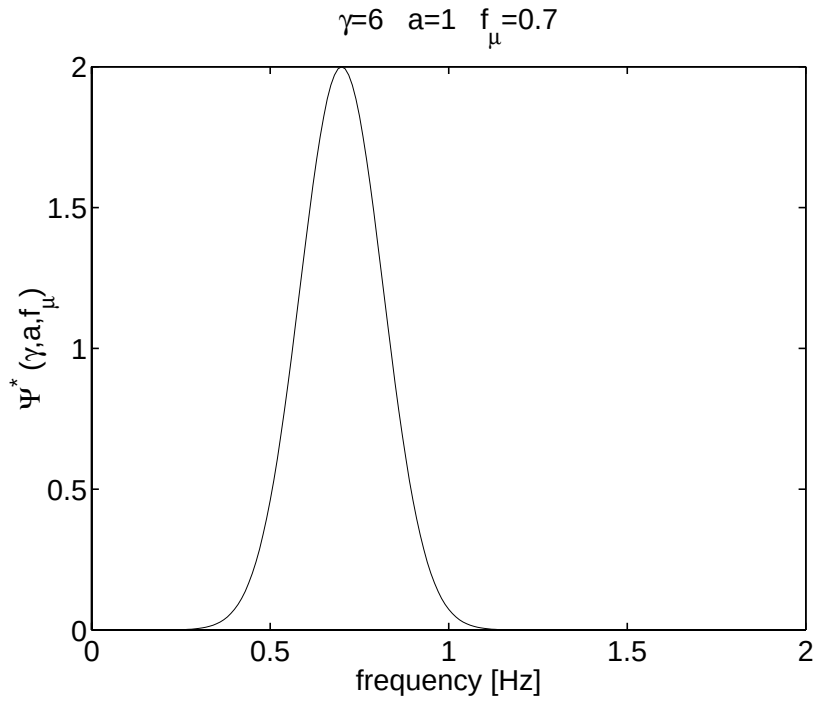

Figure 3.7: Frequency domain representation of the Morlet mother wavelet presented in Figure 3.6.

3.3.1 Characteristics and Implementation of Morlet Wavelet

In this section we provide several examples executing (3.7) and (3.13) for different values of γ, a and f_μ in order to gain insightful understanding of how each of these characteristics affects the shape of the Morlet wavelet in the time and frequency domains.

First, we present different families of Morlet wavelets. Different values of γ will produce unique families of Morlet wavelets, given in (3.13), with $a = 1$ being the mother wavelet. In Figure 3.8, three members of the Morlet family of $\gamma = 6$ in the frequency domain are shown. The peak frequency corresponding to the mother wavelet is $f_\mu = 0.7Hz$. The peak frequency, f_p, of a member of the family with larger scale a ($a > 1$) may be defined in reference to the mother wavelet, $f_p(a) = f_\mu/a$. An increase in wavelet scale, a, for the same γ corresponds to a decrease in the center peak frequency, f_p. Each member can be interpreted as a band pass filter centered at the frequency f_p. Note that the magnitude of the wavelet members is independent of the peak frequency and is always equal to 2. This results from the selection of the scale weighting function, $p(a)$, as given in (3.5). In Figure 3.9, three members corresponding to different $a's$ of the Morlet family of $\gamma = 20$ with peak frequency $f_\mu = 0.7Hz$ are shown.

For the same value of γ, if we compare two different mother wavelets ($a = 1$), one with $f_\mu = f_{\mu 1}$ and the other with $f_\mu = f_{\mu 2}$, where $f_{\mu 1} < f_{\mu 2}$, we note that the mother wavelet with frequency parameter $f_{\mu 2}$ is broader in the frequency domain with smaller temporal support in the time domain than the mother wavelet of $f_{\mu 1}$. An example of the magnitude in the frequency domain of two Morlet mother wavelets at the same $\gamma = 6$ having different frequency parameters, f_μ, is shown in Figure 3.10. The one with frequency $f_{\mu 2} = 1.4Hz$ is broader than the other with frequency $f_{\mu 1} = 0.7Hz$. Also, as shown in Figure 3.11, the temporal support of the Morlet wavelet with $f_{\mu 2} = 1.4Hz$ is smaller decaying faster to zero than the temporal support of the Morlet wavelet with $f_{\mu 1} = 0.7Hz$. A similar comparison of two mother wavelets with frequency parameters of 0.7 Hz and 1.4 Hz, respectively, for $\gamma = 20$ is shown in Figure 3.12. Again the real parts of the later Morlet mother wavelets, presented in Figure 3.13, show that the wavelet corresponding to a higher frequency parameter decays faster to zero.

Finally, we discuss the effect of the parameter γ when the peak frequency, f_μ and wavelet scale, a stay constant. In Figure 3.14, the magnitude of two Morlet mother wavelets with

frequency parameter f_μ of 0.7 Hz are compared when $\gamma = 6$ and $\gamma = 20$. The mother wavelet corresponding to larger γ is a subset of the mother wavelet with smaller γ. The mother wavelet with $\gamma = 20$ is a sharp band-pass filter and it also has larger temporal support in the time domain compared to the mother wavelet with $\gamma = 6$, as verified from their real parts shown in Figure 3.15. Another similar example presenting a mother wavelet with frequency parameter $f_\mu = 1.4Hz$, when $\gamma = 6$ and $\gamma = 20$, is shown in Figure 3.16. Again we see that the mother wavelet of $\gamma = 20$ is a subset of the mother wavelet of $\gamma = 6$. In Figure 3.17, we see that the real part corresponding to smaller $\gamma = 6$ decays faster to zero than the real part corresponding to larger $\gamma = 20$.

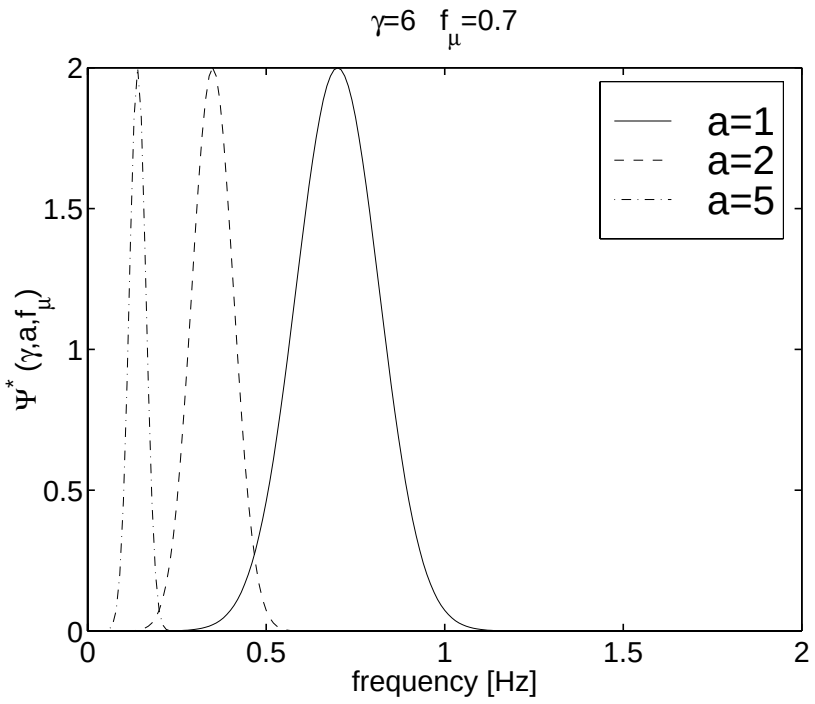

Figure 3.8: Frequency domain representation of three members of Morlet wavelet family, given in (3.13), with $\gamma = 6$.

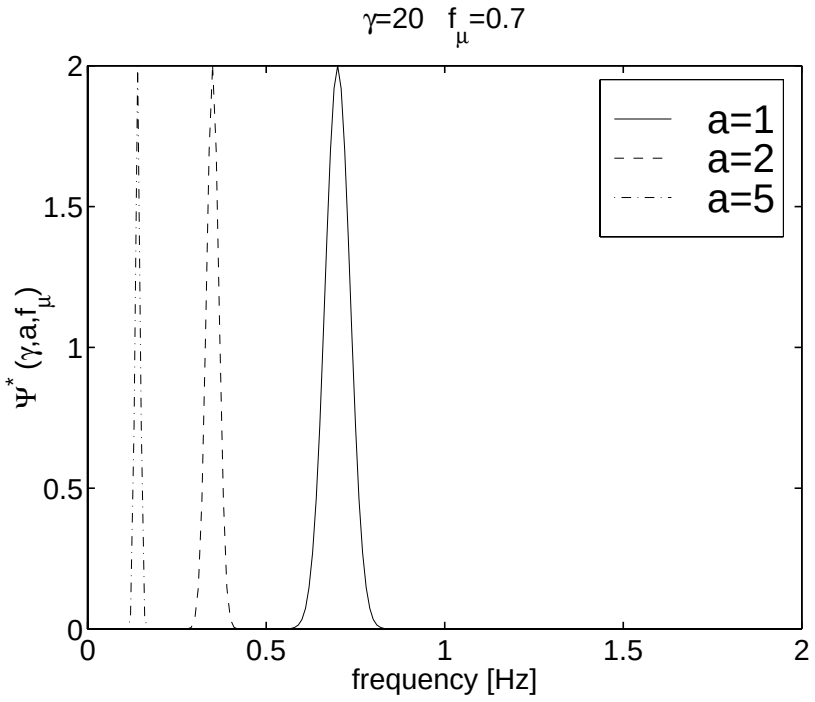

Figure 3.9: Frequency domain representation of three members of Morlet wavelet family, given in (3.13), with $\gamma = 20$.

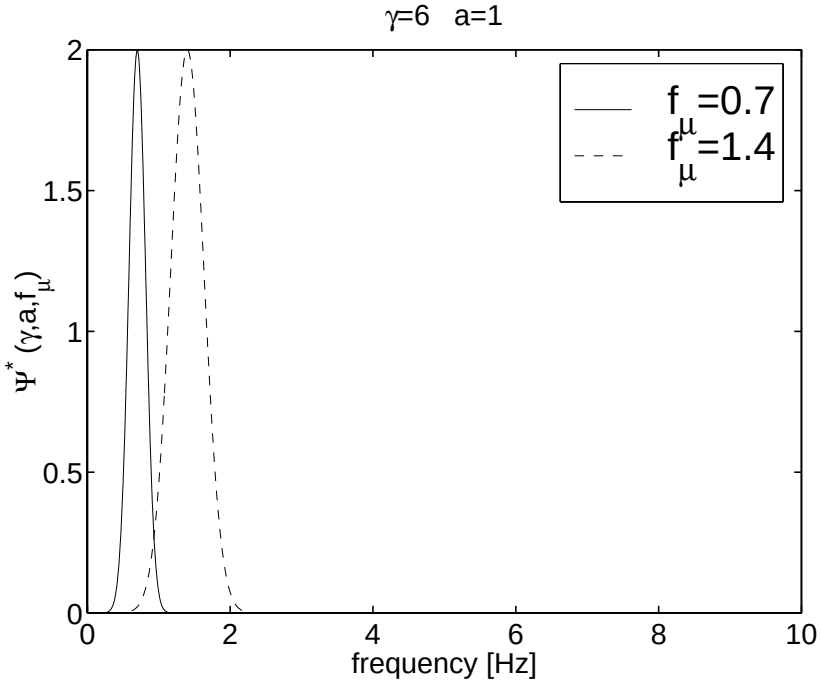

Figure 3.10: Frequency domain representation of two Morlet mother wavelets, one with frequency parameter f_μ of 0.7 Hz and another of 1.4 Hz at the same $\gamma = 6$.

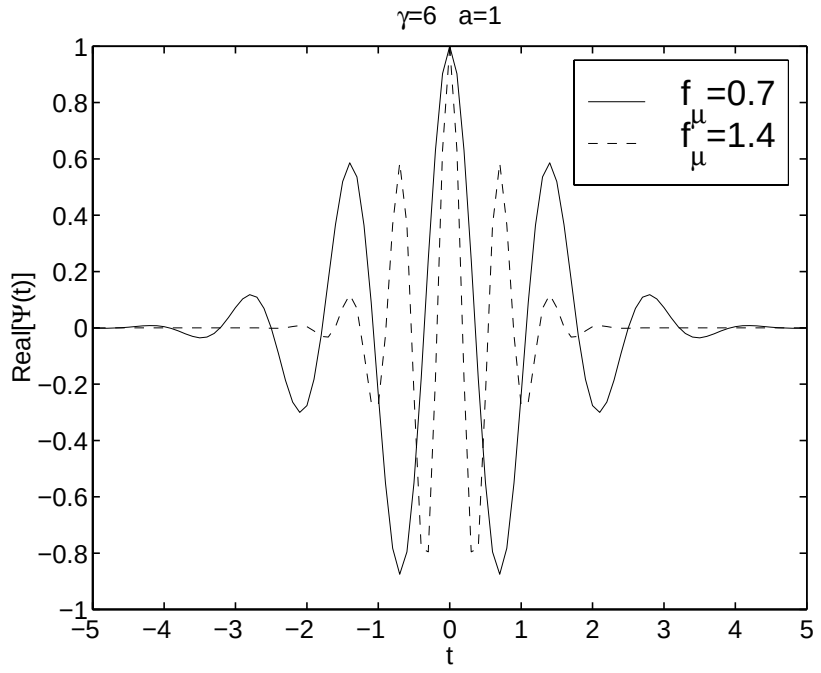

Figure 3.11: Real part of the Morlet mother wavelets presented in Figure 3.10.

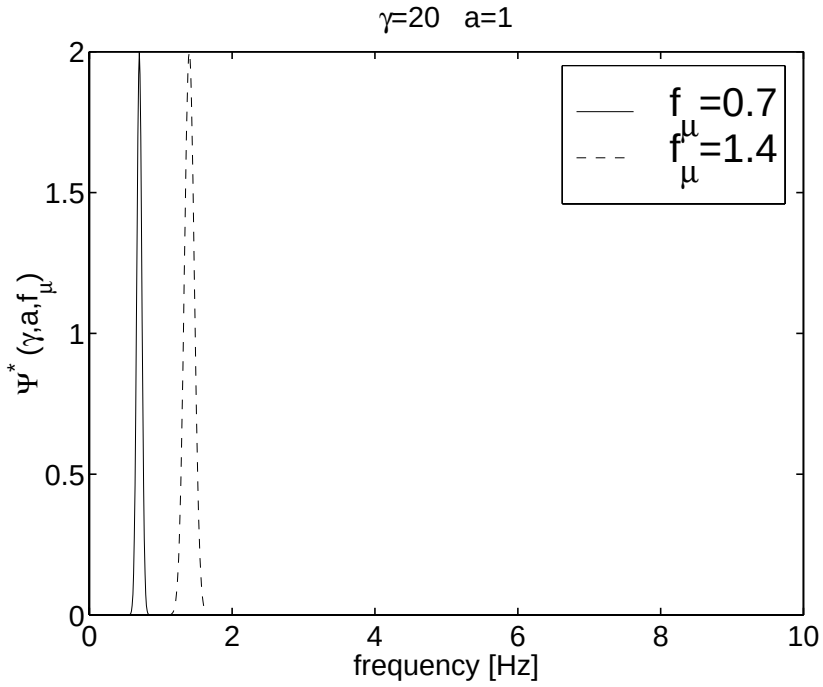

Figure 3.12: Frequency domain representation of two Morlet mother wavelets, one with frequency parameter f_μ of 0.7 Hz and another of 1.4 Hz at the same $\gamma = 20$.

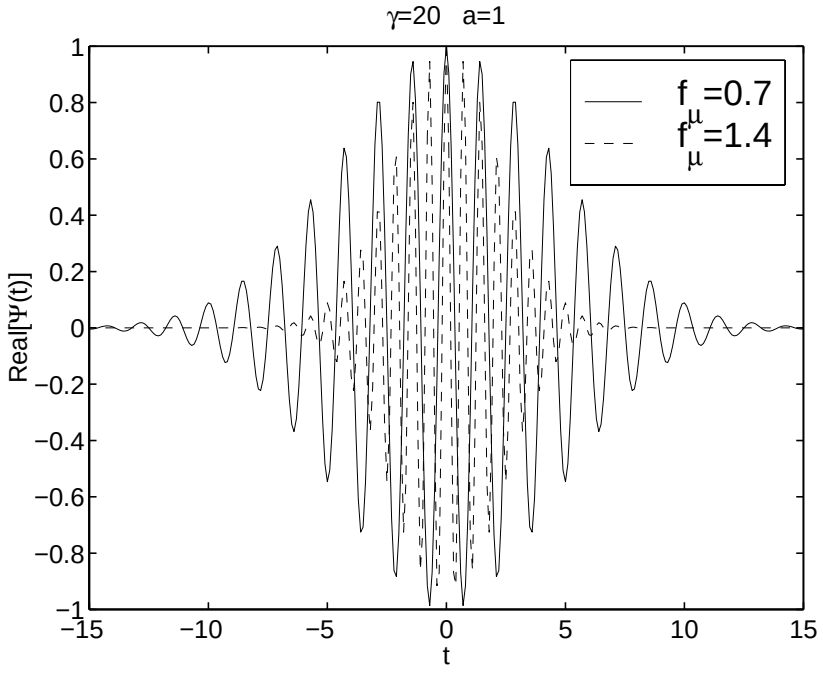

Figure 3.13: Real part of the Morlet mother wavelets presented in Figure 3.12.

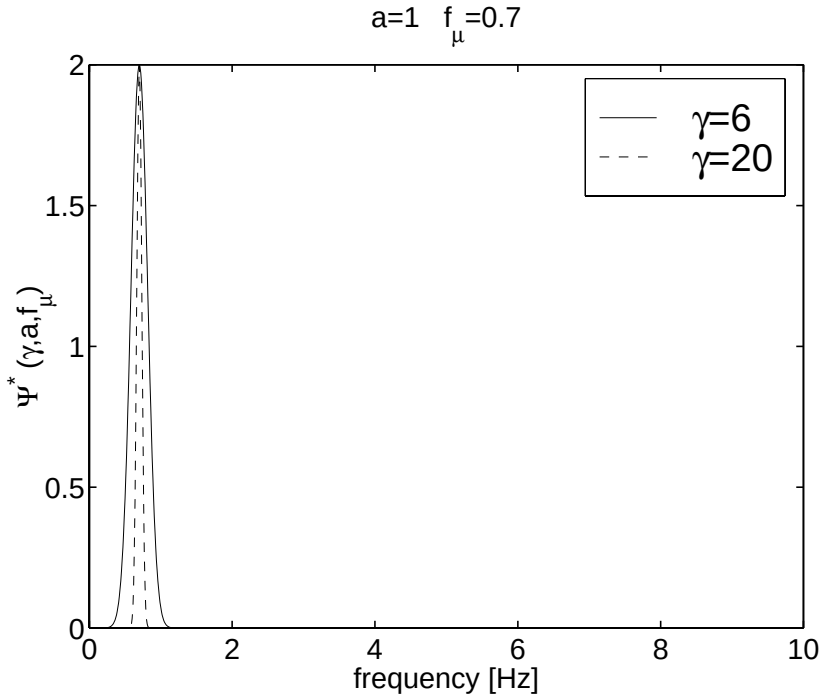

Figure 3.14: Frequency domain representation of Morlet mother wavelet with frequency parameter f_μ of 0.7 Hz when $\gamma = 6$ and $\gamma = 20$.

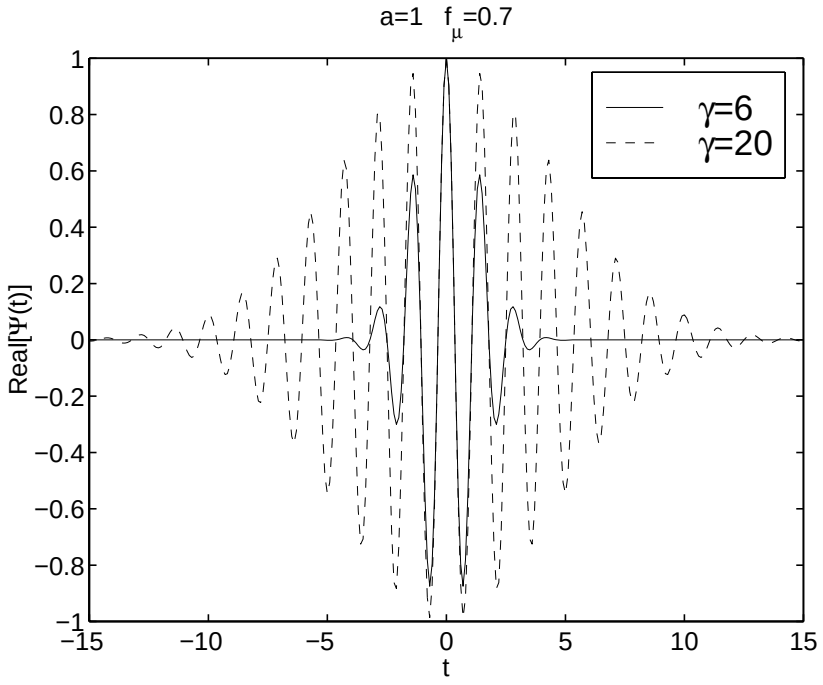

Figure 3.15: Real parts of the Morlet mother wavelets presented in Figure 3.14.

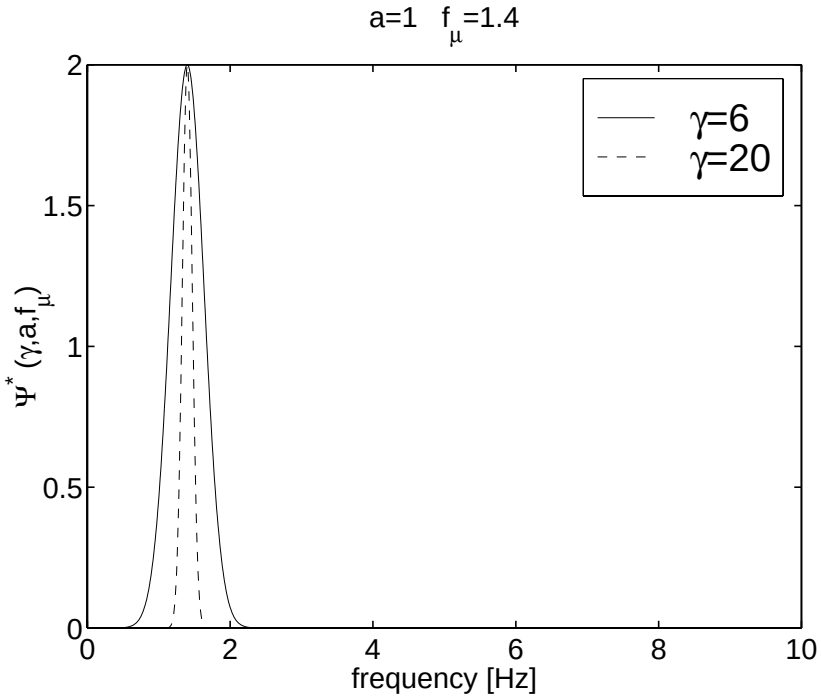

Figure 3.16: Frequency domain representation of Morlet mother wavelet with frequency parameter f_μ of 1.4 Hz when $\gamma = 6$ and $\gamma = 20$.

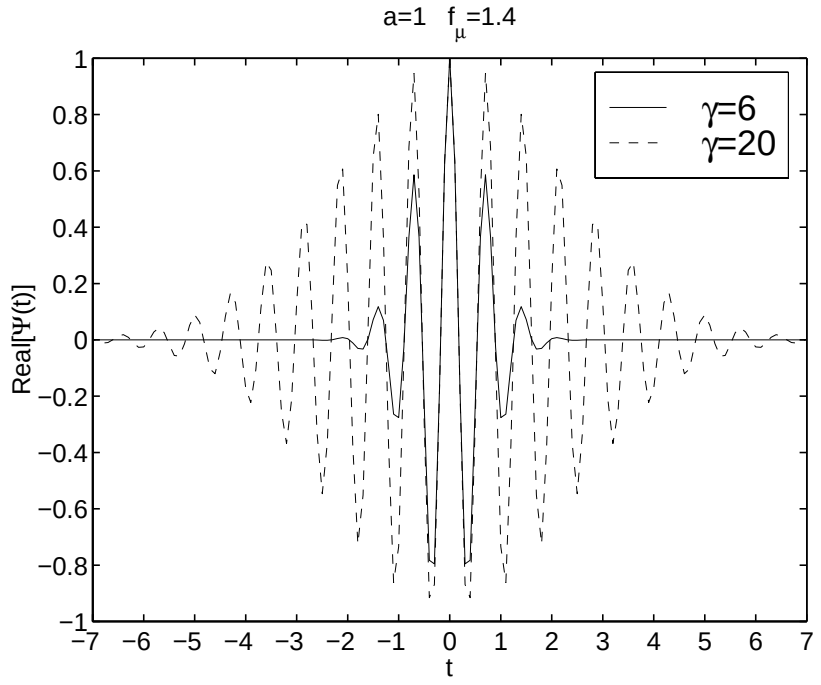

Figure 3.17: Real parts of the Morlet mother wavelets presented in Figure 3.16.

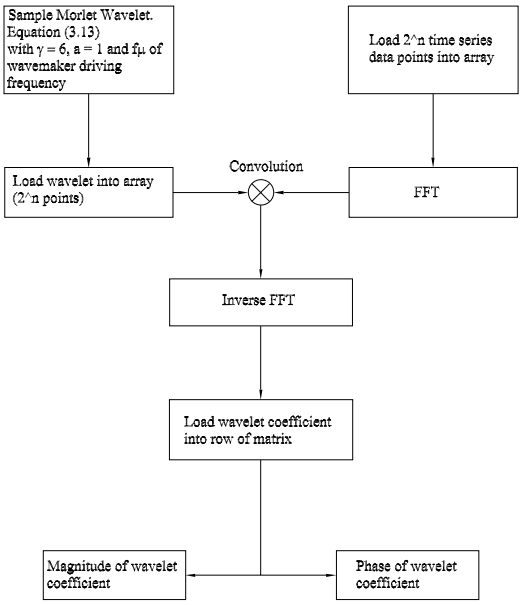

Figure 3.18: Diagram of digital continuous Morlet wavelet transform algorithm.

3.3.2 Numerical Algorithm for the Continuous Morlet Wavelet Transform

Because of the shifting property of the transform, the presence of $-\tau$ in (3.3), the wavelet transform of a function $g(t)$ at a given γ and scale, a, is a convolution integral between the function and the wavelet function at the given γ and scale, a. The basic algorithm for computing the Morlet wavelet transform is a convolution integral parameterized by the scale a and the parameter γ. The convolution is performed in the frequency domain to take advantage of the simplicity (multiplications) and efficiency of convolution in Fourier space. The diagram in Figure 3.18 illustrates the general procedure for performing the digital continuous Morlet wavelet transform. We should note here that in implementing the wavelet, we perform the sampling in the frequency domain and not in the time domain (Stamos et al. [29]). Moreover and since we are dealing with one wave component only, we perform the analysis for one scale only by considering a mother wavelet, $a = 1$, with a peak frequency, f_μ, that matches the frequency of the fundamental wave component of the measured signal.

Let's now apply the Morlet transform with $a = 1$, $\gamma = 6$ and frequency parameter, $f_\mu = 0.7Hz$

to one component cosine function given by $g(t) = 0.01\cos((2\pi 0.7)t + \pi)$. The cosine function, $g(t)$, is shown in Figure 3.19. Also shown in Figure 3.19 is the magnitude of the wavelet coefficient, $|W|$, at $f_\mu = 0.7Hz$ as defined in equation (3.6). As expected, it is the envelope of the cosine function, $g(t)$, and is equal to 0.01. The phase of the wavelet coefficient, ϕ, for the same parameters, γ and f_μ, is presented in Figure 3.20. It varies between $-\pi$ and π. If this phase is unwrapped and the $(2\pi 0.7)t$ component is subtracted, the result, ϕ_W, is the phase of the cosine function, $g(t)$, equal to π.

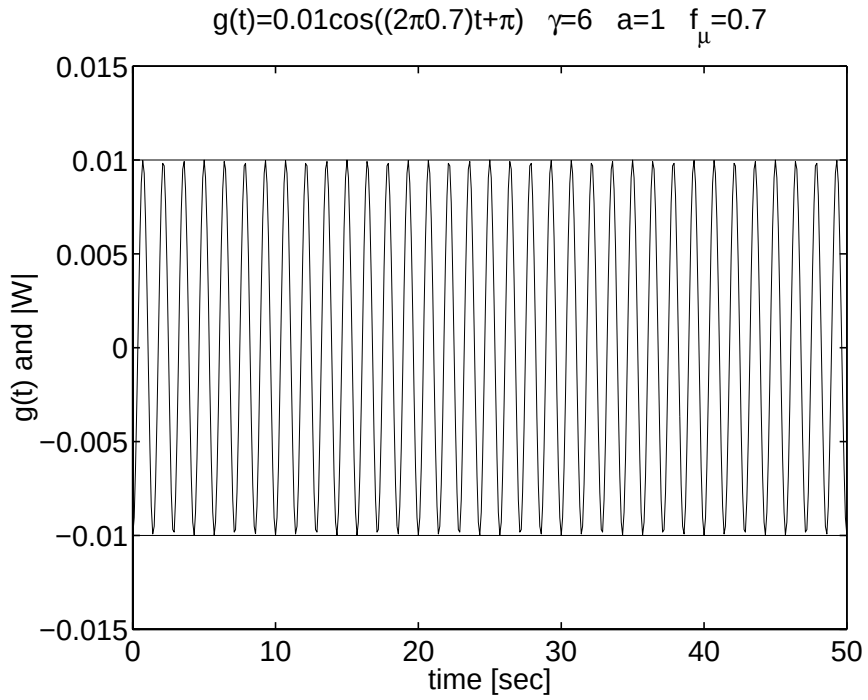

Figure 3.19: Cosine function $g(t)$ and magnitude of the mother wavelet coefficient at $f_\mu = 0.7Hz$ with $\gamma = 6$.

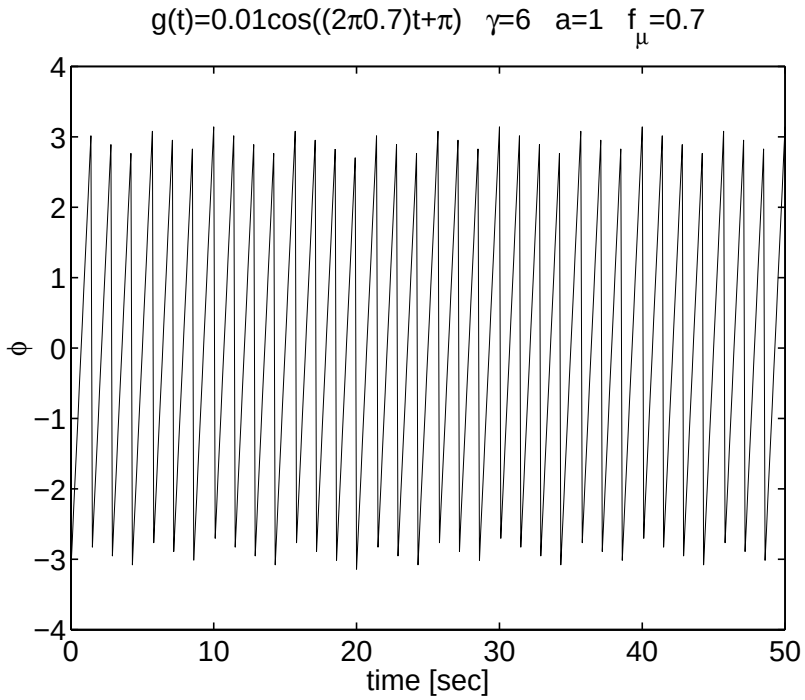

Figure 3.20: Phase of the mother wavelet coefficient at $f_\mu = 0.7Hz$ with $\gamma = 6$.

3.3.3 Numerical Example

In this section, we provide a numerical example to show how we use the Morlet wavelet to separate incident and reflected wave components. This example is obtained by considering two superimposed cosine waves that represent propagating incident and reflected waves in a wave tank as

$$\eta(x,t) = \eta_i(x,t) + \eta_r(x,t) = \alpha_i cos(\sigma t - kx + \phi_i) + \alpha_r cos(\sigma t + kx + \phi_r) \tag{3.14}$$

where $\eta(x,t)$ is the surface elevation from the mean water level, $k(= 2\pi/L)$ is the wavenumber with L being the wave length, $\sigma(= 2\pi f)$ is the angular frequency of the wave with f being the wave frequency, α is the wave amplitude, t is the time, x is the horizontal distance of the measuring point from the wavemaker, ϕ is the phase and subscripts i and r denote the incident and reflected wave components, respectively. In a wave tank experiment, a wave probe located ahead of the breakwater model will first measure the incident wave. After a certain time lapse, the reflected wave will reach the probe, which will then measure the total elevation of the composite wave. The wave periods of the incident and reflected wave components will be the same. However, when the reflected wave component reaches the measuring probe it will introduce a phase change in the wave. In our analysis, we will use this phase change to separate the incident wave component from the composite wave.

The numerical signal as given in (3.14) is generated by letting $\alpha_i = 0.01m$, $\alpha_r = 0.005m$, $\phi_i = \pi$, $\phi_r = \frac{\pi}{2}$, $x = 10m$ and $f = 0.7Hz$. The wavenumber is computed to be $k = 3.361\frac{rad}{m}$, using the dispersion relationship (Dean and Dalrymple, [8])

$$\sigma^2 = gk \tanh kh \tag{3.15}$$

where $g = 9.81\frac{m}{sec^2}$ and h is the water depth, assumed to be 0.2 m.

It is also assumed that the incident wave is recorded undisturbed for 25 seconds. After this instant we start the reflected wave, which results in a composite wave. As explained above, this simulates the history of an experiment in our wave tank. Before presenting the analysis, it is important to discuss the selection of the parameter γ. For the numerical values chosen, the signal is presented in Figure 3.21. Also shown in Figure 3.21 is the magnitude of the wavelet coefficient, $|W|$, at $f_\mu = 0.7Hz$ as defined in (3.6) for two different $\gamma's$, 6 and 20. As explained

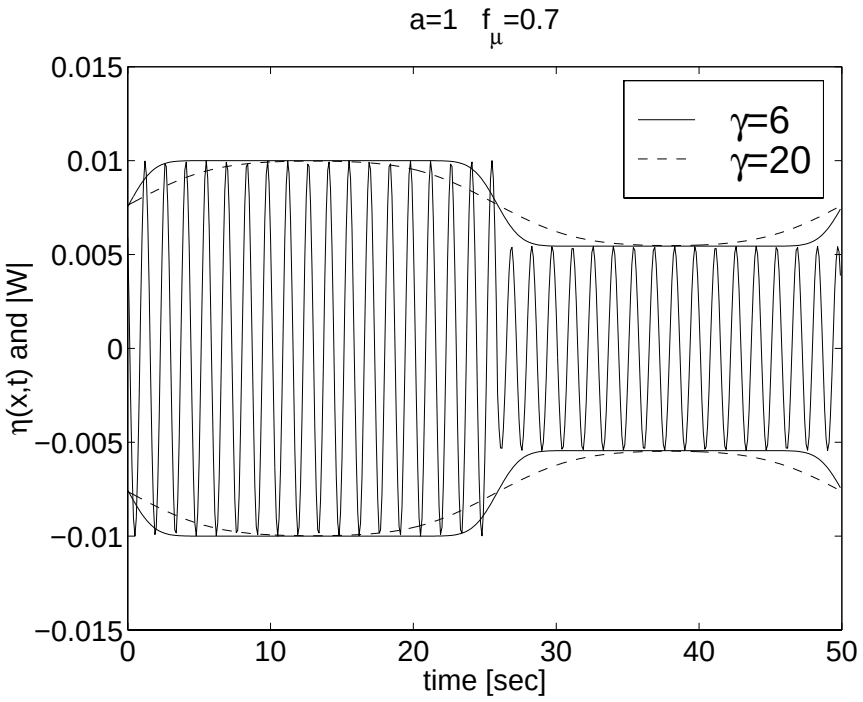

Figure 3.21: Signal generated by the numerical example given by (3.14) and magnitude of the wavelet coefficient at $f_\mu = 0.7Hz$ for $\gamma = 6$ and $\gamma = 20$.

in section 3.3.1, for a Morlet mother wavelet with large γ parameter the temporal support in the time domain is large. This means that its decay rate to zero is slower compared to a Morlet mother wavelet of a family with smaller γ. Thus, passing a mother wavelet of $\gamma = 20$ over a signal with an abrupt variation, as in the numerical signal at $t = 25sec$, the magnitude of the wavelet coefficient is smoother in the neighborhood of this time compared to the magnitude of the wavelet coefficient of a Morlet mother wavelet of $\gamma = 6$. Furthermore, if the phase of a wavelet coefficient is unwrapped and the $(2\pi f)t$ component is subtracted, the result, ϕ_W, is the phase of the signal $\eta(x,t)$ and is shown in Figure 3.22 obtained for two different γ values, namely 6 and 20. Again, using a value of $\gamma = 20$ results in smoothing the abrupt change of the signal phase at $t = 25sec$. Thus, for the application in this work, it is decided to use a Morlet wavelet with $\gamma = 6$ in order to obtain all the correct information from the signal.

For the numerical values chosen for (3.14), the signal is presented again in Figure 3.23-a. Also shown in Figure 3.23-a is the magnitude of the wavelet coefficient, $|W|$, for $\gamma = 6$ at $f_\mu = 0.7Hz$, as defined in (3.6). As expected, it is the envelope of the signal. Note that for $t < 25sec$, the magnitude of the wavelet coefficient, $|W|$, is equal to the amplitude of the incident wave

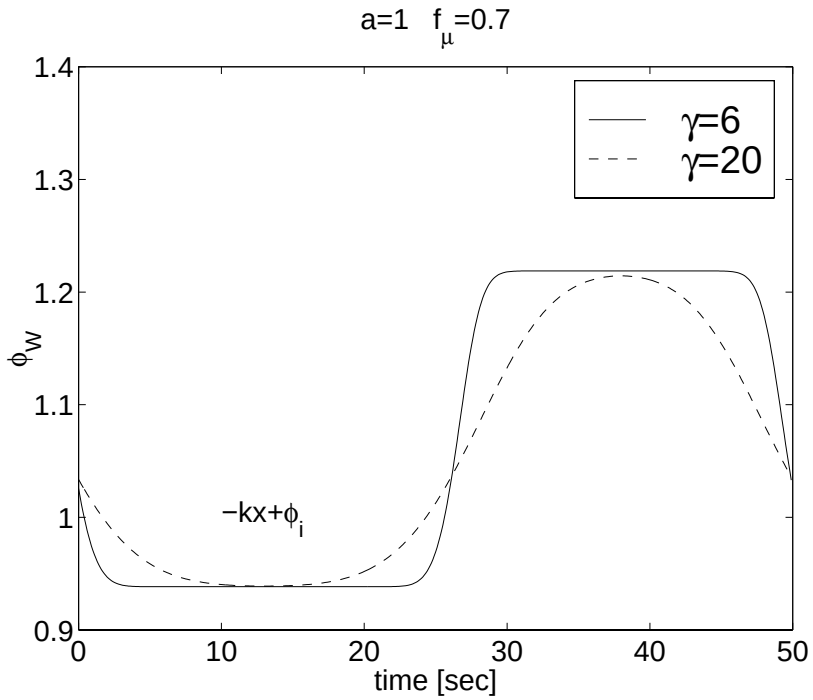

Figure 3.22: Phase of the wavelet coefficient at $f_\mu = 0.7Hz$ for $\gamma = 6$ and $\gamma = 20$.

component and for $t > 25sec$, the magnitude of the wavelet coefficient is equal to the amplitude of the composite wave, as given in (3.14).

The phase of the wavelet coefficient is independent of its magnitude and can thus provide additional information about the signal. If this phase is unwrapped and the $(2\pi f)t$ component is subtracted, the result, ϕ_W, is the phase of the signal $\eta(x,t)$ and is shown in Figure 3.23-b. For $t < 25sec$ the phase of the wavelet coefficient is equal to the total phase of the incident wave, given by $-kx+\phi_i$. Since the wavenumber k and the position x are known, we can recover the incident phase $\phi_i = \pi$. The phase of the wavelet coefficient for $t > 25sec$ is equal to the phase of the composite wave, $\eta(x,t)$. Note that the slight departure from actual values near $t = 0, 25, 50sec$ are due to end-effects, which results from the use of continuous wavelets.

The reflected wave component can be recovered by subtracting the incident wave component from the composite wave vectorially. A vectorial representation of the sum of the incident and reflected waves, such as the one given in (3.14), is shown in Figure 3.24. In this figure, $|W|$ and ϕ_W represent the amplitude and phase, respectively, of $\eta(x,t)$. For $t < 25sec$, the magnitude of the wavelet coefficient, $|W|$, is equal to α_i and the phase, ϕ_W, is equal to $-kx + \phi_i$. For

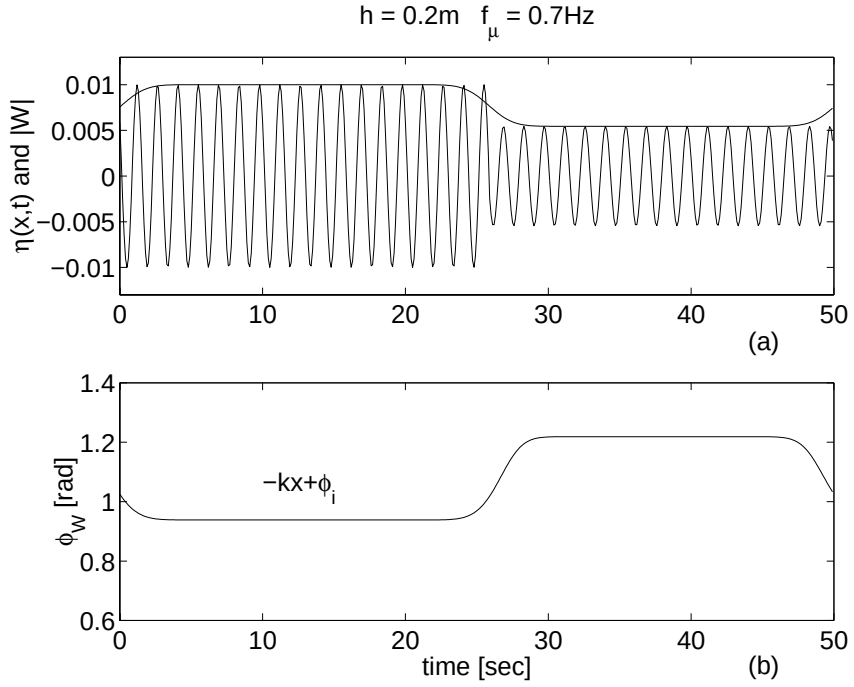

Figure 3.23: (a) Signal generated by the numerical example given by (3.14) and magnitude of the wavelet coefficient at $f_\mu = 0.7Hz$ and (b) phase of the wavelet coefficient at $f_\mu = 0.7Hz$.

$t > 25sec$, the magnitude of the wavelet coefficient, $|W|$, is the amplitude of the composite wave, which includes both incident and reflected wave components and ϕ_W is the phase of the composite wave. As shown in Figure 3.24, from the two sets of $|W|$ and ϕ_W, one can determine the amplitude, α_r, and the total phase, $kx + \phi_r$, of the reflected wave component. In Figure 3.25-a, we show the amplitude of the reflected wave, α_r. Note that, for $t < 25sec$, it is zero, since we record only the incident wave component. For $t > 25sec$, the amplitude of the reflected wave, α_r, is equal to 0.005, which is the value given to the reflected wave component in the example. Figure 3.25-b shows the total reflected phase, which is equal to $kx + \phi_r$ after 25 seconds. For $t < 25sec$, the phase does not have any significant meaning, since there was no reflected component. Since k and x are known, we are able to recover the reflected phase, $\phi_r = \frac{\pi}{2}$, as set in the example. This numerical example shows how wavelet analysis enables us to separate a reflected wave component from a composite wave using a signal from one location.

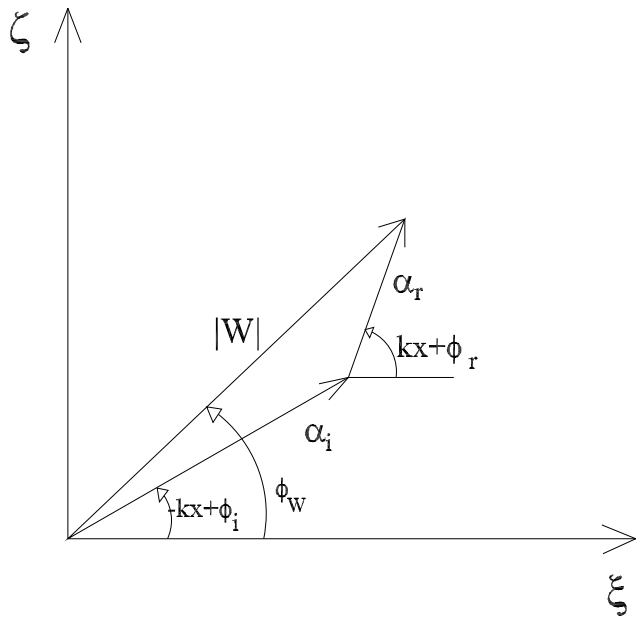

Figure 3.24: Vector representation of incident and reflected wave components.

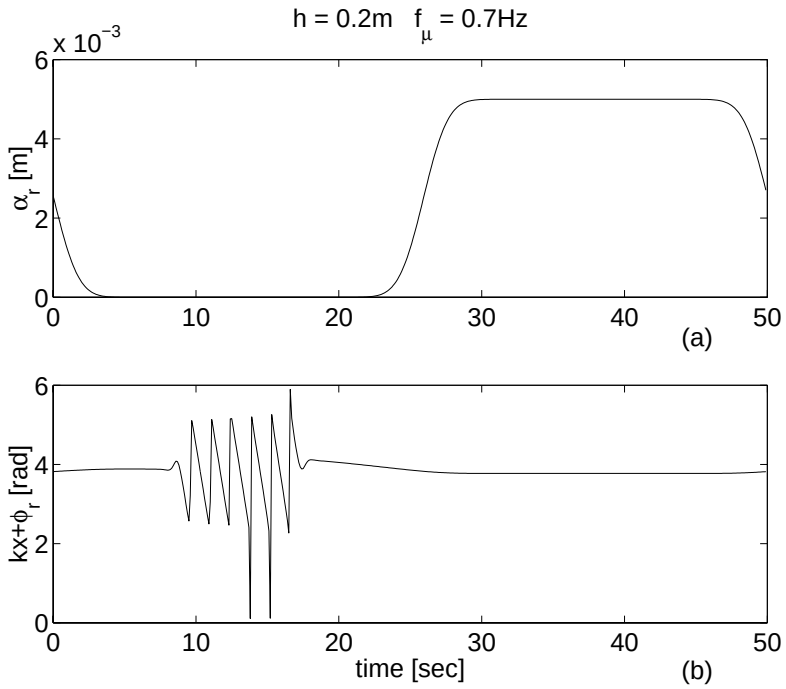

Figure 3.25: (a) Amplitude and (b) phase of the reflected wave component-Numerical example.

3.4 Resolution Technique

Another technique used to resolve the incident and reflected wave components from the records of composite waves is the resolution technique. This technique was developed on the basis of linear wave theory to separate a two-dimensional wave field into incident and reflected waves. The amplitudes of the incident, α_i and reflected, α_r waves can be resolved from the wave profiles $\eta_1(x,t)$ and $\eta_2(x,t)$ recorded at two positions x_1 and $x_2 = x_1 + \delta x$ in front of the breakwater according to (Goda and Suzuki [12])

$$\alpha_i = \frac{1}{2|\sin k\delta x|}\sqrt{(A_2 - A_1\cos k\delta x - B_1\sin k\delta x)^2 + (B_2 + A_1\sin k\delta x - B_1\cos k\delta x)^2} \quad (3.16)$$

$$\alpha_r = \frac{1}{2|\sin k\delta x|}\sqrt{(A_2 - A_1\cos k\delta x + B_1\sin k\delta x)^2 + (B_2 - A_1\sin k\delta x - B_1\cos k\delta x)^2} \quad (3.17)$$

For regular wave tests, wave profiles usually contain some higher harmonics. The Fourier amplitudes A_1, A_2, B_1 and B_2 corresponding to each frequency, either the fundamental, wavemaker-driving, frequency f or any higher harmonic, can be obtained from a Fast Fourier Transform analysis of the composite wave time series η_1 and η_2. A and B are the real and imaginary parts of Fourier coefficients and the subscripts 1 and 2 correspond to two seaward wave probes measuring the water elevation. The method yields good estimates of α_i and α_r, except when the spacing between the probes approaches an integer number of half wave lengths, $\delta x = n(L/2)$ with $n = 0, 1, 2, ...$, since the denominator of (3.16) and (3.17) becomes null. The dispersion relation (3.15) is used to calculate the wave number k for a specific angular wave frequency σ and water depth h.

The dispersion relation, (3.15), is valid for small amplitude waves. Such waves can be analyzed by linear wave theory as well as by Stokes' second order theory. The regular waves of finite amplitude are known to deviate from that relation. Any deviation from (3.15) leads to an inaccuracy in the estimates of α_i and α_r in (3.16) and (3.17) because they are based on the relative phase difference of $k\delta x$.

3.5 Typical Results for One Set of Measurements

In this section, we show how both methods, the one based on the wavelet theory and the other based on the resolution technique, can be applied to obtain reflection, transmission and energy loss coefficients from one set of measurements conducted for the suspended model. Two wave probes, spaced at 1.60 m apart, were located at 3.82 m ahead of the model. A third wave probe was also located at 2.59 m behind the model. A drawing of the experimental setup is presented in Figure 4.1, in Chapter 4.

3.5.1 Wavelet Analysis

Typical profiles of regular waves recorded ahead and behind the suspended breakwater model from the first probe and the third probe, respectively, are shown in Figure 3.26. The wavemaker frequency is set at 0.6 Hz and the water depth at 80 cm ($z/h = 0$). The first record, shown in Figure 3.26-a, consists initially of the incident wave component, $\eta_i(x,t)$. After an initial period, it contains the sum of the incident and reflected wave components (composite wave), $\eta(x,t)$. The second record, shown in Figure 3.26-b, contains the transmitted wave, $\eta_t(x,t)$. An analysis similar to the one presented in section 3.3.3 is conducted for the first record. The magnitude and the unwrapped phase of the wavelet coefficient at the wave component with $f_\mu = 0.6Hz$ are presented in Figures 3.27-a and 3.27-b, respectively. Estimates for the amplitude, α_i, and the total phase, $-kx + \phi_i$, of the incident wave component are obtained computing averages for the magnitude and phase of the wavelet coefficient between $t = 11.9sec$ and $t = 14.2sec$. The first time, $t = 11.9sec$, corresponds to a well-defined incident wave peak approaching the first probe. The second time, $t = 14.2sec$, corresponds to that peak arriving at the breakwater model. Based on these averages, we estimate α_i to be 1.277 cm and $-kx + \phi_i$ to be 5.315 rad. In Figure 3.28, we compare the estimated incident wave component (dashed line), obtained with these values for α_i and $-kx + \phi_i$, and the real part (solid line) of the wavelet coefficient at $f_\mu = 0.6Hz$ of the record shown in Figure 3.26-a. Note the good match over the time period between 9.2 and 16.6 seconds. This shows that the estimated incident wave component compares very well with the wave component of the measured signal over this part of the record, which consists of the incident component.

The reflected wave component is determined by subtracting vectorially the incident wave component, as determined above, from the composite wave. Estimates for the amplitude, α_r, and the total phase, $kx + \phi_r$, of the reflected wave component are obtained by computing averages for the amplitude and phase of the reflected component obtained from the vectorial subtraction between $t = 16.6sec$ and $t = 24sec$. The first time, $t = 16.6sec$, corresponds to a composite wave peak approaching the first probe, and the second time, $t = 24sec$, corresponds roughly to a re-reflected wave peak from the wavemaker approaching it again. Based on these averages, we calculate α_r to be 0.102 cm and $-kx + \phi_r$ to be 0.339 rad.

The magnitude of the wavelet coefficient is also calculated at the wave component at $f_\mu = 0.6Hz$ for the transmitted signal, shown in Figure 3.26-b. An estimate for the amplitude, α_t, of the transmitted wave is obtained computing an average value for the magnitude of the wavelet coefficient between $t = 9.2sec$ and $t = 17.8sec$. The first time, $t = 9.2sec$, corresponds to a well-defined wave peak approaching the probe behind the breakwater model, and the second time, $t = 17.8sec$, corresponds to that peak arriving at the end of the wave tank. Based on this average, we calculate α_t to be 1.149 cm. Based on the above estimates for α_i, α_r and α_t, the reflection coefficient, C_r, is calculated to be 0.08 and the transmission coefficient, C_t, to be 0.90. The energy loss coefficient, C_L, is found to be about 0.43 using (1.1). Thus, most of the wave energy for this experimental test is transmitted and the lowest portion is reflected.

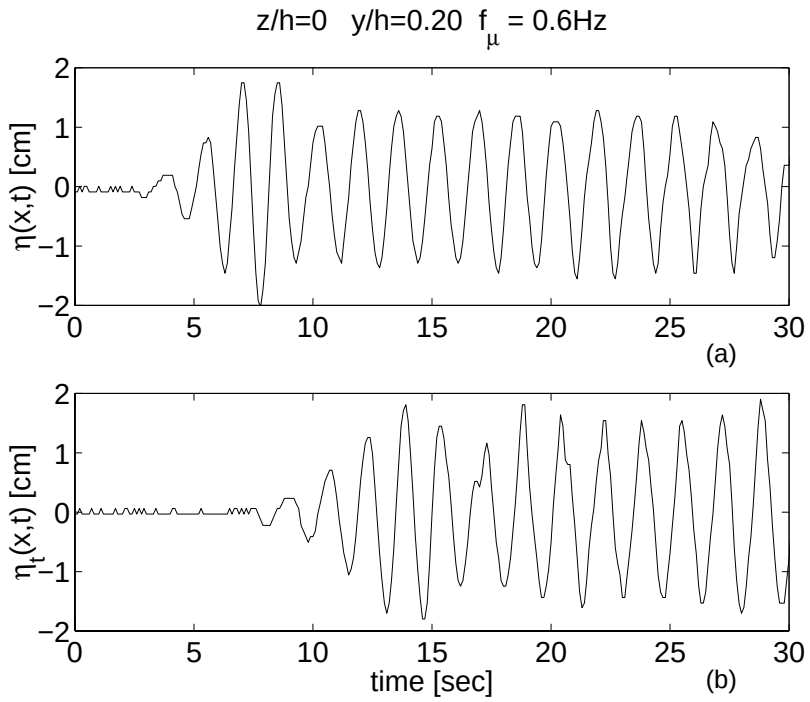

Figure 3.26: Typical regular wave profiles at two locations: (a) ahead of and (b) behind the suspended breakwater model.

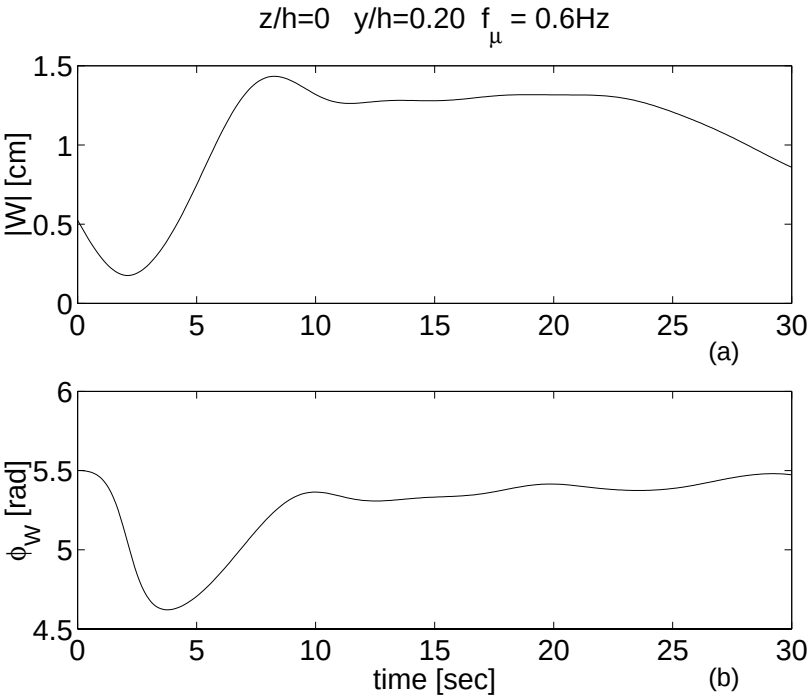

Figure 3.27: Magnitude (a) and phase (b) of the wavelet coefficient at the frequency of the fundamental wave component in the record shown in Figure 3.26-a.

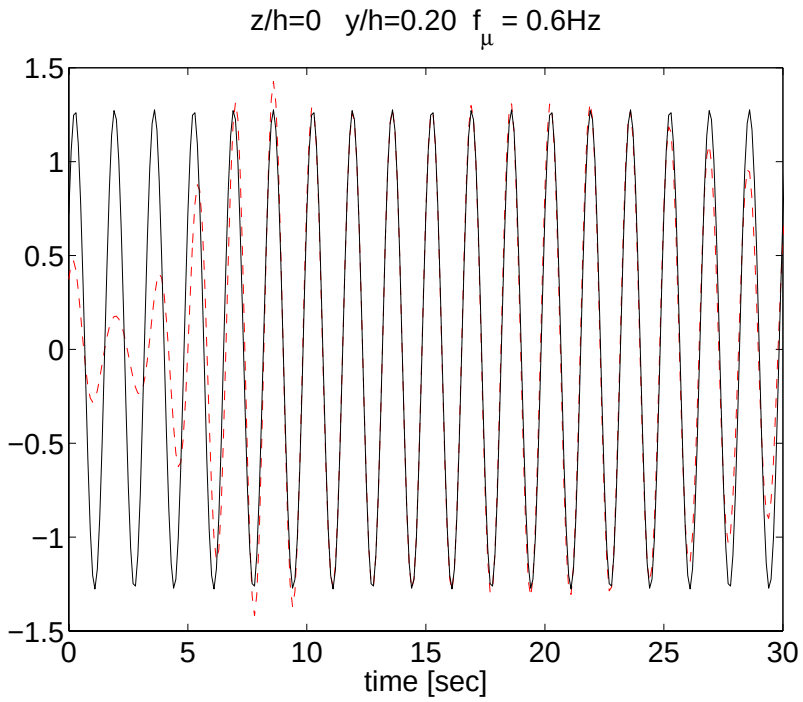

Figure 3.28: Real part of the estimated incident wave component (solid line) and real part (dashed line) of the wavelet coefficient at the frequency of the fundamental wave component.

3.5.2 Resolution Technique

The same typical profiles of regular waves at 0.6 Hz, as presented in section 3.5.1, adding also the record of the second wave probe, are shown in Figure 3.29. The first two records ahead of the model, shown in Figures 3.29-(a) and 3.29-(b), contain the sum of the incident and reflected waves. Special care is necessary to remove the initial portion of the signal from the upstream time series, which does not include the reflection from the breakwater model, as well as the final portion, which is contaminated by subsequent reflections. These are generated when the wave reflected from the model encounters the wavemaker, is reflected again and propagates again in the same direction with the incident wave. The final record length to be analyzed depends on the wave speed and differs for each wavemaker-driving frequency. The third record, shown in Figure 3.29-(c), shows the transmitted wave.

Typical plots of the corresponding composite wave spectra and transmitted wave spectra are shown in Figure 3.30. The spectra shown in Figure 3.30-(a) are the spectra of the composite records shown in Figures 3.29-(a) and 3.29-(b), and the spectrum shown in Figure 3.30-(b) is the spectrum of the transmitted record in Figure 3.29-(c). The composite waves can be resolved into the incident and reflected wave spectra components. Equations (3.16) and (3.17) are applied to estimate α_i and α_r for all the frequencies in the range $0 < f < 5Hz$. Plots of the resolved incident (solid line) and reflected wave (dashed line) spectra are shown in Figure 3.31 for a wavemaker-driving frequency of 0.6 Hz. The resultant estimates display peaks at the fundamental wave frequency and its harmonics. The estimated amplitudes at the peaks were employed as the representative amplitudes of incident and reflected waves. The peaks at the same frequencies, shown in Figure 3.31-b, are half of the amplitudes of the transmitted wave. We restricted our study to collect the estimated amplitudes α_i, α_r, and the measured amplitude α_t, only at the fundamental wave frequency. The estimates for α_i, α_r and α_t at the fundamental frequency 0.6 Hz are 1.278 cm, 0.08 cm and 0.548 cm, respectively. The wave coefficients C_r, C_t and C_L, are calculated based on these amplitudes. For the wave profiles, presented in Figure 3.29, the reflection coefficient, C_r, is found to be 0.06 and the transmission coefficient, C_t, to be 0.86. Based on (1.1), the energy loss coefficient, C_L, is found to be about 0.51. There is a very small deviation from the estimates of the wavelet analysis.

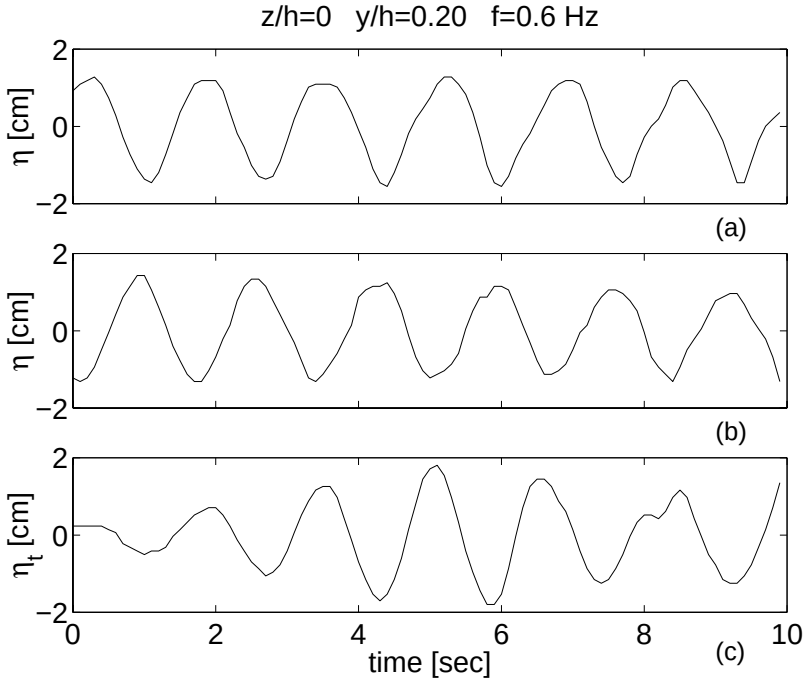

Figure 3.29: Typical regular wave profiles at three locations: (a) and (b) ahead of and (c) behind of the suspended breakwater model.

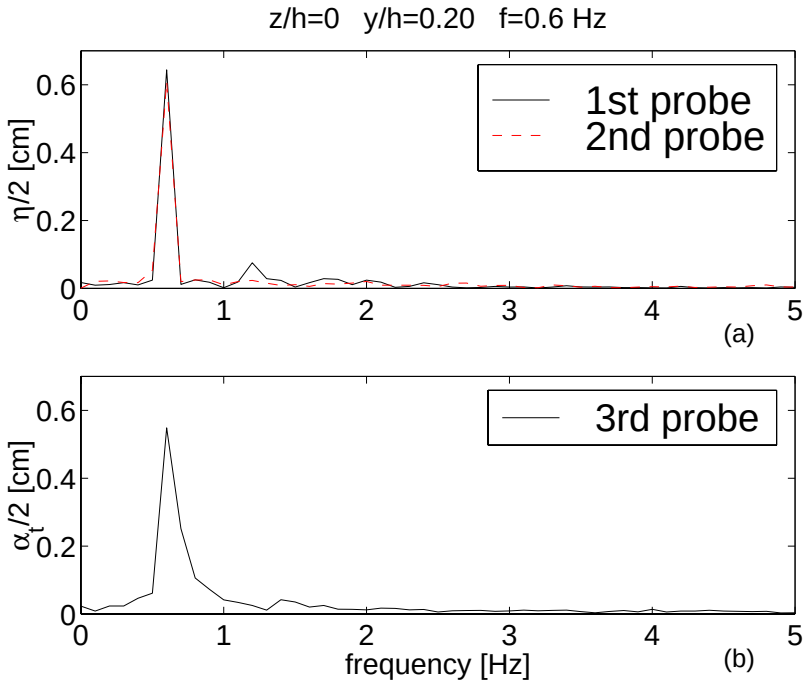

Figure 3.30: Typical plots (a) of composite and (b) of transmitted wave spectra.

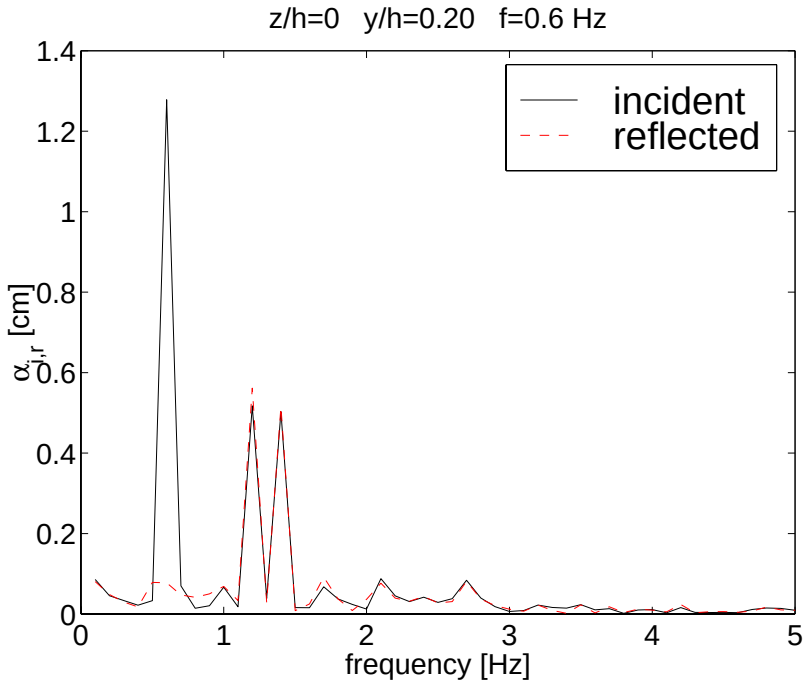

Figure 3.31: Typical plots of resolved incident (solid line) and reflected (dashed line) wave spectra.

3.6 Comparison between Wavelet Analysis and Resolution Technique

In this section, the two methods are compared, presenting estimates of reflection coefficients, C_r, for the suspended breakwater model. The analysis described in sections 3.5.1 for wavelet analysis and 3.5.2 for the resolution technique is performed on part of the records for the suspended flexible-sack under different internal pressures, wave frequencies and water depths.

Figure 3.32 shows the reflection coefficients, C_r, with the ratio of $\delta x/L$ estimated by the two methods at a water depth of 80 cm. As noted in section 3.4, the resolution technique yields good estimates of C_r, except when the spacing between the probes approaches an integer number of half wave lengths, $\delta x = n(L/2)$. Figure 3.32 indicates that there is a significant difference between the two methods when $\delta x/L$ matches this condition. Thus, when $\delta x/L$ is equal to 1.03, 1.48 and 2.01 the resolution technique estimates deviate from those of wavelet analysis. Surprisingly, there is a good match between the methods when $\delta x/L = 0.54$. At $\delta x/L = 1.73$, the measured wave amplitude is very close to the region where Stokes' third order theory is valid and where expressions for wave celerity and dispersion are not identical to those obtained by linear theory. Thus, a wrong estimate of the wavenumber k is obtained using (3.15), which leads to inaccurate estimates of α_i and α_r in (3.16) and (3.17). The regions of validity for various wave theories are obtained from Figure 2-7 in the Shore Protection Manual [7].

Figure 3.33 shows the reflection coefficients, C_r, with the ratio of $\delta x/L$ estimated by the two methods at a water depth of 90 cm. Again there is a significant difference between the methods when δx approaches an integer number of half wave lengths. Thus, when $\delta x/L$ is equal to 0.53, 1.03, 1.48 and 2.01 the resolution technique estimates deviate from those of wavelet analysis. Figure 3.34 also shows the reflection coefficients, C_r, with the ratio of $\delta x/L$ estimated by the two methods at water depth of 100 cm. The results show a significant difference between the methods when $\delta x/L$ is equal to 0.52, 1.03, 1.48 and 2.01. At $\delta x/L = 1.73$ the measured wave amplitude is in the region where Stokes' third order theory is applied. Thus, an inaccurate estimate of k is introduced in (3.16) and (3.17) using (3.15).

Based on the results obtained from the comparison of the two methods, we conclude that

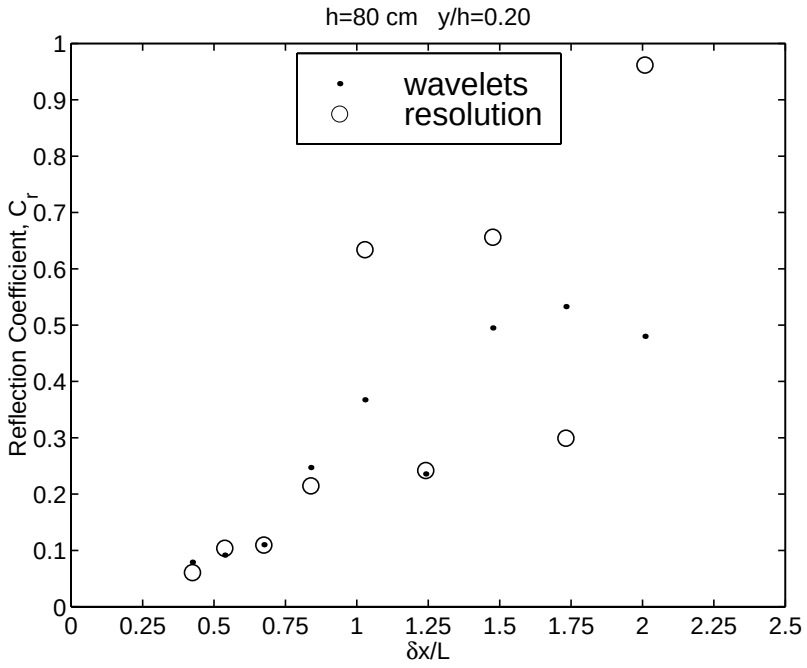

Figure 3.32: Comparison of reflection coefficients between wavelet analysis and resolution method for the suspended breakwater model. Water depth 80 cm.

our setup for the wave probes presented in the beginning of section 3.5 will not give accurate estimates of the reflection coefficients, C_r, using the resolution technique. Furthermore, for the resolution technique the dispersion relation (3.15) will give inaccurate estimates of the wave number, k, for high amplitude waves that are in the region where Stokes' higher order theories are applied. Thus, one more inaccuracy is added to the final estimates of α_i and α_r. For the reasons explained above, all the measured data for all breakwater models are processed and analyzed using the method based on the wavelet theory. The wave probes' setup does not influence the wavelet analysis. Moreover, high amplitude waves can be analyzed accurately since we are not using the wave number, k, to estimate α_i and α_r.

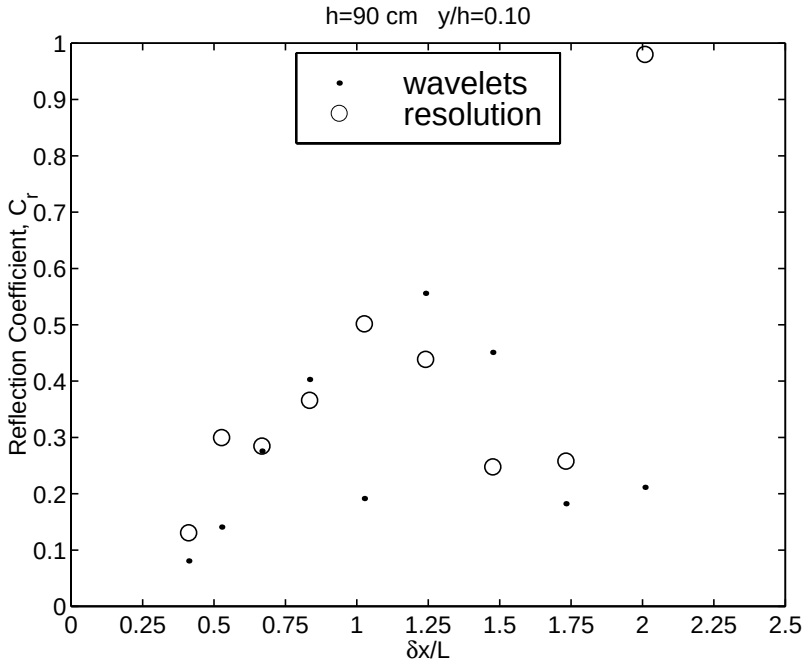

Figure 3.33: Comparison of reflection coefficients between wavelet analysis and resolution method for the suspended breakwater model. Water depth 90 cm.

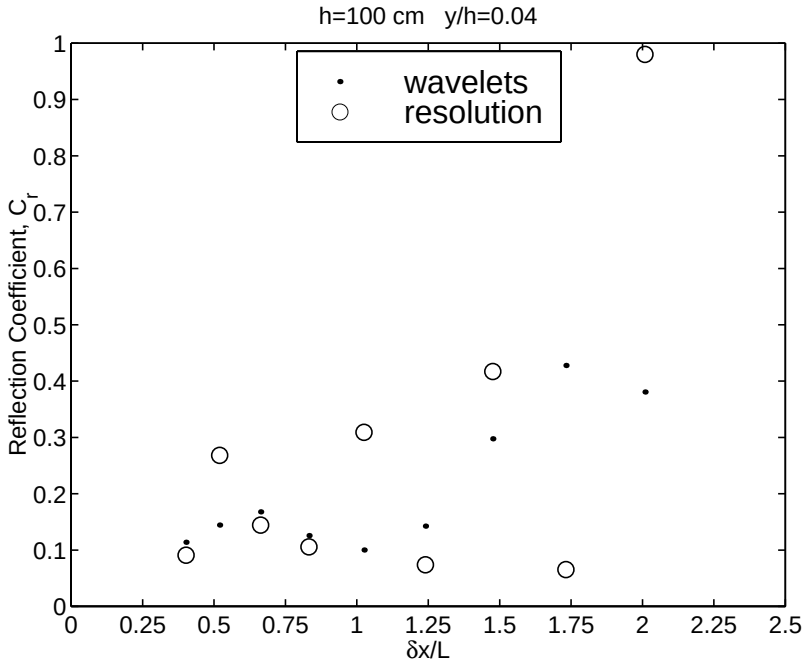

Figure 3.34: Comparison of reflection coefficients between wavelet analysis and resolution method for the suspended breakwater model. Water depth 100 cm.

Chapter 4

Wave Coefficients Over Suspended Flexible Breakwater

4.1 Introduction

In this chapter we present and discuss the reflection, transmission and energy loss coefficients of the suspended breakwater model. All the experiments were carried out in the Engineering Science and Mechanics (ESM) wave tank of Virginia Tech. A Wavetek 275 digital function generator was used to generate the electrical sine-wave signals of different frequencies and amplitudes that drive the wavemaker. The studies involve monochromatic waves propagating in the normal direction to the model. The model consists of a water-filled flexible sack, which also contains two air-filled flexible cylindrical tubes to provide sufficient buoyancy to the system. Reflection, transmission and energy loss coefficients are presented for a variety of wave conditions and different internal pressures in the flexible model for several specific water depths. Both fully-submerged and surface-grazing systems were considered. Energy considerations allow us also to estimate the energy losses due to the processes explained in section 2.6.

4.2 Experimental Setup and Testing Conditions

A drawing of the experimental setup is presented in Figure 4.1. Two wave probes were used to measure the water surface elevation. The first probe was located at 5.27 m ahead of the breakwater model and was measuring the incident wave component initially and the composite wave after a short period. The second probe was located at 2.44 m behind the model and was measuring the transmitted wave. Continuous wave records 102.4 sec long are taken at a sampling time-rate of 0.1 sec.

The breakwater model consists of a flexible sack suspended from a flexible cylindrical buoy and hinged at the wave tank floor. A drawing with the dimensions and construction details of the deflated flexible sack model is presented in Figure 4.2. The sack is made of reinforced high-grade neoprene rubber with thickness of 0.158 cm (1/16 in) and modulus of elasticity 3675 KPa (533 psi). The rubber sheet is attached at its low edge with aluminum clamps, while its sides are also fastened with aluminum clamps. When the sack is inflated with water it takes approximately a cylindrical inverted raindrop shape. The total length of the model is slightly smaller than the width of the tank to eliminate contact between model ends and the wave tank walls. The flexible buoy consists of two narrow cylindrical tubes connected in parallel and mounted inside the sack. Each tube has 2.79 cm (1.10 in) diameter and is made of butyl rubber. The tubes are inflated with air and their length is somewhat smaller than the total length of the structure.

The flexible sack is also equipped, on one side, with two hose fittings, one at the top and another at the bottom. The bottom fitting allows the model to be filled with water through a hose from the pressure-head device. The top fitting is used to read the internal sack-pressure before each set of experiments using a piezometric tube. From the top fitting a plastic hose also connects the inner narrow tubes with a pressure-regulating system, which monitors and controls the air-pressure, increasing or decreasing the buoyancy of the structure. The total internal air-pressure of the tubes was kept at 27.6 KPa (4 psi) during all the tests. Different snapshots when the flexible sack breakwater model was suspended in the wave tank are presented in Figures 4.3, 4.4 and 4.5.

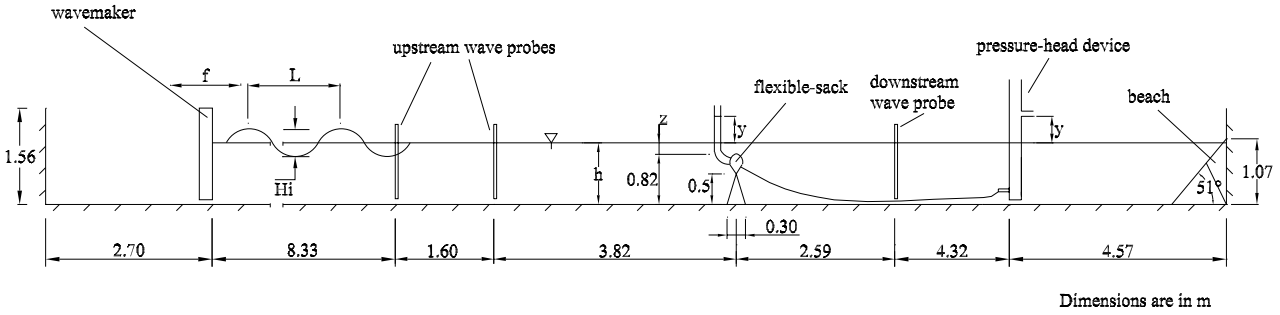

Figure 4.1: Experimental set up of the suspended flexible sack breakwater model.

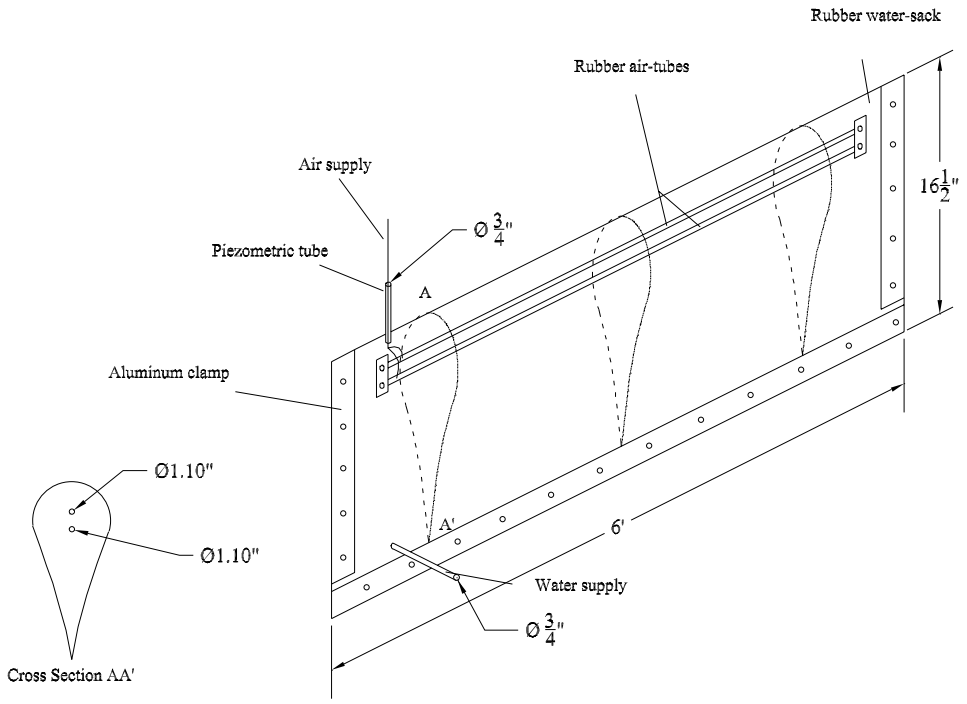

Figure 4.2: Dimensions and construction details of deflated flexible sack breakwater model.

The model is moored with four steel-nylon cables at the bottom of the wave tank, as shown in Figure 4.6. In Figure 4.6(a) we see the cables' connections to the tank floor in still water. In Figures 4.6(b) and 4.6(c) we see in sequential frames the formation of an extensive deformation for the back cables during a wave's action. The model is somewhat constrained in location but it is free to move along short circular arcs, nearly parallel to the bottom. In Figure 4.7, in Frame 1, we see the flexible sack at its equilibrium position in still water. In Frames 2 and 3 the flexible sack is oscillating back and forth while it interacts with waves.

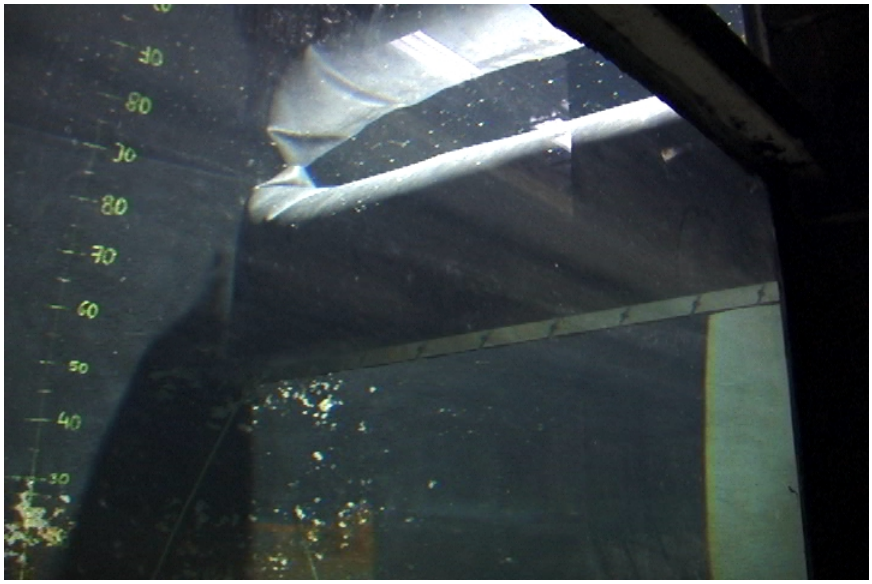

Figure 4.3: Bottom-front-view of flexible sack breakwater model.

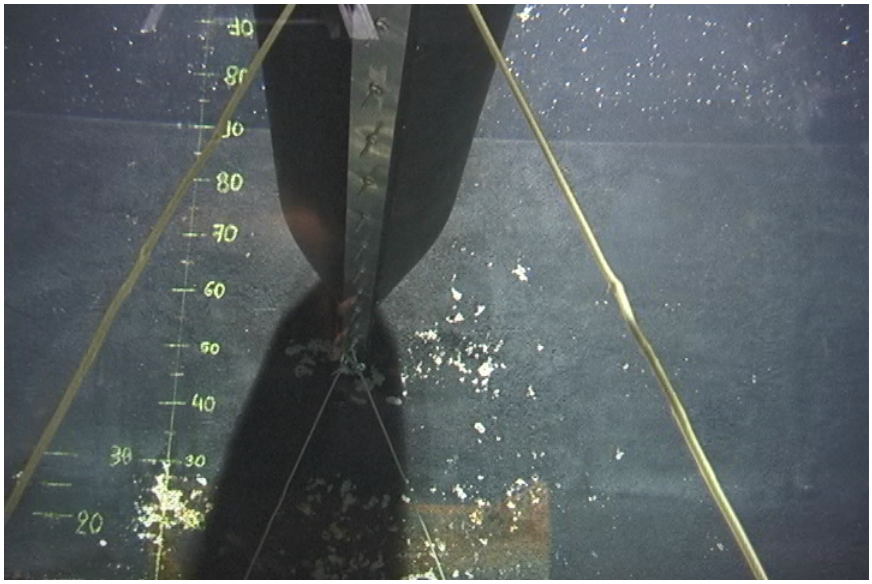

Figure 4.4: Bottom-view of flexible sack breakwater model.

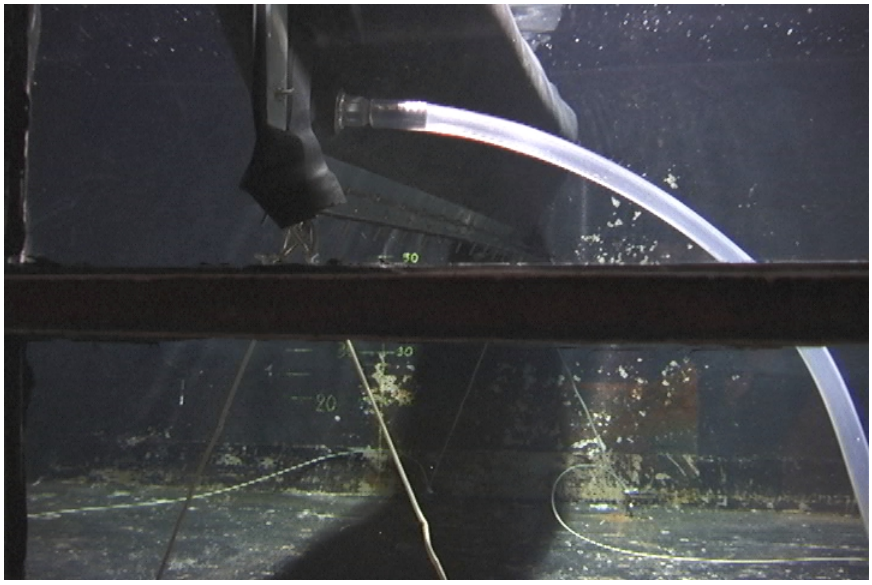

Figure 4.5: Bottom-back-view of flexible sack breakwater model.

(a) Cables' connections to the bottom of ESM wave tank at still water.

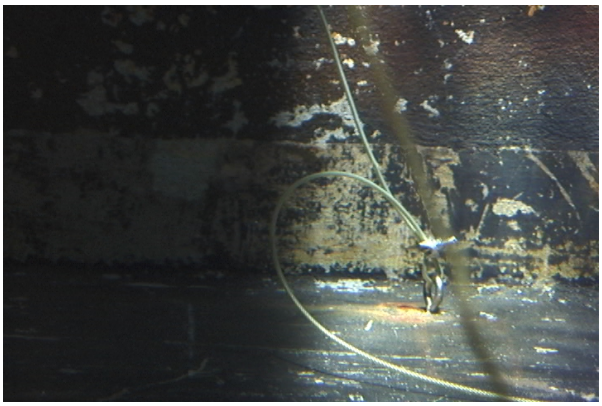

(b) Back cables deformation during wave action.

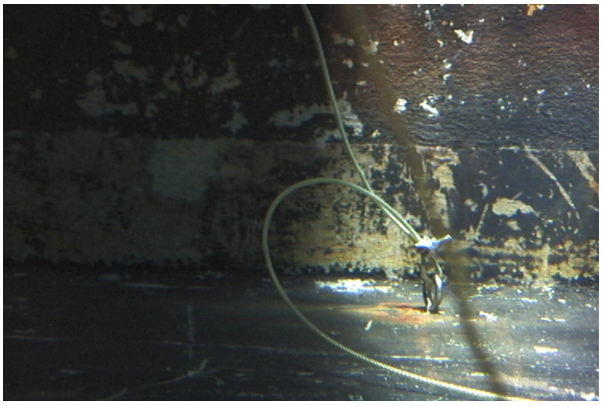

(c) Back cables extensive deformation during wave action.

Figure 4.6: Connections and deformation of flexible sack's cables.

(a) Frame 1

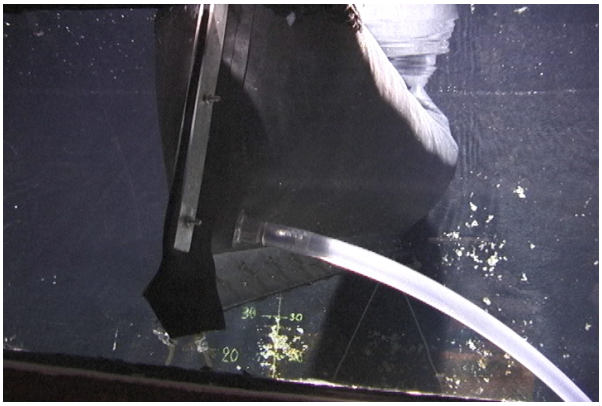

(b) Frame 2

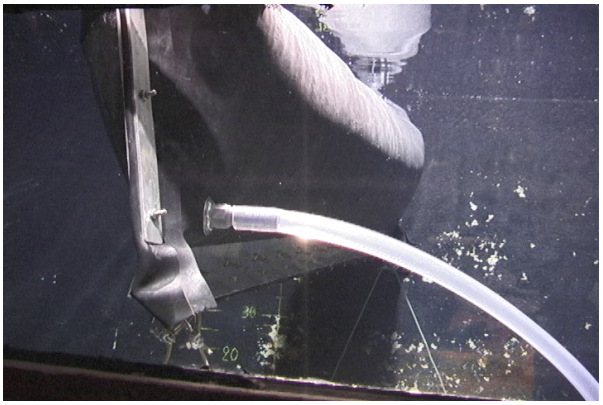

(c) Frame 3

Figure 4.7: Oscillation of flexible sack during wave action.

Tests for different wave frequencies and amplitudes, yielding different wave steepnesses, $\frac{H_i}{L}$, were conducted at water depths of 80 cm ($z/h = 0$), 90 cm ($z/h = 0.09$) and 100 cm ($z/h = 0.18$). Moreover, for the case of $z/h = 0.09$ we considered y/h ratios of 0.10 and 0.16, and for the case of $z/h = 0.18$ we considered y/h ratios of 0.04 and 0.10. All the experimental runs for the suspended flexible sack are summarized and presented in Table 4.1.

Table 4.1: Experimental runs for the suspended flexible sack breakwater model.

Flexible sack	Water depth (h), [cm]	z/h	y/h	Wavemaker driving frequency, [Hz]
	80	0	0.20	0.6, 0.7, 0.8,...,1.4
	90	0.09	0.10	0.6, 0.7, 0.8,...,1.4
		0.09	0.16	0.6, 0.7, 0.8,...,1.4
	100	0.18	0.04	0.6, 0.7, 0.8,...,1.4
		0.18	0.10	0.6, 0.7, 0.8,...,1.4

4.3 Results and Discussion

The variation of wave steepness, H_i/L, with kh for all waves, when the water depth was 80 cm ($z/h = 0$), is shown in Figure 4.8. The wave steepness, H_i/L, increases from 0.007 to 0.049 as kh increases from 1.33 to 6.31. At $kh = 3.23$ there is a local minimum of $H_i/L = 0.020$. The values of the incident height, H_i, were determined from the wavelet analysis.

Variations of reflection, transmission and energy loss coefficients with kh, for the conditions shown in Figure 4.8, are presented in Figure 4.9. The y/h ratio was 0.20. The results show that the reflection is most effective with a coefficient value near 0.50 for $kh \geq 4.64$ (maximum wave steepness, H_i/L) and less effective with a coefficient value near 0.08 for $kh \leq 1.69$ (minimum wave steepness, H_i/L). In between, C_r varies around a value of 0.25 with a slight maximum near $kh = 3.23$. The average reflection, C_r, is near 30% for the range of kh studied. As for the transmission coefficient, C_t, it is noted that it varies around a value of 0.80 with a slight dip around 0.50 near $kh = 3.23$ and $kh = 6.31$. The average transmission is 73% for the range of kh studied. As for the energy loss coefficient, C_L, the results show that it varies around a value

of 0.50 with a slight dip around 0.18 near $kh = 4.64$. The corresponding average value for the energy loss is 54%.

It can be noticed that the wave steepness $H_i/L = 0.020$ ($kh = 3.23$) at which transmission is minimum coincides with the steepness at which the energy loss is maximum and not with that of maximum reflection, $H_i/L = 0.043$ ($kh = 5.44$). This indicates that a greater proportion of wave energy is dissipated due to turbulence, rather than being reflected back. In Figure 4.10, the flexible sack grazing the surface interacts with incident waves without breaking, while in Figure 4.11, wave breaking over the flexible sack is shown.

The formation of a mode of oscillation along the longitudinal direction of the model is presented in Figure 4.12 in a sequence of frames when the flexible sack is grazing the water surface at a frequency of 1 Hz. In Frame 1 the incident wave approaches the flexible sack breakwater. In Frame 2 the flexible sack interacts with the incoming water waves, leading to a slight breaking. Frame 3 shows a following time instant, where part of the incident wave passes over the breakwater. We can also see that the right end of the flexible sack is starting to sink. In Frame 4, the right end is almost under the water and pushes the middle of the model upwards. This is more pronounced in Frame 5 where the final stage of the formation of the mode of oscillation along the longitudinal direction of the model is occurring. Frame 6 shows the wave breaking over the breakwater as a consequence of this mode of oscillation.

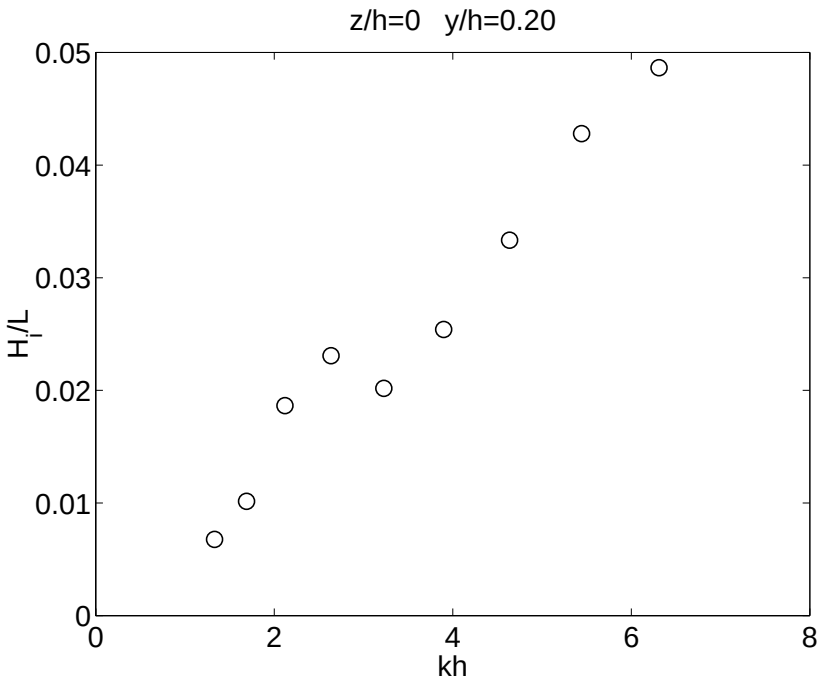

Figure 4.8: Variation of wave steepness with kh for the flexible sack. Water depth 80 cm.

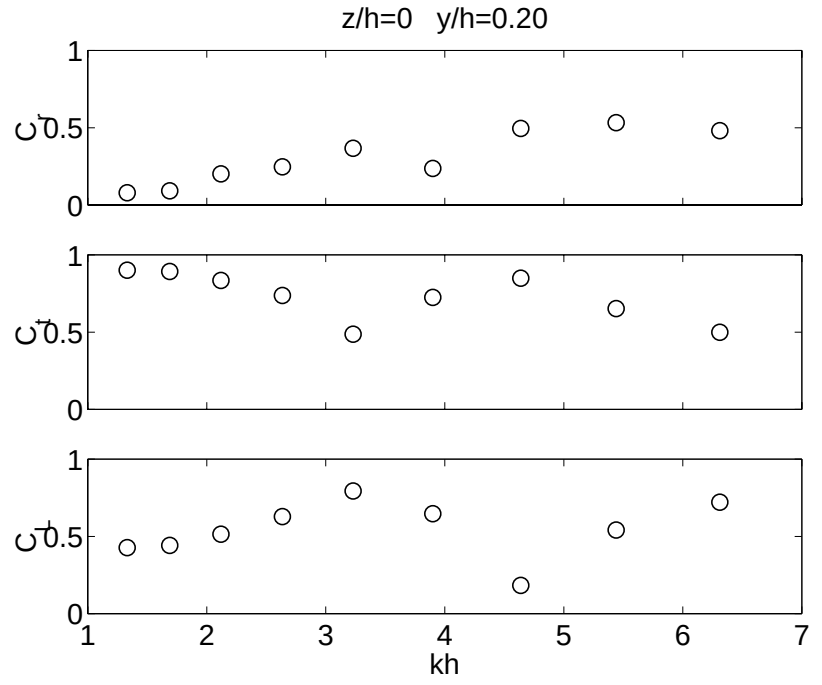

Figure 4.9: Variations of wave coefficients with kh for the flexible sack. Water depth 80 cm.

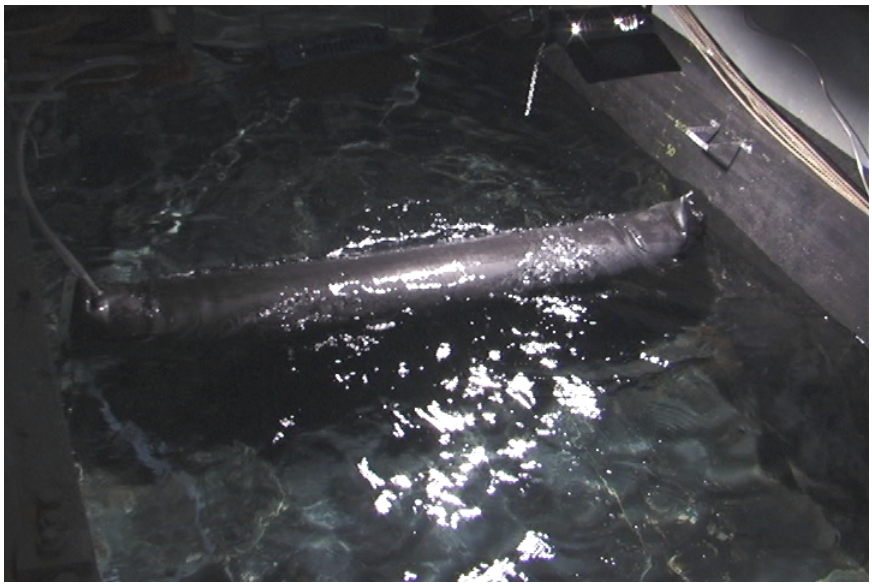

Figure 4.10: Interaction of water waves with the flexible sack grazing the surface without breaking.

Figure 4.11: Wave breaking over the flexible sack grazing the surface.

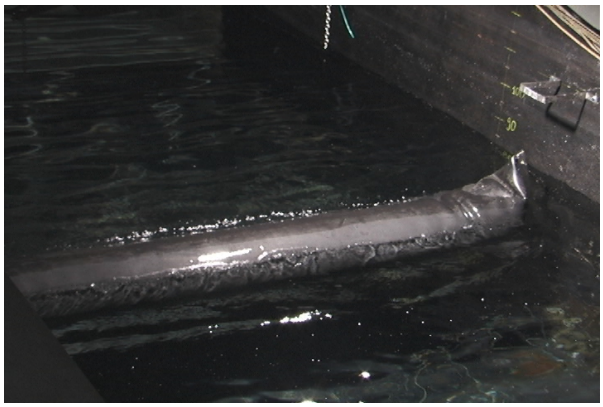

(a) Frame 1

(b) Frame 2

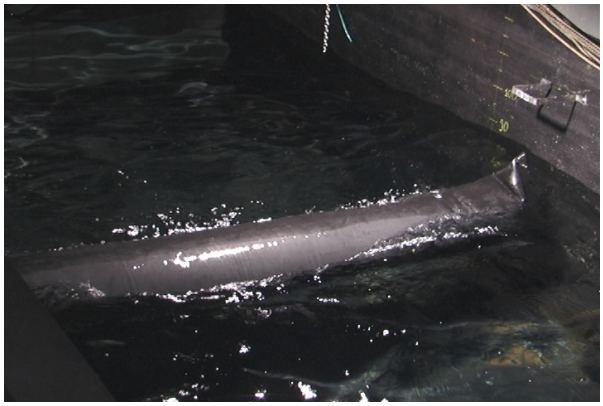

(c) Frame 3

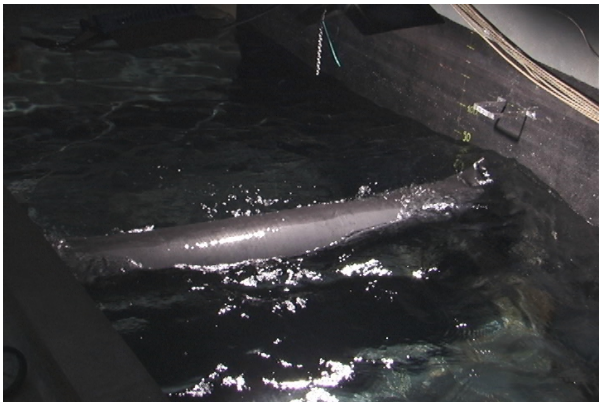

(d) Frame 4

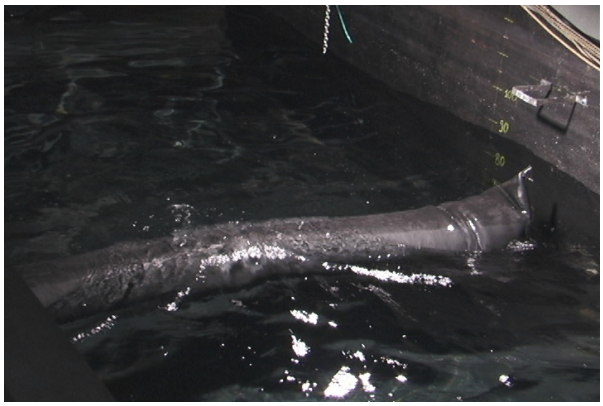

(e) Frame 5

(f) Frame 6

Figure 4.12: Oscillation along the longitudinal direction of the flexible sack grazing the surface.

The variation of wave steepness, H_i/L, with kh for all waves, when the water depth was 90 cm ($z/h = 0.09$), is shown in Figure 4.13. The wave steepness, H_i/L, increases from 0.011 to 0.042 as kh increases from 1.45 to 7.10. The values for the incident height, H_i, are determined from the wavelet analysis. It is interesting to note that H_i/L values, which are determined from independent experimental runs at each wave frequency, are very consistent. This shows the reliability of the wavelet analysis, as presented in Chapter 3 to obtain estimates for H_i.

Variations of reflection, transmission and energy loss coefficients with kh, for the conditions shown in Figure 4.13, are given in Figure 4.14. The results show that C_r varies around 0.45 for $kh \geq 2.95$ and $kh \leq 5.22$. Below and above this range the values of C_r are lower and vary near 0.15. Moreover, the values of C_r are very close to each other for the two internal-sack pressures tested, throughout the range of kh. The average values of C_r are found to be about 28% and 28% for y/h ratios of 0.10 and 0.16, respectively, for the range of kh studied. As for the transmission coefficient, C_t, the results show values above 0.70 for both sack's pressures. Again the values of C_t are very close to each other for the two internal-sack pressures. The flexible sack breakwater model has an average transmission of 83% and 83% for y/h ratios of 0.10 and 0.16, respectively, for the range of kh studied. As for the energy loss coefficient, C_L, the results show that it varies around a value of 0.50. The corresponding average values for the energy loss at this depth are 43% and 43%. It can be noticed that minimum transmission is not achieved when reflection is maximum. This result, again, emphasizes the importance of wave dissipation due to turbulence in the effectiveness of the suspended flexible sack in reducing the transmitted waves. By comparing the average values of the wave coefficients for both pressures, it can be concluded that most of the wave energy is transmitted and dissipated. The lowest portion of the wave energy is reflected back.

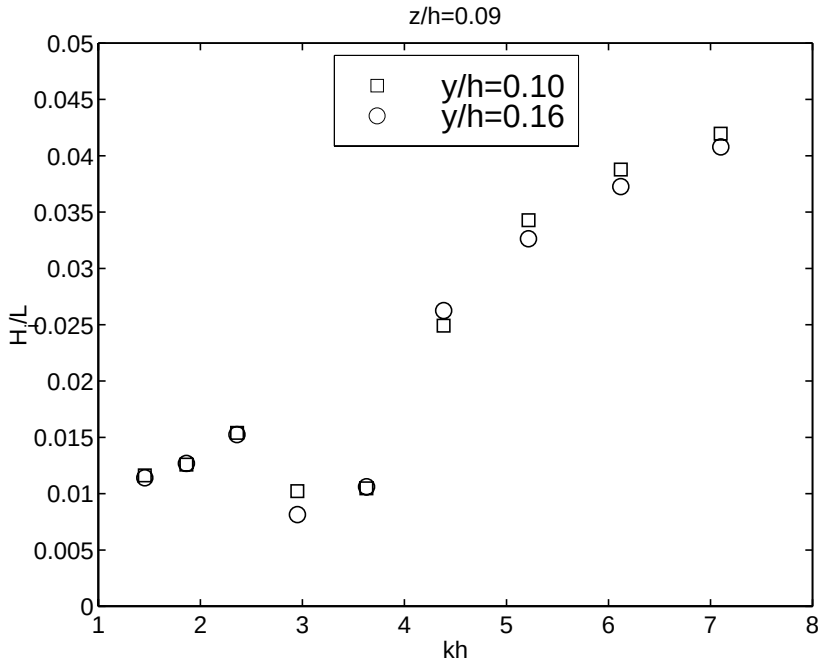

Figure 4.13: Variation of wave steepness with kh for the flexible sack. Water depth 90 cm.

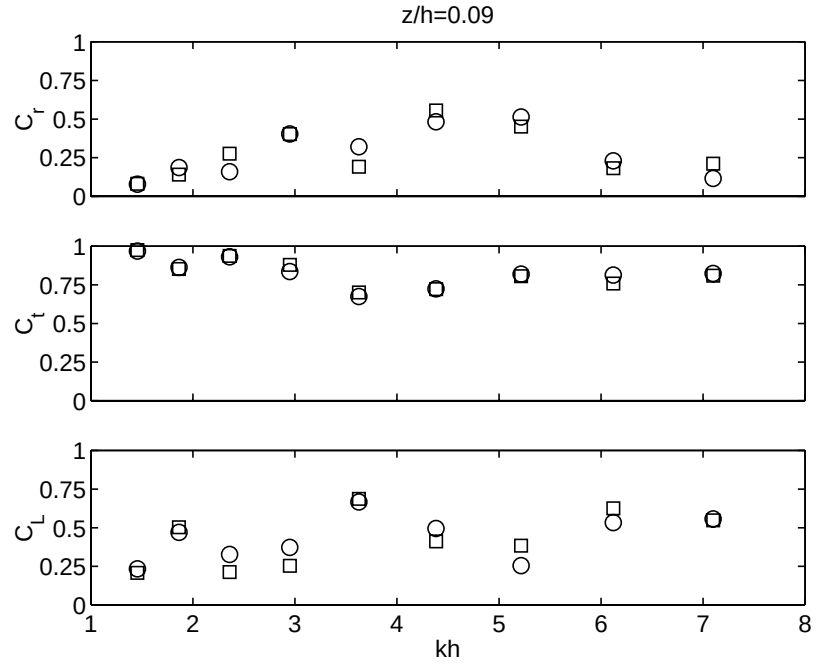

Figure 4.14: Variations of wave coefficients with kh for the flexible sack. Water depth 90 cm. For legend see Figure 4.13.

The variation of wave steepness, H_i/L, with kh for all waves, when the water depth was 100 cm ($z/h = 0.18$), is shown in Figure 4.15. The wave steepness, H_i/L, increases from 0.014 to 0.053 as kh increases from 1.58 to 7.89. The values for the incident height, H_i, are determined again from the wavelet analysis and they are consistent for the independent experimental runs involving two different internal-sack pressures.

Variations of reflection, transmission and energy loss coefficients with kh, for the conditions shown in Figure 4.15, are presented in Figure 4.16. The results show that the reflection is most effective with a coefficient value around 0.35 for $kh \geq 6.80$ (maximum wave steepness, H_i/L). For $kh \leq 5.79$ the results show C_r values below 0.30 for y/h ratios of 0.04 and 0.10. The reflection coefficient, C_r, is independent of the variations in internal-sack pressure throughout the range of kh. The average values of C_r are found to be about 22% and 21% for y/h ratios of 0.04 and 0.10, respectively, for the range of kh studied. As for the transmission coefficient, C_t, the results show values above 0.80 for all the sack's internal pressures. In that water depth, the flexible sack breakwater model has an average transmission of 89% and 88% for y/h ratios of 0.04 and 0.10, respectively, for the range of kh studied. The coefficient of energy loss, C_L, varies around a value of 0.35 with a slight dip around 0.15 near $kh = 5.79$ for $y/h = 0.04$. For $kh \leq 2.60$, C_L is independent of the variations in wave steepness for both y/h ratios, while for $kh \geq 5.79$, C_L is independent of the variations in wave steepness for y/h equal to 0.10. In between, it is found that the variation in the wave steepness does not have any significant influence on the variations of C_L for $y/h = 0.04$ whereas for $y/h = 0.10$ the value of C_L increases with wave steepness. The corresponding average values for the energy loss are 36% and 40% for y/h ratios of 0.04 and 0.10, respectively. By comparing again the average values of the wave coefficients for both pressures, it can be concluded that most of the wave energy is transmitted and dissipated. The lowest portion of the wave energy is reflected.

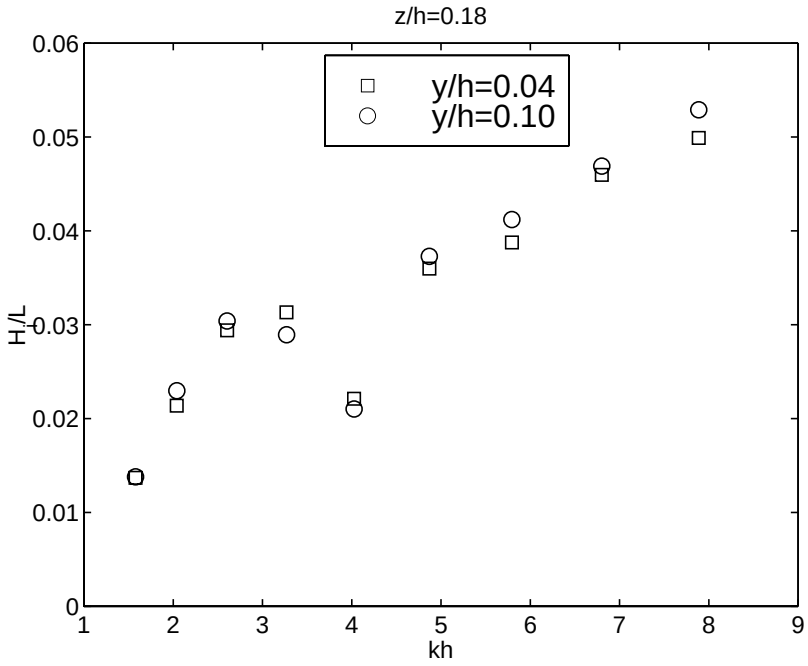

Figure 4.15: Variation of wave steepness with kh for the flexible sack. Water depth 100 cm.

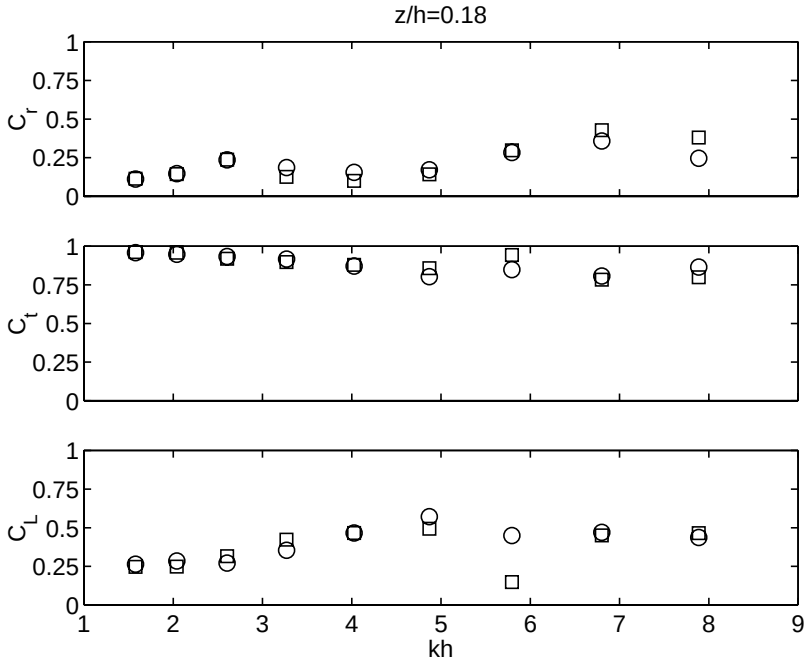

Figure 4.16: Variations of wave coefficients with kh for the flexible sack. Water depth 100 cm. For legend see Figure 4.15.

4.4 Conclusions

By comparing the average values of the wave coefficients for all internal flexible sack pressures, it can be concluded that as the submergence depth ratio decreases, the performance of the breakwater model becomes more effective. Thus, the lower submergence depth ratio, $z/h = 0$, causes higher wave reflection, lower wave transmission and higher energy loss than the higher submergence depth ratios of $z/h = 0.09$ and 0.18. However, for all submergence depth ratios examined, most of the wave energy is transmitted, some is dissipated and the lowest portion is reflected.

For submergence depth ratios, z/h, of 0 and 0.09, minimum transmission is not achieved when reflection is maximum but when energy loss is at its peak. This indicates that a greater proportion of wave energy is dissipated due to turbulence, rather than being reflected back. For submergence depth ratios, z/h, of 0.09 and 0.18, the reflection, transmission and energy loss coefficients are almost independent of the internal flexible sack's pressures, throughout the range of wave steepness studied.

Based also on the presented results, we can conclude that the variation in the wave steepness significantly influences the variations of the wave reflection and wave transmission for $z/h = 0$. As the submergence depth ratio increases, the variation in the wave steepness influences the variations of the wave reflection more and the variations of the wave transmission less. Moreover, the variation of the wave reflection with wave steepness decreases as the submergence depth ratio increases.

Chapter 5

Wave Coefficients Over Bottom-Mounted Breakwaters

5.1 Introduction

In this chapter we present and discuss the reflection, transmission and energy loss coefficients obtained for the bottom-mounted breakwater models. All the experiments were carried out in the Engineering Science and Mechanics (ESM) wave tank of Virginia Tech. The studies involve monochromatic waves propagating in the normal direction to the models. A 275 Wavetek digital function generator was used to generate the electrical sine-wave signals of different frequencies and amplitudes, and to drive the wavemaker. Two wave probes were used to measure the water surface elevation. The first wave probe was located at 5.27 m ahead of the model and was measuring the incident wave component initially and the composite wave after a time period. The second wave probe was located at 2.44 m behind the model and was measuring the transmitted wave. As in the work for the suspended model, wavelet analysis is used to separate the two parts of a composite record, which are then used to determine the reflection coefficient. The transmission coefficient is measured using the record of the second wave probe. For all the experimental runs, continuous wave records of 102.4 sec long were taken at a sampling time-rate of 0.1 sec.

The potential effectiveness of different model geometries as breakwaters is investigated. First,

we compare the performance of a rectangular but flexible structure filled with water to a rectangular rigid model. An example presenting typical results of all wave coefficients for one set of measurements is given for the rectangular rigid model. The analysis described in this example is performed on all records of bottom-mounted models. Second, a hemi-cylindrical flexible structure filled with water is compared with a hemi-cylindrical rigid structure. Finally, reflection and transmission characteristics of regular surface waves over two hemi-cylindrical, flexible-composite breakwater models are also presented. The first model is reinforced with composite strips along its longitudinal direction and is filled with water. The second model is reinforced with composite strips along its longitudinal as well as its hoop direction and is also filled with water. In both cases the results are compared with the results obtained for the hemi-cylindrical rigid model.

Reflection, transmission and energy loss coefficients are presented for a variety of wave conditions for the rigid models as well as for different internal pressures in the flexible models for several specific water depths. Energy considerations allow us also to estimate the energy losses due to the processes explained in section 2.6. The ultimate goal of the analysis is to optimize the bottom-mounted breakwater's design for minimum wave transmission.

5.2 Wave Coefficients Over Rectangular Flexible and Rigid Breakwaters

5.2.1 Experimental Setup and Testing Conditions

A drawing of the experimental setup is presented in Figure 5.1. Two breakwater models were used in these experiments. The first model is a solid prism with dimensions of 1.83m x 0.30m x 0.17m (6ft x 1ft x 6.75in). The prism is made of polyvinyl-chloride (PVC) and is mounted on an aluminum plate of 1.83m x 0.30m (6ft x 1ft). A drawing with the dimensions of the rectangular rigid breakwater model is presented in Figure 5.2. Photos of the rectangular rigid breakwater model are presented in Figures 5.3, 5.4. The second model consists of a flexible membrane fastened on an aluminum plate with the same dimensions as the rigid model. The

membrane is made of high-grade neoprene rubber of medium hardness with a thickness of 0.158 cm (1/16 in) and modulus of elasticity 3675 KPa (533 psi). The rubber sheet is attached to the plate sides at the bottom with aluminum clamps. A drawing with the dimensions of the rectangular flexible breakwater model is presented in Figure 5.5. The rubber sheet is reinforced with a rectangular PVC sheet, as shown in Figures 5.6 and 5.7. The idea is to preserve the top side of the model as flat as possible in order to induce flow separation and consequently turbulent dissipation. The sheet has dimensions of 1.22m x 0.30m x 0.63cm (4ft x 1ft x 1/4in) and is positioned inside the model. The ends of the flexible model are capped with rectangular sheets of plexiglass with thickness of 1.27 cm (1/2 in), where the rubber sheet is fastened tight using two aluminum belts. This design assumes a rectangular shape with dimensions close to those of the rigid prism when the flexible model is filled with water.

The rubber sheet is also equipped with two hose fittings. The first, which is close to one side at the bottom of the flexible model, allowed the model to be filled with water from the pressure-head device, which also recovered any water losses during the experiments. The second fitting is on the top of the other side of the model and allowed us to read the internal pressure before each set of experiments using a piezometric tube. Both rigid and flexible structures were anchored rigidly at the tank floor using steel-nylon cables. Four hooks and four stainless steel pad-eyes, one at each corner on the aluminum plate, were also used for that reason. Thus, both models did not float or move when subjected to wave action. We also made sure that there was no contact between the models' ends and the tank walls during the experiments. Photos of the rectangular flexible breakwater model are presented in Figures 5.8 and 5.9.

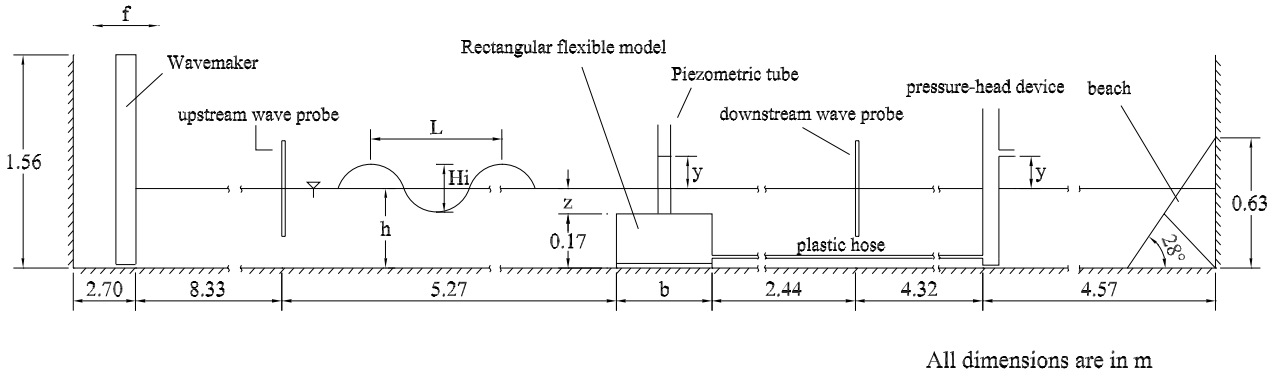

Figure 5.1: Experimental setup of the rectangular flexible breakwater model.

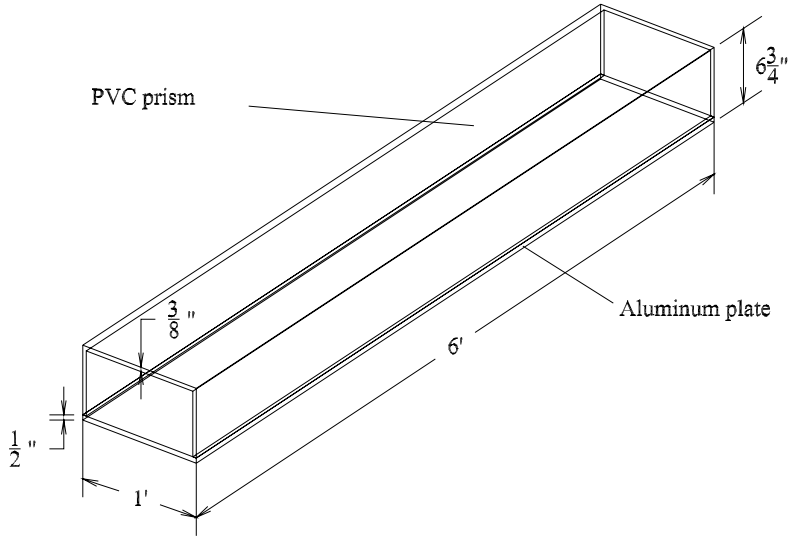

Figure 5.2: Dimensions of the rectangular rigid breakwater model.

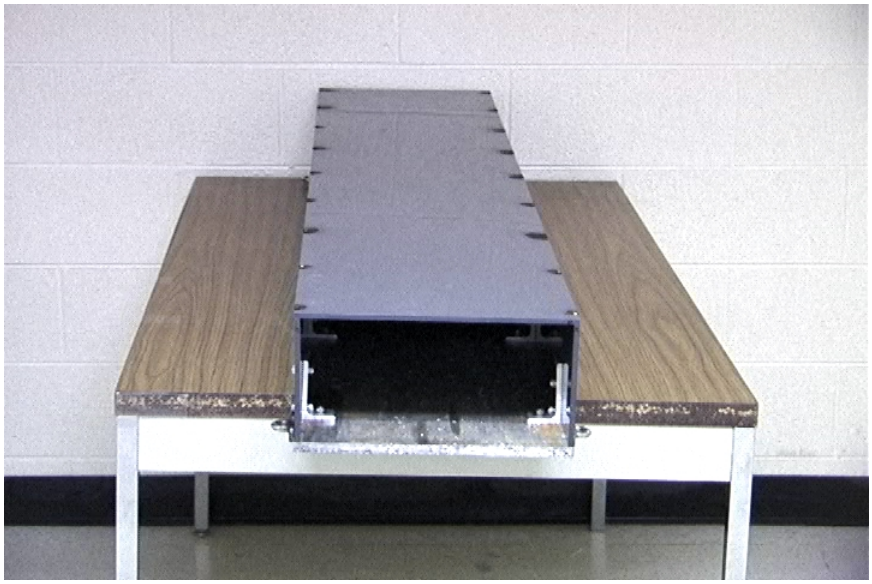

Figure 5.3: Front-view of the rectangular rigid breakwater model.

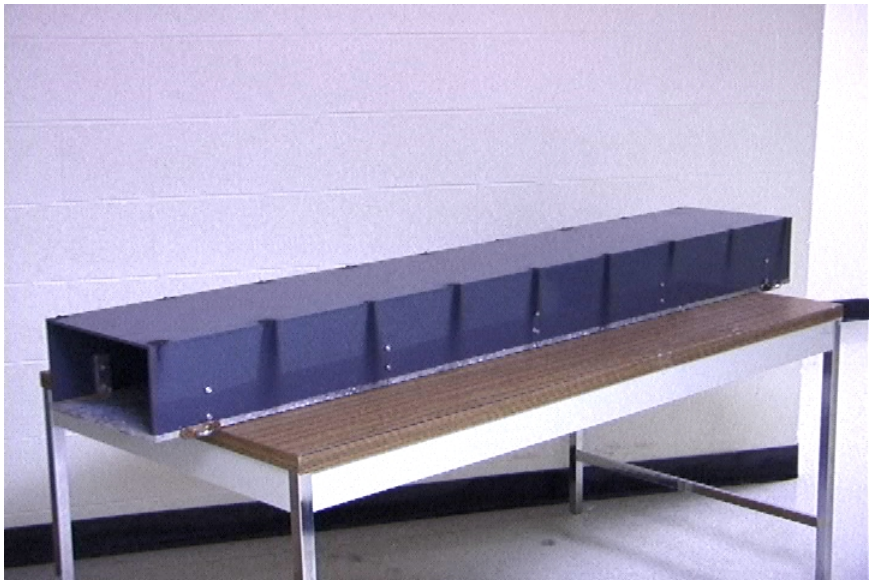

Figure 5.4: Side-view of the rectangular rigid breakwater model.

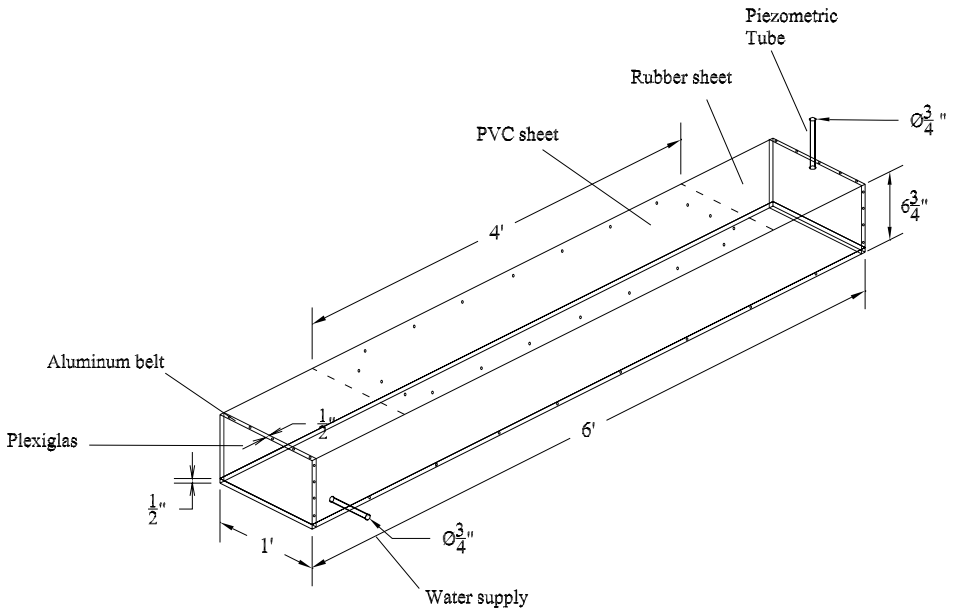

Figure 5.5: Dimensions of the rectangular flexible breakwater model.

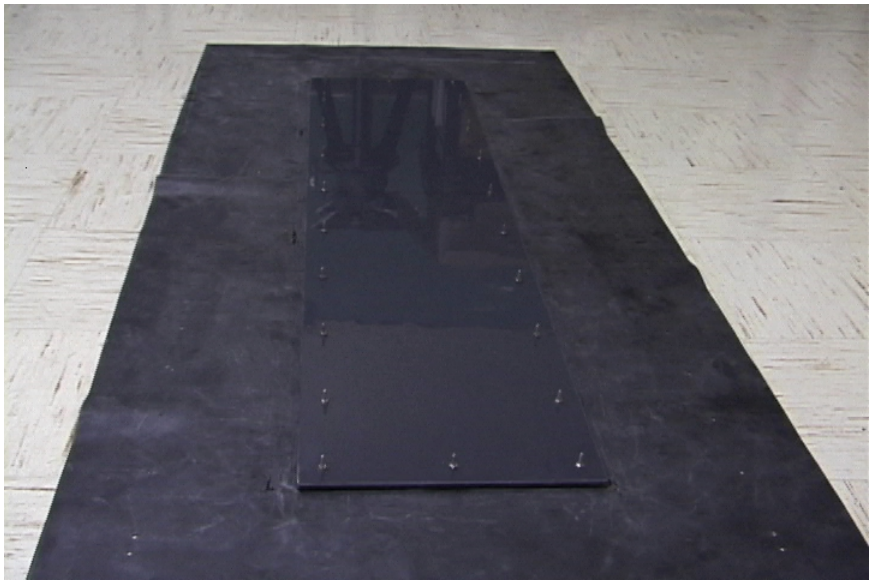

Figure 5.6: Front-view of the PVC sheet attached to the rubber sheet.

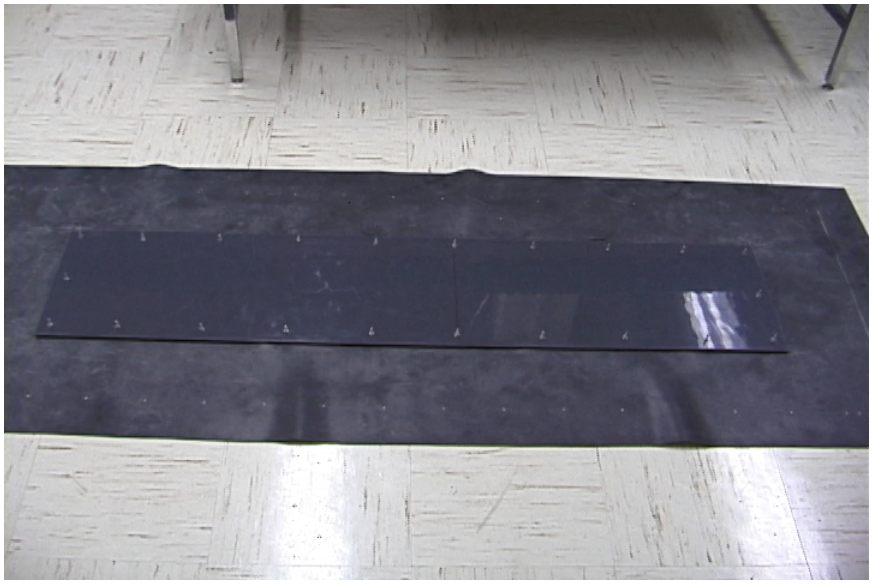

Figure 5.7: Side-view of the PVC sheet attached to the rubber sheet.

Figure 5.8: Front-view of the rectangular flexible breakwater model.

Figure 5.9: Side-view of the rectangular flexible breakwater model.

Table 5.1: Experimental runs for the rigid and flexible rectangular breakwater models.

	Water depth (h), [cm]	z/h	y/h	Wavemaker driving frequency, [Hz]
Rigid model	22.5	0.24		0.6, 0.7, 0.8,...,1.4
Rigid model	27.5	0.38		0.6, 0.7, 0.8,...,1.4
Flexible model	22.5	0.24	0.007	0.6, 0.7, 0.8,...,1.4
		0.24	0.141	0.6, 0.7, 0.8,...,1.4
		0.24	0.282	0.6, 0.7, 0.8,...,1.4
Flexible model	27.5	0.38	0.007	0.6, 0.7, 0.8,...,1.4
		0.38	0.141	0.6, 0.7, 0.8,...,1.4
		0.38	0.282	0.6, 0.7, 0.8,...,1.4

Tests for different wave frequencies and amplitudes, yielding different wave steepnesses, $\frac{H_i}{L}$, were conducted at water depths of 22.5 cm ($z/h = 0.24$) and 27.5 cm ($z/h = 0.38$) for both models. Moreover, for the flexible model, we considered y/h ratios of 0.007, 0.141 and 0.282 at each water depth. All the experimental runs for both rectangular breakwater models are summarized and presented in Table 5.1.

5.2.2 Results and Discussion

Typical results for one set of measurements

Typical profiles of regular waves recorded ahead of and behind the rectangular rigid breakwater model are shown in Figure 5.10. The wavemaker frequency was set at 0.6 Hz. The first record, shown in Figure 5.10-a, consists initially of the incident wave component, $\eta_i(x,t)$. After an initial period, it contains the sum of the incident and reflected wave components (composite wave), $\eta(x,t)$. The second record, shown in Figure 5.10-b, contains the transmitted wave, $\eta_t(x,t)$. An analysis similar to the one presented in Section 3.5.1 is conducted for the first record. The magnitude and the unwrapped phase of the wavelet coefficient at the wave component with $f_\mu = 0.6Hz$ are presented in Figures 5.11-a and 5.11-b, respectively. Estimates for the amplitude, α_i, and the total phase, $-kx + \phi_i$, of the incident wave component are obtained,

computing averages for the magnitude and phase of the wavelet coefficient between $t = 5.5sec$ and $t = 9.3sec$. The first time, $t = 5.5sec$, corresponds to a well-defined incident wave peak approaching the first probe. The second time, $t = 9.3sec$, corresponds to that peak arriving at the breakwater. Based on these averages, we estimate α_i to be 1.21 cm and $-kx + \phi_i$ to be 4.905 rad. In Figure 5.12, we compare the estimated incident wave component (dashed line), obtained with these values for α_i and $-kx + \phi_i$, and the real part (solid line) of the wavelet coefficient at $f_\mu = 0.6Hz$ of the record shown in Fig. 5.10-a. Note the good match over the time period between 5 and 10 seconds. This shows that the estimated incident wave component compares very well with the wave component of the measured signal over this part of the record which consists of the incident component.

The reflected wave component is determined by subtracting vectorially the incident wave component, as determined above, from the composite wave. Estimates for the amplitude, α_r and the total phase, $kx + \phi_r$, of the reflected wave component are obtained by computing averages for the amplitude and phase of the reflected component obtained from the vectorial subtraction between $t = 13sec$ and $t = 24.8sec$. The first time, $t = 13sec$, corresponds to a composite wave peak approaching the first probe, and the second time, $t = 24.8sec$, corresponds roughly to a re-reflected wave peak from the wavemaker approaching it again. Based on these averages, we calculate α_r to be 0.54 cm and $-kx + \phi_r$ to be 2.06 rad.

In Figure 5.13, the magnitude of the wavelet coefficient, $|W|_t$, at the wave component at $f_\mu = 0.6Hz$ in the transmitted signal, shown in Fig. 5.10-b, is presented. An estimate for the amplitude, α_t, of the transmitted wave is obtained, computing an average value for the magnitude of the wavelet coefficient between $t = 11.2sec$ and $t = 18.1sec$. The first time, $t = 11.2sec$, corresponds to a well-defined wave peak approaching the probe behind the breakwater model, and the second time, $t = 18.1sec$, corresponds to that peak arriving at the wave tank end. Based on this average, we calculate α_t to be 0.80 cm. With the above estimates for α_i, α_r and α_t, the reflection coefficient, C_r, is calculated to be 0.44 and the transmission coefficient, C_t, to be 0.66. The energy loss coefficient, C_L, via (1.1), is found to be about 0.61.

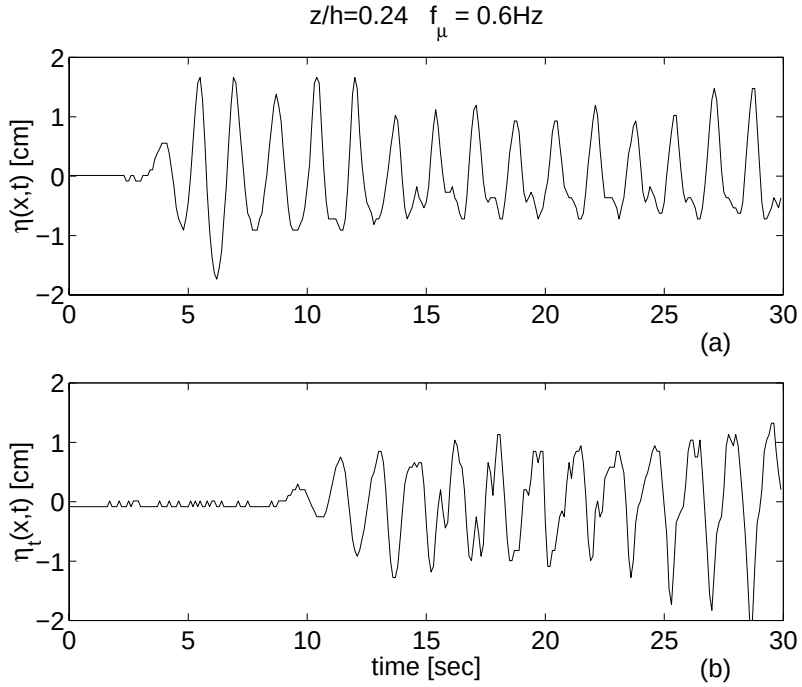

Figure 5.10: Typical regular wave profiles at two locations: (a) ahead of and (b) behind the rectangular rigid breakwater model.

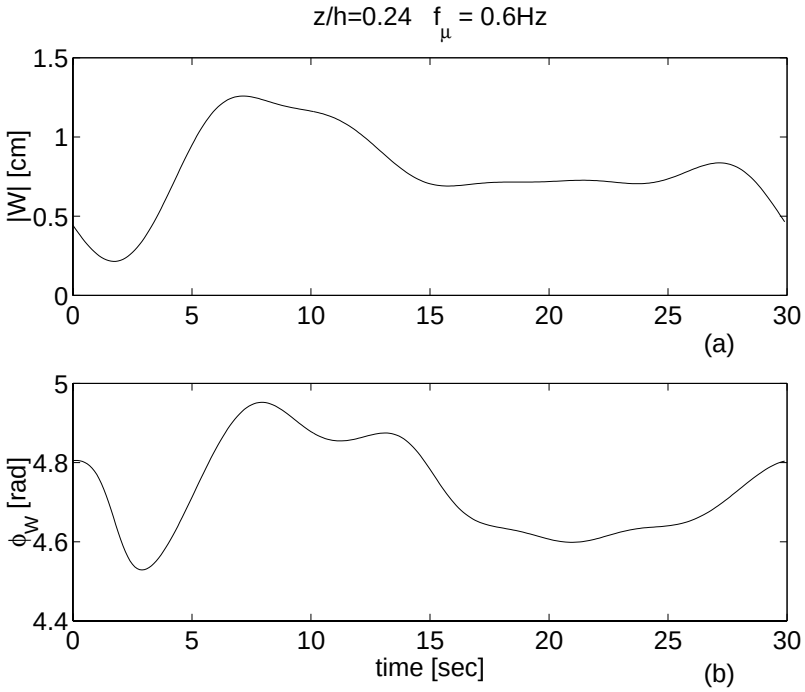

Figure 5.11: (a) Magnitude and (b) phase of the wavelet coefficient at the frequency of the fundamental wave component in the record shown in Fig. 5.10-a.

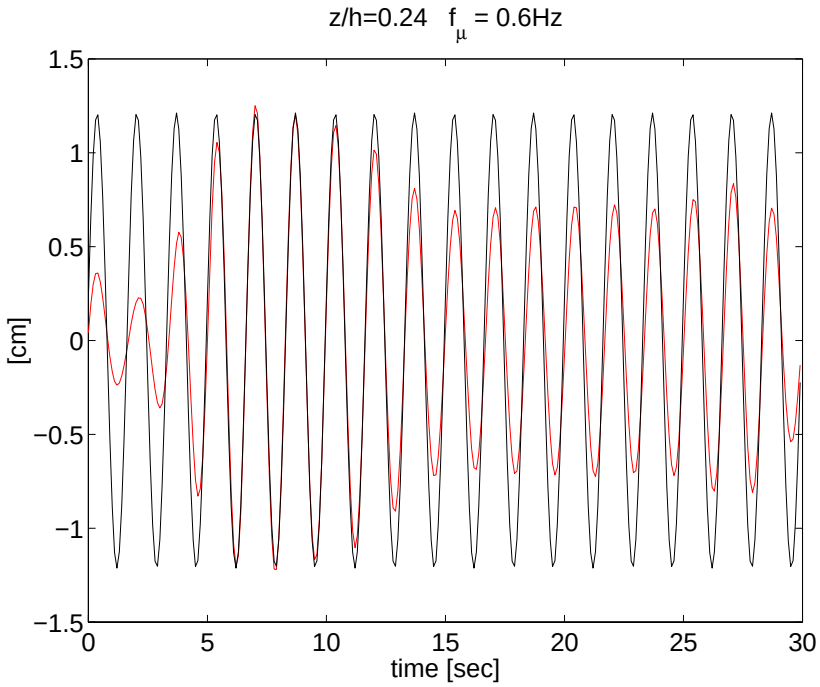

Figure 5.12: Real part of the estimated incident wave component (solid line) and real part (dashed line) of the wavelet coefficient at the frequency of the fundamental wave component.

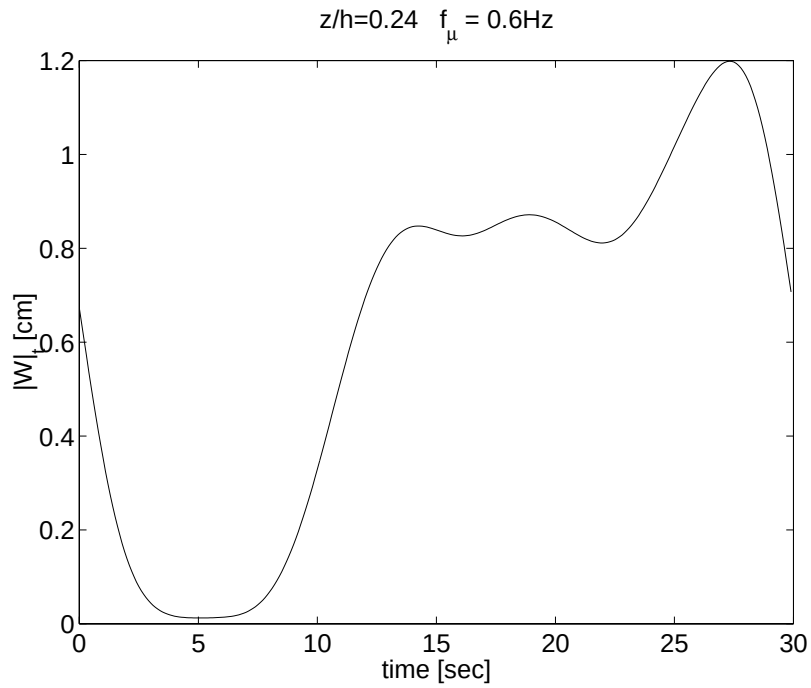

Figure 5.13: Magnitude of the wavelet coefficient at the frequency of the fundamental wave component in the record shown in Figure 5.10-b.

Reflection and Transmission Coefficients

The analysis described in the previous section was performed on all records for both rigid and flexible breakwater models, under different internal pressures in the flexible breakwater, wave frequencies and water depths. In this section, we compare the effectiveness of the rigid and flexible rectangular breakwaters and present the results in terms of the parameters presented in section 2.8. The variation of wave steepness, H_i/L, with kh for all waves, when the water depth is 22.5 cm ($z/h = 0.24$), is shown in Figure 5.14. The wave steepness, H_i/L, increases from 0.010 to 0.035 as kh increases from 0.60 to 1.86. The values for the incident height, H_i, were determined from the wavelet analysis. It is interesting to note that H_i/L values, which are determined from independent experimental runs, are extremely consistent with each other except for $kh = 0.84$ and 0.98 were small differences are noted. This shows the reliability of the wavelet analysis to obtain estimates for H_i.

Variations of reflection, transmission and energy loss coefficients with kh, for the conditions shown in Figure 5.14, are given in Figure 5.15. The results show that the reflection is most effective with a coefficient value of 0.55 near kh values of 0.60 (minimum wave steepness, H_i/L) and 1.86 (maximum wave steepness, H_i/L). In between, C_r is smaller, with a minimum of 0.05 near $kh = 0.98$ for the flexible model with y/h ratios of 0.141 and 0.282. As for the difference in the reflection characteristics of the rigid and flexible breakwaters, it is found that the average reflection for the rigid model is about 38% for the range of kh considered here. For the flexible model, C_r is near 32%, 33% and 36% for y/h ratios of 0.007, 0.141 and 0.282, respectively. These results indicate that the reflection coefficient increases with an increase in the stiffness of the model. As for the transmission coefficient, C_t, it is noted that it varies around a value of 0.5 with a slight dip near $kh = 0.98$. The rigid model has an average transmission of about 64%, while the flexible model has an average transmission of 35%, 53% and 52% for y/h ratios of 0.007, 0.141 and 0.282, respectively, for the range of kh studied. These results show that C_t decreases with decreasing stiffness of the breakwater.

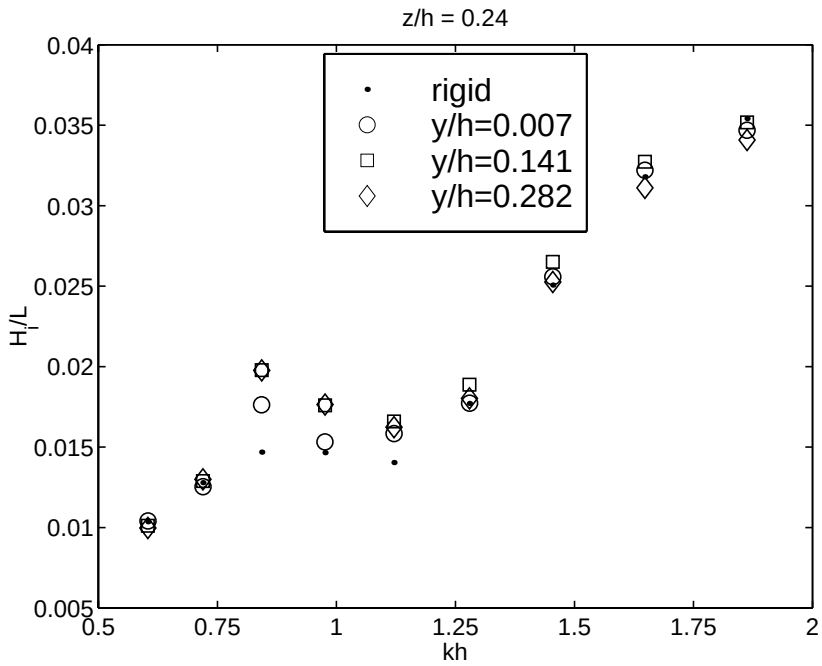

Figure 5.14: Variation of wave steepness with kh for the rectangular rigid and flexible models. Water depth 22.5 cm.

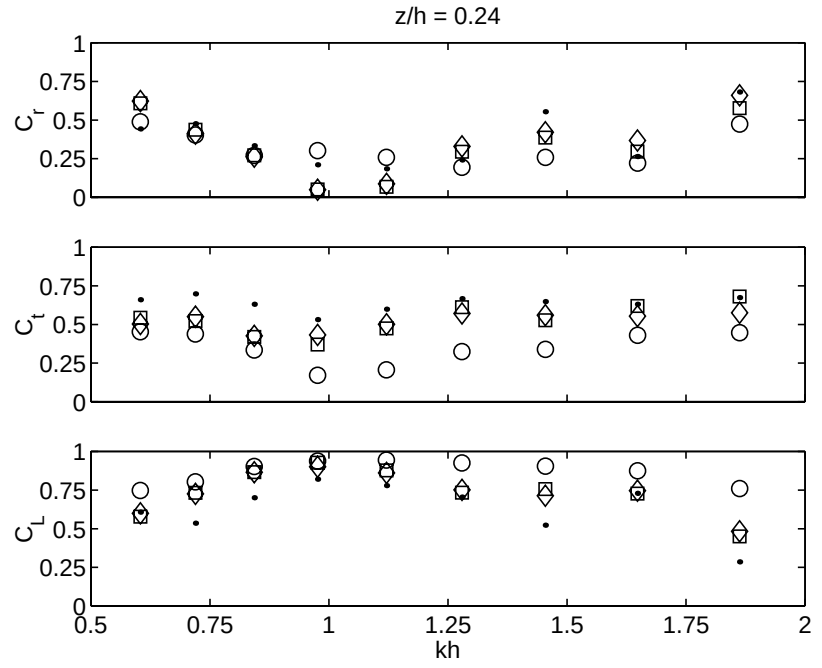

Figure 5.15: Variations of wave coefficients with kh for the rectangular rigid and flexible models. Water depth 22.5 cm. For legend see Figure 5.14.

As for the coefficient of energy loss, C_L, the results show that it increases for $kh \leq 0.84$ and decreases for $kh \geq 1.28$. In between, C_L is almost independent of the variations in wave steepness. It should also be noted that the energy loss tends to increase with decrease in stiffness. The corresponding average values for the rigid and flexible breakwaters with y/h ratios of 0.007, 0.141 and 0.282 are 63%, 87%, 74% and 74%, respectively. This shows that the energy dissipation due to the processes explained in section 2.6 is highest for the flexible model with $y/h = 0.007$. It is important also to note that $kh = 0.98$, at which energy loss is maximum, about 0.90, coincides with kh at which the transmission is minimum for both models. Moreover, at the same kh value the reflection is almost minimum, indicating that most of the wave energy is dissipated, rather than being reflected. This result emphasizes the significance of the wave dissipation over and near the model in reducing the transmitted waves.

The variation of wave steepness, H_i/L, with kh for all waves, for the rigid and flexible rectangular models, when the water depth is 27.5 cm ($z/h = 0.38$), is shown in Figure 5.16. The wave steepness, H_i/L, increases from 0.015 to 0.060 as kh increases from 0.68 to 2.22. The waves considered here are thus steeper than those in a water depth of 22.5 cm. Again, the H_i/L values for the same kh are very close together, indicating repeatable estimates for the incident wave height, H_i, using the wavelet analysis.

Variations of reflection coefficient, transmission coefficient and energy loss coefficient with kh for $z/h = 0.38$, for the conditions shown in Figure 5.16, are presented in Figure 5.17. The results show that C_r varies near 0.5 for $kh \leq 0.95$ and $kh \geq 1.95$. In between, the values of C_r are lower, with a minimum near 0.2 at $kh = 1.48$. Moreover, the reflection coefficient values are very close for all models for $kh \leq 1.11$, indicating no significant influence from the stiffness. For $kh \geq 1.29$, the reflection by the rigid model is found to be significantly higher compared to reflection by the flexible ones. As for the transmission coefficient, C_t, the results show values above 0.45 for all models. The results also show that C_t tends to increase with increase in stiffness in that the rigid model transmits higher wave energy than the flexible model. The energy dissipation is maximum for the flexible model with $y/h = 0.007$ and minimum for the rigid model throughout the range of kh. The results also show that the increase in the wave steepness does not have any influence on the variations of C_L for the rigid model when $kh \geq 1.11$ and $kh \leq 1.70$.

For the rigid model, the average value of C_r is found to be about 40% and these of C_t and C_L are about 69% and 57%, respectively, for the range of kh studied. For the flexible model with $y/h = 0.007$, the average value of C_r is found to be about 29% and these of C_t and C_L are about 51% and 79%, respectively. Although the rigid model reflects more wave energy, the flexible model is a more effective breakwater since the transmitted waves are smaller. This is most likely because the flexible model has the ability of oscillating in different modes and possibly dissipating the incoming waves. For the flexible model with $y/h = 0.141$ and 0.282, the average values are 29% and 33% for the wave reflection, 60% and 61% for the wave transmission and 72% and 70% for the energy loss, respectively.

In order to determine the effect of model width, variations of all three coefficients are discussed at constant submergence depth ratio, z/h, substituting the kh parameter with the model width to wave length ratio, b/L. The model width for both breakwaters was kept constant at 0.30 m and the incident wave length, L, was varied from 0.75 to 2.3 m for the case of $z/h = 0.24$ and from 0.77 to 2.5m for the case of $z/h = 0.38$. For the case of $z/h = 0.24$, values of b/L were varied between 0.130 and 0.401. The optimum b/L ratio for both models is between 0.210 and 0.242, where the wave transmission is minimum and the energy loss is maximum, being most marked for the flexible model with $y/h = 0.007$. For the case of $z/h = 0.38$, the value of b/L was varied between 0.119 and 0.392. The optimum b/L ratio for this case is between 0.344 and 0.392, where the transmission varies around 0.5 and the wave reflection (especially for the rigid model) and energy loss (especially for the flexible model with $y/h = 0.007$) are high.

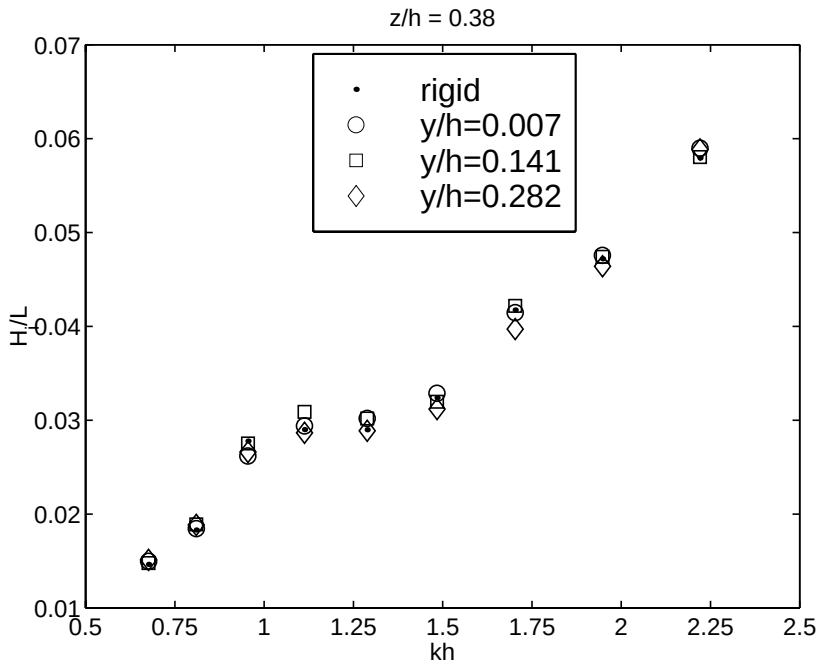

Figure 5.16: Variation of wave steepness with kh for the rectangular rigid and flexible models. Water depth 27.5 cm.

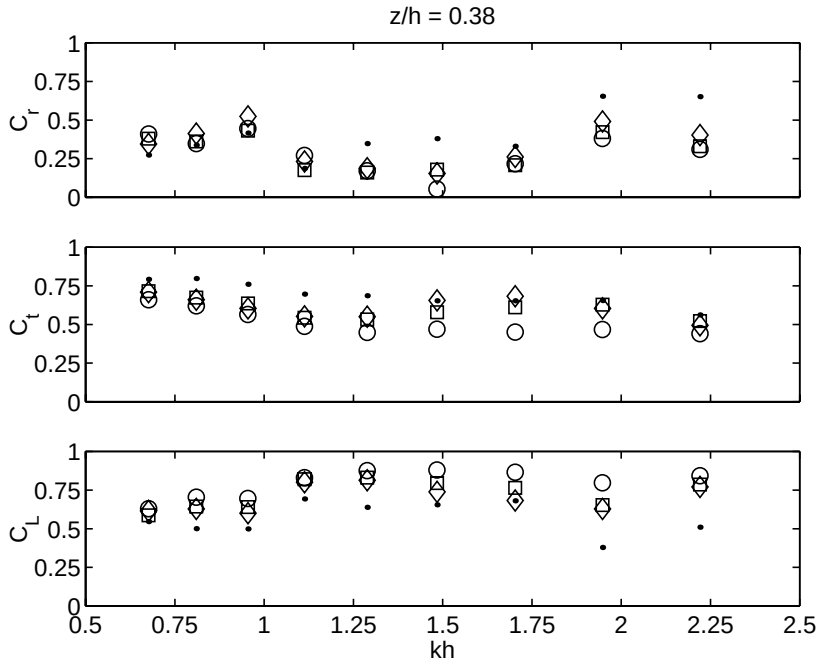

Figure 5.17: Variations of wave coefficients with kh for the rectangular rigid and flexible models. Water depth 27.5 cm. For legend see Figure 5.16.

5.2.3 Conclusions

The reflection and transmission characteristics of regular waves and the energy dissipation by rigid and flexible rectangular breakwater models, which are mounted to the bottom of a wave tank, are investigated experimentally. Results are discussed for different depths of submergence of the models, different internal pressures in the case of the flexible breakwater and for a wide range of wave steepness. By comparing the average values of the wave coefficients for both models and all internal flexible models' pressures, it can be concluded that the lower submergence depth ratio, 0.24, causes higher wave reflection, lower wave transmission and higher energy loss than the high submergence depth ratio of 0.38.

The results also show that, in general, the rigid model has a higher reflection coefficient than the flexible model. On the other hand, the flexible model has a much higher energy loss coefficient. This is most likely because the flexible model has the ability of oscillating in different modes and possibly dissipating the incoming waves. In the range of internal pressures considered here, the energy loss coefficient is higher at the lower pressures. The variation in the wave steepness, H_i/L, influences most of the variations of the wave reflection for both models and both submergence depth ratios. The results also provide optimal breakwater widths for reflection, transmission and energy loss coefficients for waves with different wave lengths.

5.3 Wave Coefficients Over Hemi-Cylindrical Flexible and Rigid Breakwaters

5.3.1 Experimental Setup and Testing Conditions

A drawing of the experimental setup is presented in Figure 5.18. Two breakwater models were used in these experiments. The first model is a hemi-cylindrical rigid tube, which is 1.83m (6 ft) long with 15.24 cm (6 in) diameter. The tube is made of polyvinyl-chloride (PVC). It is mounted on an aluminum plate 1.83m (6 ft) long and 0.30m (1 ft) wide. A drawing with the dimensions of the hemi-cylindrical rigid breakwater model is presented in Figure 5.19. Photos of the hemi-cylindrical rigid breakwater model are presented in Figures 5.20, 5.21. The second model consists of a flexible membrane mounted and fastened also on an aluminum plate with the same dimensions as the rigid model. The membrane is made of high-grade neoprene rubber of medium hardness with a thickness of 0.158 cm (1/16 in) and modulus of elasticity 3675 KPa (533 psi). The rubber sheet is attached to the plate sides at the bottom with aluminum clamps. The ends of the model are capped with hemi-cylindrical sheets of plexiglass of 1.27 cm (1/2 in) thickness, where the rubber sheet is fastened tight with two aluminum belts. This design assumes a hemi-cylindrical shape with dimensions close to those of the rigid model when the flexible model is filled with water. The flexible model, used in these experiments, was similar to the design employed by Dewi et al, [9]. A drawing with the dimensions of the hemi-cylindrical flexible breakwater model is presented in Figure 5.22.

The rubber sheet is also equipped with two hose fittings. The first, which is closed to one side at the bottom of the model, allowed the model to be filled with water from the pressure-head device, which also recovered any water losses during the experiment. The second fitting is on the top of the other side of the model and allowed us to read the internal pressure before each set of experiments using a piezometric tube. Photos of the hemi-cylindrical flexible breakwater model are presented in Figures 5.23 and 5.24.

Both rigid and flexible structures were anchored rigidly at the tank floor using steel-nylon cables, as shown in Figure 5.25 for the rigid model. Four hooks and four stainless steel pad-eyes one at each corner on the aluminum plate were also used for that reason. Thus, both models

did not float or move when subjected to wave action. We also made sure that there was no contact between the models' ends and the wave tank walls during the experiments.

Tests for different wave frequencies and amplitudes, yielding different wave steepnesses, $\frac{H_i}{L}$, were conducted at water depths of 22.5 cm ($z/h = 0.27$) and 27.5 cm ($z/h = 0.40$) for both models. Moreover, for the flexible model, we considered y/h ratios of 0.007, 0.141 and 0.282 at each water depth. All the experimental runs for both hemi-cylindrical breakwater models are summarized and presented in Table 5.2.

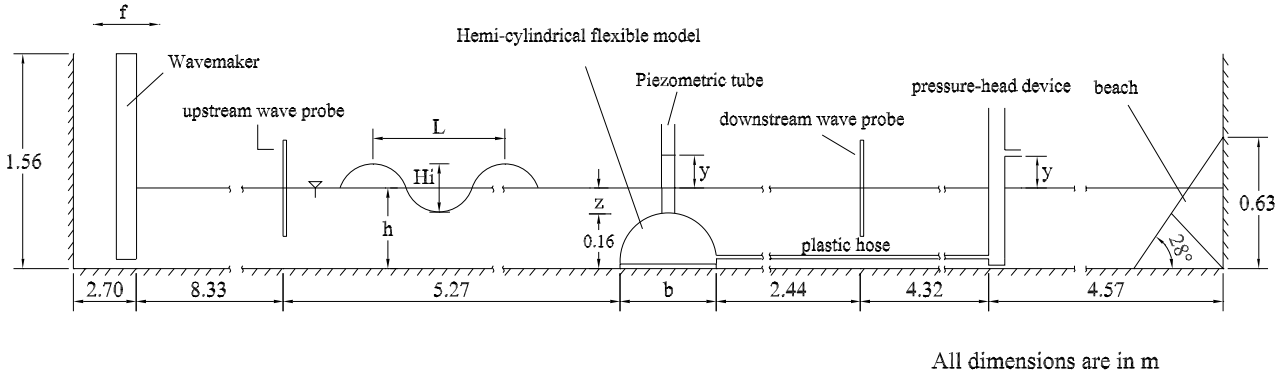

Figure 5.18: Experimental setup of the hemi-cylindrical flexible breakwater model.

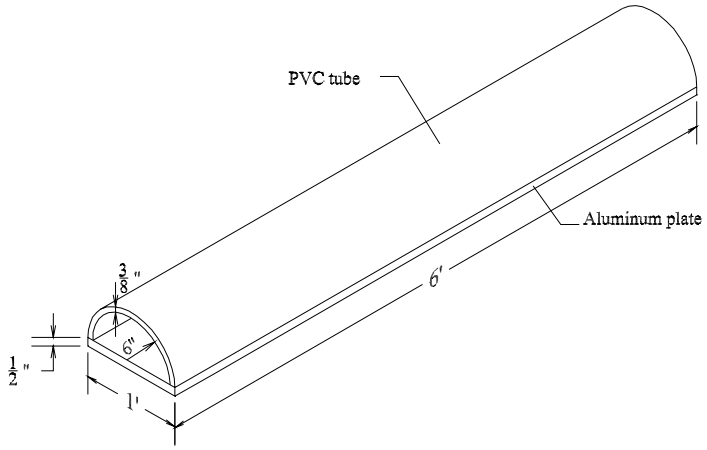

Figure 5.19: Dimensions of hemi-cylindrical rigid breakwater model.

Figure 5.20: Front-view of hemi-cylindrical rigid breakwater model.

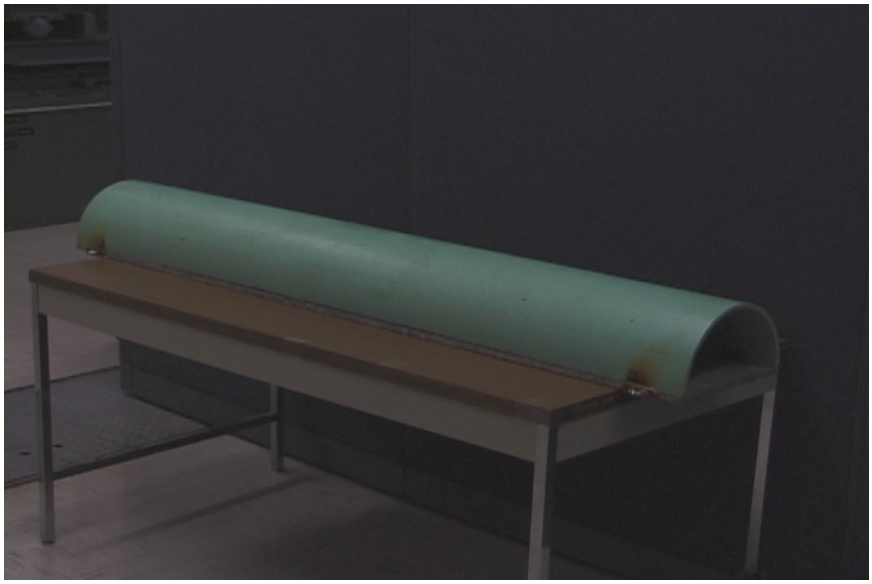

Figure 5.21: Side-view of hemi-cylindrical rigid breakwater model.

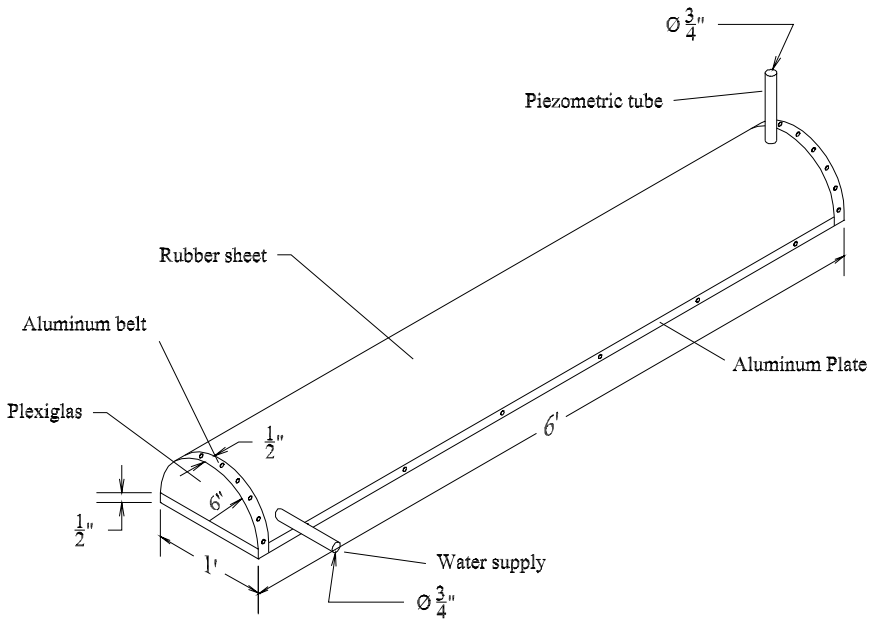

Figure 5.22: Dimensions of hemi-cylindrical flexible breakwater model.

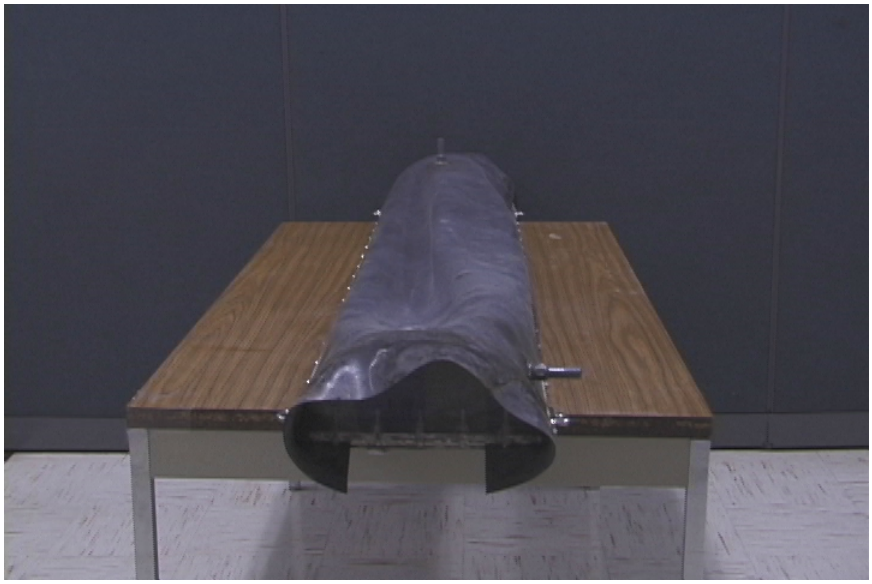

Figure 5.23: Front-view of hemi-cylindrical flexible breakwater model.

Figure 5.24: Side-view of hemi-cylindrical flexible breakwater model.

Figure 5.25: Hemi-cylindrical rigid breakwater model anchored rigidly at the wave tank floor.

Table 5.2: Experimental runs for the hemi-cylindrical rigid and flexible breakwater models.

	Water depth (h), [cm]	z/h	y/h	Wavemaker driving frequency, [Hz]
Rigid model	22.5	0.27		0.6, 0.7, 0.8,...,1.4
Rigid model	27.5	0.40		0.6, 0.7, 0.8,...,1.4
Flexible model	22.5	0.27	0.007	0.6, 0.7, 0.8,...,1.4
		0.27	0.141	0.6, 0.7, 0.8,...,1.4
		0.27	0.282	0.6, 0.7, 0.8,...,1.4
Flexible model	27.5	0.40	0.007	0.6, 0.7, 0.8,...,1.4
		0.40	0.141	0.6, 0.7, 0.8,...,1.4
		0.40	0.282	0.6, 0.7, 0.8,...,1.4

5.3.2 Results and Discussion

The variation of wave steepness, H_i/L, with kh for all waves, when the water depth was 22.5 cm ($z/h = 0.27$), is shown in Figure 5.26. The wave steepness, H_i/L, increases from 0.010 to 0.035 as kh increases from 0.60 to 1.86. The values for the incident height, H_i, are determined from the wavelet analysis. It is interesting to note that H_i/L values, which are determined from

independent experimental runs, are extremely consistent except for $kh = 0.84$, 0.98 and 1.12, where a small difference is noted. This shows the reliability of the wavelet analysis to obtain estimates for H_i.

Variations of reflection, transmission and energy loss coefficients with kh, for the conditions shown in Figure 5.26, are presented in Figure 5.27. The results show that the reflection coefficient, C_r, varies around a value of 0.50 with a dip near $kh = 1.45$ for $y/h = 0.282$. It is also found that the variations in the breakwater's stiffness alter significantly the value of C_r for $kh \geq 1.28$. As for the difference in the reflection characteristics of the rigid and flexible breakwater models, it is found that the average reflection for the rigid model is about 40% for the range of kh studied. For the flexible model, C_r is near 38%, 49% and 46% for y/h ratios of 0.007, 0.141 and 0.282, respectively. These results indicate that the reflection coefficient is slightly higher for $y/h = 0.141$.

As for the transmission coefficient, C_t, it is noted that it varies around a value of 0.60. It is interesting to note, based on Figure 5.27, that for the rigid model and for the flexible model with $y/h = 0.282$, the value of C_t is almost independent of the variations in wave steepness. For $kh \geq 1.45$ the flexible model with $y/h = 0.007$ has significantly lower wave transmission than the rigid model and the flexible models with y/h ratios of 0.141 and 0.282. The rigid model has an average transmission of about 72%, while the flexible model has an average transmission of 54%, 59% and 67% for y/h ratios of 0.007, 0.141 and 0.282, respectively, for the range of kh studied. These results show that C_t decreases with decreasing stiffness of the breakwater. As for the coefficient of energy loss, C_L, the results show that there is no dominant trend throughout the range of kh for all the models. The value of C_L varies around a value of 0.60. The corresponding average values for the energy loss for the rigid and flexible breakwaters with y/h ratios of 0.007, 0.141 and 0.282 are 55%, 69%, 60% and 53%, respectively. This shows that the energy dissipation due to the processes explained in section 2.6 is highest for the flexible model with $y/h = 0.007$ and lowest for the rigid model and for the flexible model with $y/h = 0.282$.

The variation of wave steepness, H_i/L, with kh for all waves, for the rigid and flexible models, when the water depth was 27.5 cm ($z/h = 0.40$), is shown in Figure 5.28. The wave steepness, H_i/L, increases from 0.014 to 0.060 as kh increases from 0.68 to 2.22. The waves considered

here are thus steeper than those in a water depth of 22.5 cm. The values for the incident height, H_i, are determined again from the wavelet analysis and they are consistent for the independent experimental runs involving two different internal pressures.

Variations of reflection coefficient, transmission coefficient and energy loss coefficient with kh for $z/h = 0.40$, for the conditions shown in Figure 5.28, are presented in Figure 5.29. The results show that C_r varies near 0.30. For $kh \leq 1.29$, it is found that the different breakwater stiffnesses do not have a significant influence on the variations of C_r, whereas for $kh \geq 1.48$ the value of C_r alters with the stiffness. As for the transmission coefficient, C_t, the results show values above 0.50 for all models, with a minimum value of 0.38 at $kh = 2.22$ for the flexible model with y/h ratio of 0.007. The results also show that C_t tends to increase with increase in stiffness in that the rigid model transmits higher energy than the flexible model almost throughout all the range of kh. The energy dissipation varies near 0.50 and it is maximum for the flexible model with $y/h = 0.007$ when $kh \leq 1.11$ and $kh \geq 1.70$. For the rigid model, the average value of C_r is found to be about 24% and those of C_t and C_L are about 78% and 55%, respectively, for the range of kh studied. For the flexible model with $y/h = 0.007$, 0.141 and 0.282 the average values are 38%, 37% and 34% for the wave reflection, 61%, 74% and 78% for the wave transmission and 66%, 53% and 51% for the energy loss.

In order to determine the effect of model width, variations of all three coefficients are discussed at constant submergence depth ratio, z/h, substituting the kh parameter with the model width to wave length ratio, b/L. The model width for both breakwater models is kept constant at 0.30m and the incident wave length, L, is varied from 0.76 to 2.34 m for the case of $z/h = 0.27$ and from 0.78 to 2.55m for the case of $z/h = 0.40$. For the case of $z/h = 0.27$, the values of the b/L ratio are varied between 0.130 and 0.401. Based on Figure 5.27, the optimum b/L ratio for the flexible model with $y/h = 0.007$ is between 0.314 and 0.401, where the wave transmission is minimum and the energy loss is maximum. For the rigid model, it is not clear which b/L ratio is optimum since its C_t does not have any distinguished minimum value. As for the case of $z/h = 0.40$, the value of b/L is varied between 0.119 and 0.392. Again, an optimum b/L ratio is visible only for the flexible model with $y/h = 0.007$. For this case the wave transmission is minimum and wave energy loss maximum if b/L is between 0.300 and 0.392. The wave reflection is also high at this range of b/L ratio.

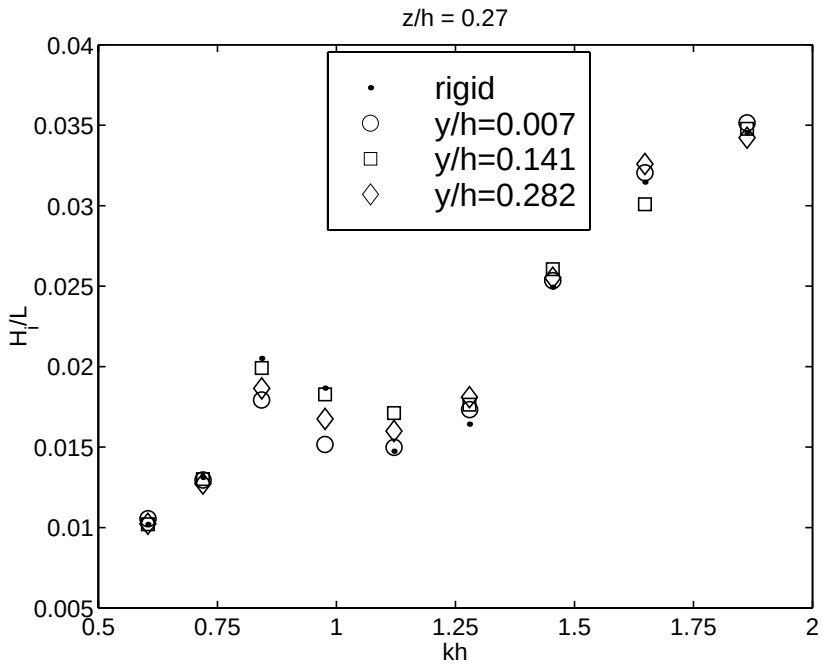

Figure 5.26: Variation of wave steepness with kh for the hemi-cylindrical rigid and flexible models. Water depth 22.5 cm.

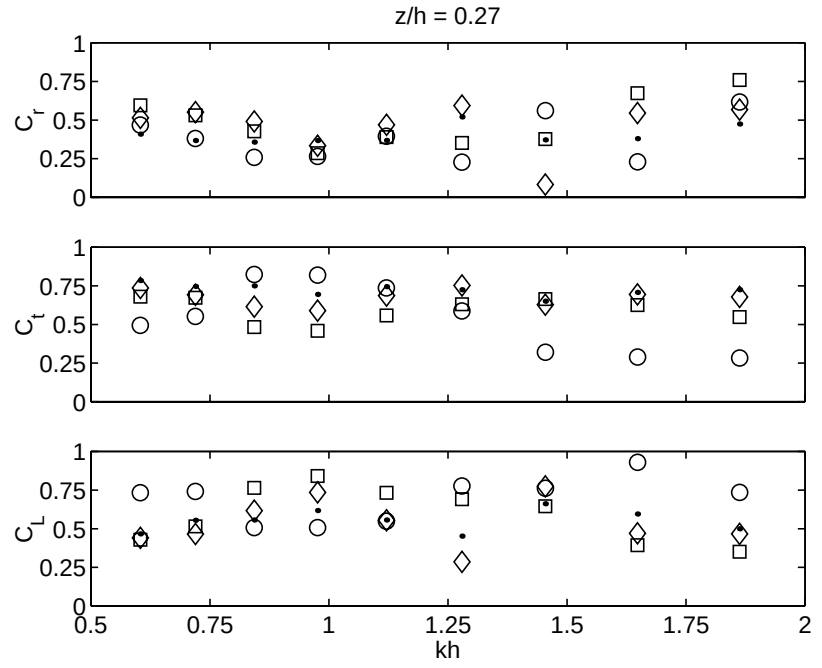

Figure 5.27: Variations of wave coefficients with kh for the hemi-cylindrical rigid and flexible models. Water depth 22.5 cm. For legend see Figure 5.26.

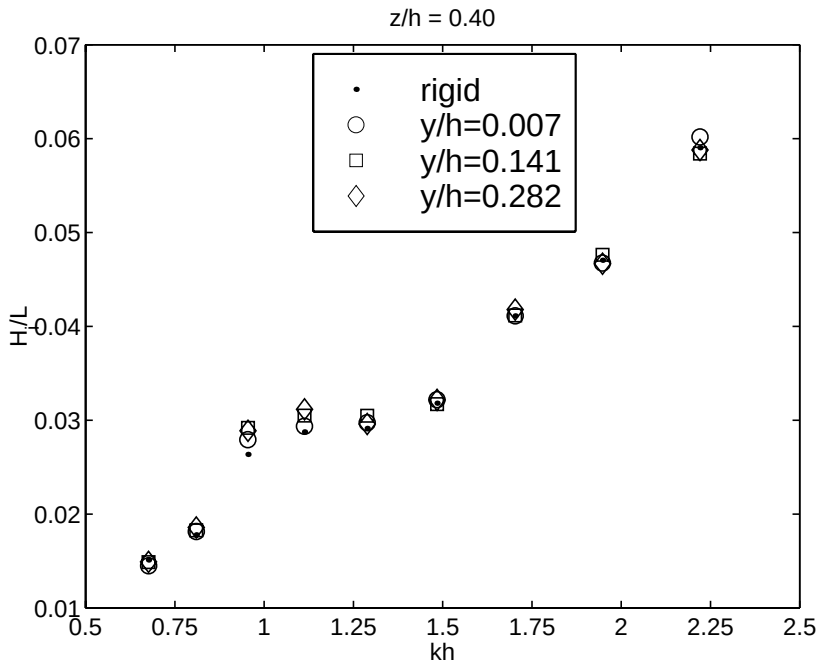

Figure 5.28: Variation of wave steepness with kh for the hemi-cylindrical rigid and flexible models. Water depth 27.5 cm.

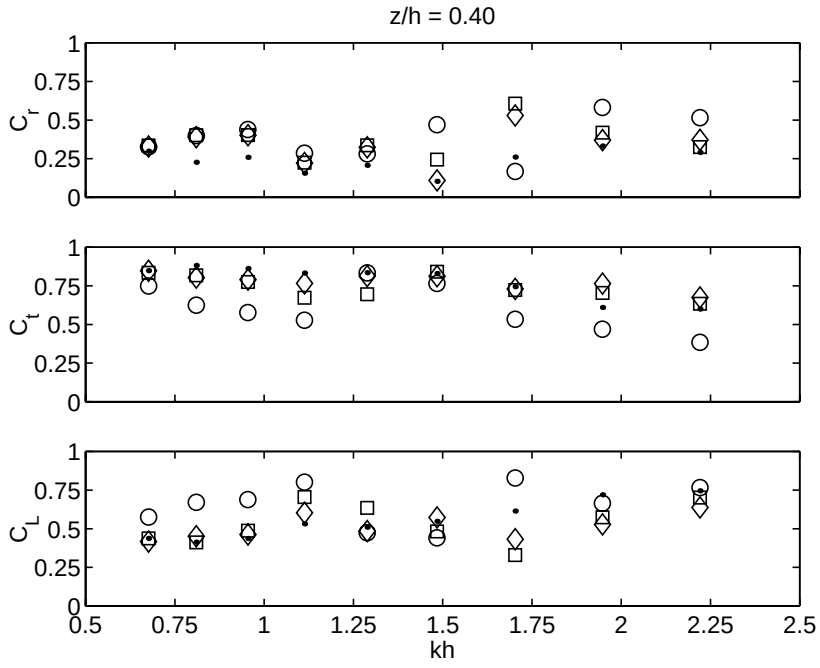

Figure 5.29: Variations of wave coefficients with kh for the hemi-cylindrical rigid and flexible models. Water depth 27.5 cm. For legend see Figure 5.28.

5.3.3 Conclusions

By comparing the average values of the wave coefficients for both models and all internal flexible model pressures, it can be concluded that the lower submergence depth ratio, $z/h = 0.27$, causes higher wave reflection, lower wave transmission and higher energy loss than the high submergence depth ratio of 0.40. The results also show that for both submergence depth ratios, rigid and flexible models with $y/h = 0.141$ and 0.282 transmit most of the wave energy, dissipate some and reflect only a low portion. As for the flexible model with $y/h = 0.007$, most of the wave energy is dissipated, some is transmitted and the remaining lowest portion is reflected. This is most likely because the flexible model with the lower internal pressure has the ability of oscillating in different modes and possibly dissipating the incoming waves more easily. Since the effectiveness of a breakwater basically depends on the height of transmitted waves, the average values of transmission coefficients show that the effectiveness increases, translating to lower height of transmitted waves, as the stiffness of the models decreases. Thus, the flexible model with $y/h = 0.007$ is the most effective breakwater and the rigid the least effective.

The variation in the wave steepness, H_i/L, influences most the variations of the wave reflection for both submergence depth ratios. This is more pronounced for the flexible model for all internal pressures as the wave steepness increases. The wave transmission varies significantly with the wave steepness only for the flexible model with $y/h = 0.007$ for both submergence depth ratios.

5.4 Wave Coefficients Over First Hemi-Cylindrical Flexible Composite Breakwater

5.4.1 Experimental Setup and Testing Conditions

The drawing of the experimental setup is identical to the one presented in Figure 5.18 for the hemi-cylindrical flexible breakwater model. The breakwater model is constructed out of high-grade neoprene rubber of medium hardness with thickness of 0.158 cm (1/16 in) and modulus of elasticity 3675 KPa (533 psi). The rubber sheet is reinforced with four composite strips that are each 1.22 m (4 ft) long and made of 40% (vol) AS-4 carbon fibers in polyphenol sulfide matrix. The composite strips are attached uniformly onto the surface of the rubber sheet along the longitudinal direction, as shown in Figure 5.30. Each of them has a cross section of 1.27cm x 0.10cm (0.5in x 0.04in). The rubber sheet is finally fastened, as explained in section 5.3.1 for the hemi-cylindrical flexible model, on a 1.83m x 0.30m (6ft x 1ft) aluminum flat plate.

The author finds it appropriate to describe the procedure that was followed to attach the composite strips to the neoprene rubber sheet. At the beginning, Devlon rubber adhesive was applied to the first composite strip. We noticed sections of the strip becoming uncovered as the drying adhesive crept back to a state of lesser deformation. Immediately after covering the composite strip, we applied adhesive to the line on the rubber sheet where the strip would sit. The composite strip was laid on the rubber and manual pressure was applied for about 5 minutes. This procedure was repeated for the other three composite strips. On the first two strips, a seal was established by smearing adhesive along the sides of the composite strips. This was not repeated on the third and fourth strips, because we decided we would apply a silicon rubber sealant before putting the model in use. Excess adhesive was removed. The adhesive was left to cure under no pressure.

Photos of the first hemi-cylindrical flexible composite breakwater model are presented in Figures 5.31 and 5.32. The model was anchored rigidly at the tank floor with steel-nylon cables using four stainless steel pad-eyes placed on the aluminum plate and four hooks permanently connected to the tank bottom. Thus, the model did not float or move when subjected to wave action. We also made sure that there was no contact between the model ends and wave tank

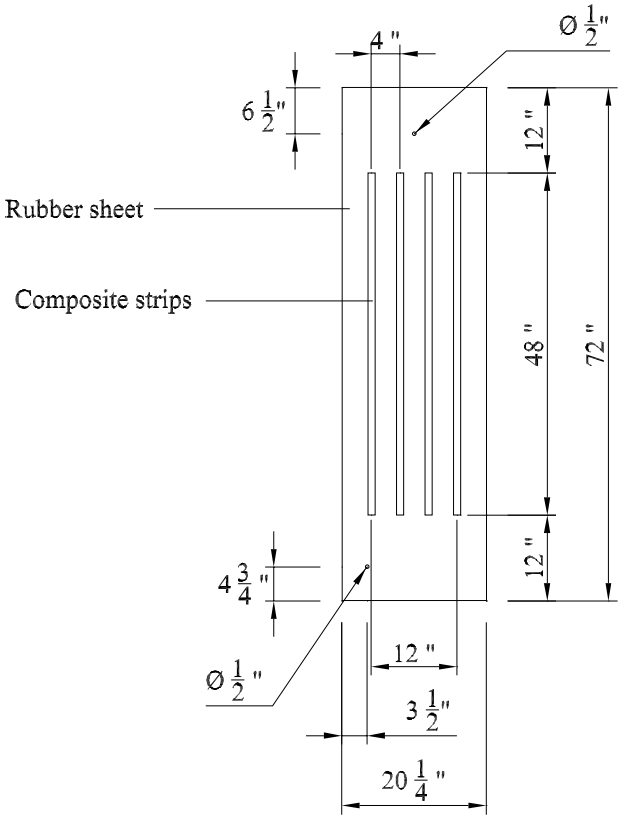

Figure 5.30: Dimensions of rubber sheet and composite strips along its longitudinal direction.

walls during the experiments.

Tests for different wave frequencies and amplitudes, yielding different wave steepnesses, $\frac{H_i}{L}$, were conducted at water depths of 22.5 cm ($z/h = 0.27$) and 27.5 cm ($z/h = 0.40$). We also considered y/h ratios of 0.007, 0.141 and 0.282 at each water depth. All the experimental runs are summarized and presented in Table 5.3. The experimental runs for the hemi-cylindrical rigid model presented in section 5.3 are also included.

Figure 5.31: Front-view of the first hemi-cylindrical flexible composite breakwater model.

Figure 5.32: Side-view of the first hemi-cylindrical flexible composite breakwater model.

Table 5.3: Experimental runs for the hemi-cylindrical rigid and first flexible composite breakwater models.

	Water depth (h), [cm]	z/h	y/h	Wavemaker driving frequency, [Hz]
Rigid model	22.5	0.27		0.6, 0.7, 0.8,...,1.4
Rigid model	27.5	0.40		0.6, 0.7, 0.8,...,1.4
Composite model	22.5	0.27	0.007	0.6, 0.7, 0.8,...,1.4
		0.27	0.141	0.6, 0.7, 0.8,...,1.4
		0.27	0.282	0.6, 0.7, 0.8,...,1.4
Composite model	27.5	0.40	0.007	0.6, 0.7, 0.8,...,1.4
		0.40	0.141	0.6, 0.7, 0.8,...,1.4
		0.40	0.282	0.6, 0.7, 0.8,...,1.4

5.4.2 Results and Discussion

The variation of wave steepness, H_i/L, with kh for all waves, when the water depth was 22.5 cm ($z/h = 0.27$), is shown in Figure 5.33. The wave steepness, H_i/L, increases from 0.010 to 0.035 as kh increases from 0.60 to 1.86. The values for the incident height, H_i, are determined again from the wavelet analysis. It is interesting to note that H_i/L values, which are determined from independent experimental runs, are extremely consistent except for $kh = 0.84$ and 0.98 where a small difference is noted. This shows the reliability of the analysis technique in obtaining estimates for H_i.

Variations of reflection, transmission and energy loss coefficients with kh, for the conditions shown in Figure 5.33, are given in Figure 5.34. The results show that the reflection coefficient, C_r, varies around a value of 0.40. As for the difference in the reflection characteristics of the rigid and flexible composite breakwaters, it is found that the average reflection for the rigid model is about 40%, for the range of kh studied. For the flexible composite model, C_r is near 44%, 40% and 36% for y/h ratios of 0.007, 0.141 and 0.282, respectively. These results indicate that the models' stiffness does not have any significant influence on the wave reflection. For

the transmission coefficient, C_t, the results show values above 0.5 for all models with minimum values of 0.26 and 0.29 at $kh = 0.84$ and 1.86, respectively, for the flexible composite model with $y/h = 0.007$. For $kh \leq 0.84$ and $kh \geq 1.28$ the flexible composite model with $y/h = 0.007$ transmits the lowest wave energy. Surprisingly, the results also show that the rigid model transmits slightly lower wave energy than the flexible composite models with $y/h = 0.141$ and 0.282 throughout the range of kh. The C_t values for the composite model with $y/h = 0.141$ and 0.282 are very close to each other for the range of kh studied. The rigid model has an average transmission of about 72%, while the flexible composite model has an average transmission of 57%, 78% and 81% for y/h ratios of 0.007, 0.141 and 0.282, respectively, for the range of kh studied. As for the coefficient of energy loss, C_L, the results show that it varies around a value of 0.50 for all the models. The corresponding average values for the energy loss for the rigid and flexible composite breakwaters with y/h ratios of 0.007, 0.141 and 0.282 are 55%, 60%, 41% and 42%, respectively. Again, the flexible composite model with $y/h = 0.007$ and the rigid model have the best performance, dissipating the highest wave energy.

The variation of wave steepness, H_i/L, with kh for all waves, for the rigid and flexible composite models, when the water depth was 27.5 cm ($z/h = 0.40$), is shown in Figure 5.35. The wave steepness, H_i/L, increases from 0.015 to 0.060 as kh increases from 0.68 to 2.22. The waves considered here are thus steeper than those in a water depth of 22.5 cm. Again, the H_i/L values for the same kh are very close together, indicating repeatable estimates for the incident wave height, H_i, from the wavelet analysis.

Variations of reflection coefficient, transmission coefficient and energy loss coefficient with kh for $z/h = 0.40$, for the conditions shown in Figure 5.35, are presented in Figure 5.36. The results show that C_r varies near 0.30 for $kh \leq 1.29$ and near 0.40 for $kh \geq 1.48$. As for the transmission coefficient, C_t, the results show values above 0.60 for all models with a minimum value of 0.53 at $kh = 1.11$ for the flexible composite model with $y/h = 0.007$. The results also show that C_t is minimum for the flexible composite model with $y/h = 0.007$ throughout the range of kh. The energy dissipation varies around a value of 0.50. For $kh \leq 1.29$ the flexible composite model with $y/h = 0.007$ dissipates the highest wave energy, while for $kh \geq 1.48$ the rigid model is more effective in dissipating the incident wave energy.

For the rigid model, the average value of C_r is found to be about 24% and those of C_t and C_L

are about 78% and 55%, respectively, for the range of kh studied. For the flexible composite model with $y/h = 0.007$, 0.141 and 0.282 the average values are 41%, 32% and 28% for the wave reflection, 70%, 87% and 89% for the wave transmission and 54%, 35% and 32% for the energy loss. These results show that the flexible composite model with $y/h = 0.007$ has the best performance since it reflects and dissipates the highest wave energy. The rigid model also dissipates high wave energy but reflects the lowest wave energy back. Although the other two flexible composite models with $y/h = 0.141$ and 0.282 reflect higher wave energy compared to the rigid model, they are less effective since they transmit higher waves.

In order to determine again the effect of model width, variations of all three coefficients are discussed at a constant submergence depth ratio, z/h, substituting the kh parameter with the model width to wave length ratio, b/L. The model width for both breakwater models is kept constant at 0.30 m and the incident wave length, L, is varied from 0.76 to 2.34 m for the case of $z/h = 0.27$ and from 0.78 to 2.55 m for the case of $z/h = 0.40$. For the case of $z/h = 0.27$, the values of the b/L ratio are varied between 0.130 and 0.401. Based on Figure 5.34, the optimum b/L ratio for the flexible composite model with $y/h = 0.007$ is between 0.130 and 0.182, where the wave transmission is minimum and the wave reflection and wave energy loss are very high. Moreover, another optimum b/L ratio for the flexible composite model with $y/h = 0.007$ is between 0.355 and 0.401, where the wave transmission is also minimum and the wave energy loss is maximum. For the rigid model it is not clear which b/L ratio is optimum since its C_t values do not have any significant distinguished minimum value.

As for the case of $z/h = 0.40$, the value of b/L is varied between 0.119 and 0.392. Based on Figure 5.44, the optimum b/L ratio for the flexible composite model with $y/h = 0.007$ is between 0.196 and 0.227, where the wave transmission is minimum and the wave energy loss is maximum. Another optimum b/L ratio for the flexible composite model with $y/h = 0.007$ and the rigid model is between 0.344 and 0.392 (maximum wave steepness), where the wave transmission is minimum and wave energy loss and wave reflection are maximum.

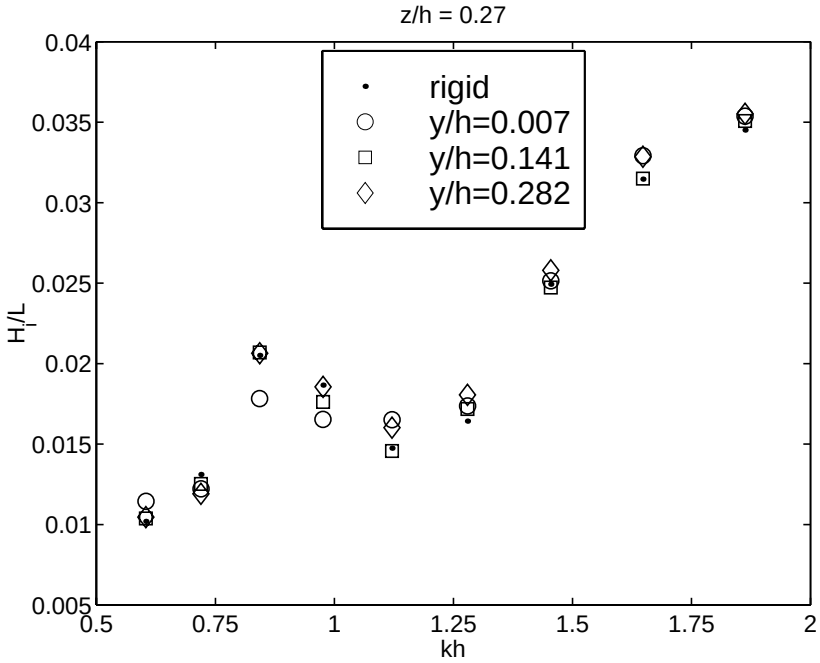

Figure 5.33: Variation of wave steepness with kh for the hemi-cylindrical rigid and first flexible composite models. Water depth 22.5 cm.

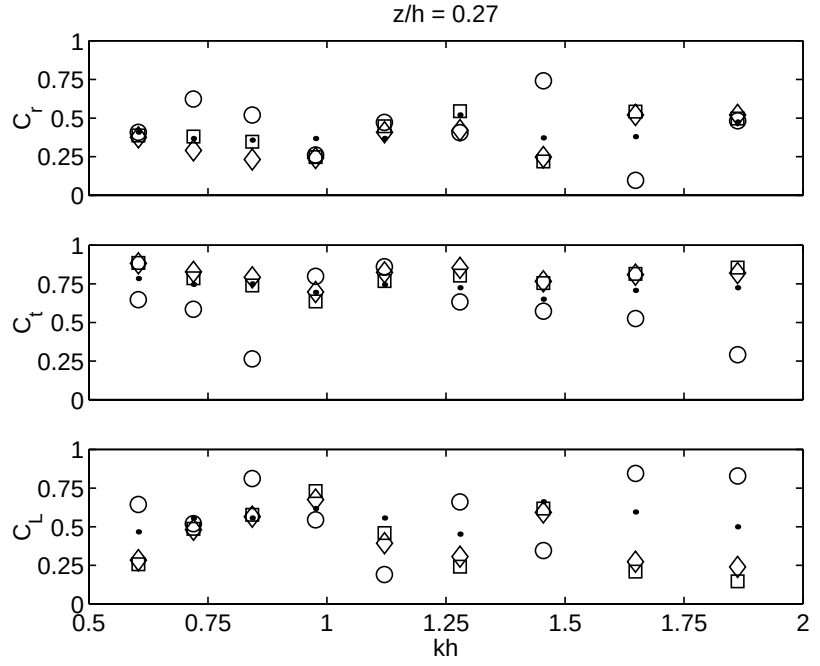

Figure 5.34: Variations of wave coefficients with kh for the hemi-cylindrical rigid and first flexible composite models. Water depth 22.5 cm. For legend see Figure 5.33.

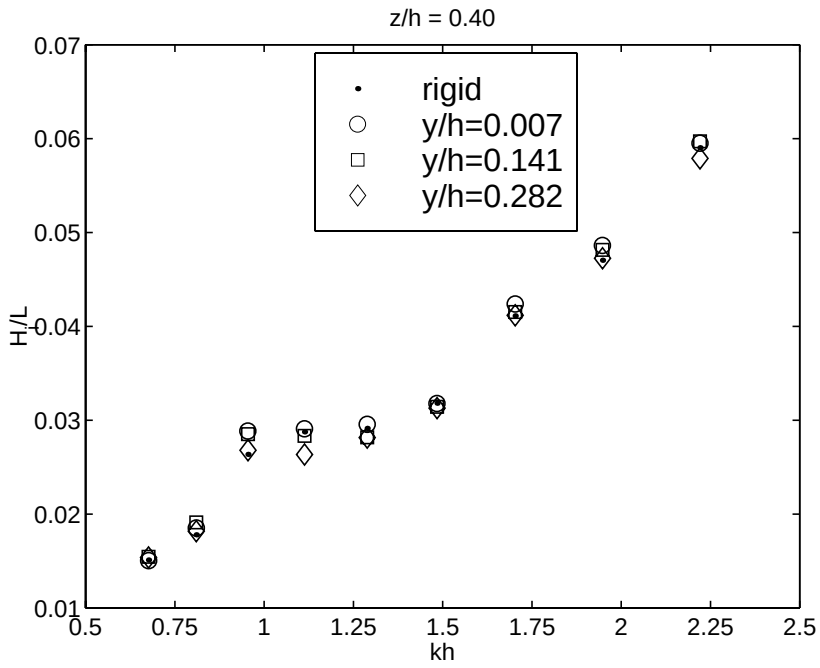

Figure 5.35: Variation of wave steepness with kh for the hemi-cylindrical rigid and first flexible composite models. Water depth 27.5 cm.

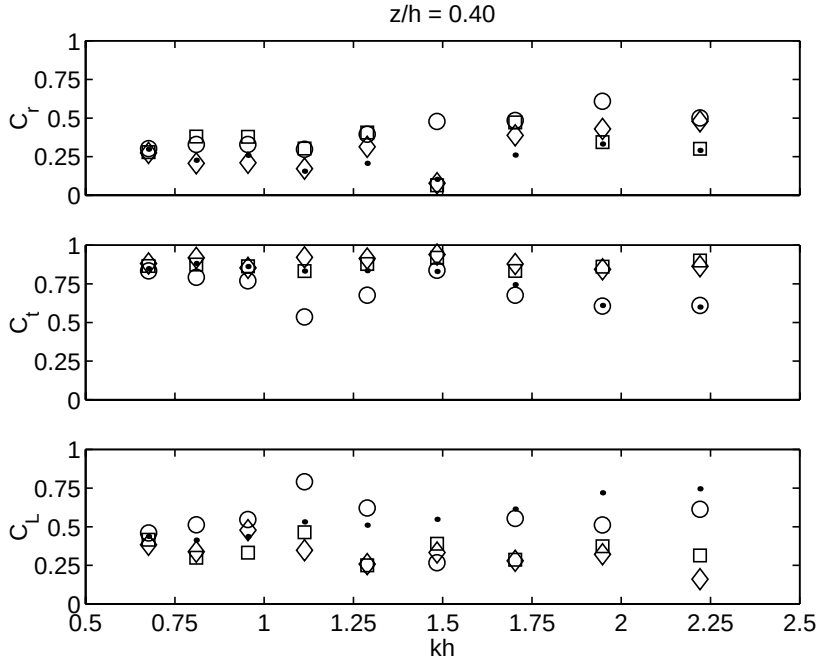

Figure 5.36: Variations of wave coefficients with kh for the hemi-cylindrical rigid and first flexible composite models. Water depth 27.5 cm. For legend see Figure 5.35.

5.4.3 Conclusions

By comparing the average values of the wave coefficients for both models and all internal flexible composite models' pressures, it can be concluded that the lower submergence depth ratio, $z/h = 0.27$, causes higher wave reflection, lower wave transmission and higher energy loss than the high submergence depth ratio of 0.40. The results also show that for a submergence depth ratio of 0.27, rigid and flexible composite with $y/h = 0.141$ and 0.282 models transmit most of the wave energy. As for the flexible composite model with $y/h = 0.007$, most of the wave energy is equally dissipated and transmitted and the remaining portion is reflected. For a submergence depth ratio of 0.40, most of the wave energy is transmitted for both breakwater models. Based on the order of the average values of transmission coefficient, C_t, and energy loss coefficient, C_L for both submergence depth ratios, we can conclude that the flexible composite model with $y/h = 0.007$ and the rigid model are the most effective breakwaters. Moreover, this also indicates that the flexible composite models with $y/h = 0.141$ and 0.282 respond to the waves and behave as if they were even stiffer than the rigid model.

Based on the results, the variation in the wave steepness influences most the variations of the wave reflection for both submergence depth ratios for both models. The wave transmission varies significantly with the wave steepness only for the flexible composite model with $y/h = 0.007$ for both submergence depth ratios.

5.5 Wave Coefficients Over Second Hemi-Cylindrical Flexible Composite Breakwater

5.5.1 Experimental Setup and Testing Conditions

The drawing of the experimental setup is identical to the one presented in Figure 5.18 for the hemi-cylindrical flexible breakwater model. The breakwater model is constructed out of high-grade neoprene rubber of medium hardness with thickness of 0.158 cm (1/16 in) and modulus of elasticity 3675 KPa (533 psi). The rubber sheet is reinforced with eleven composite strips, made of 40% (vol) AS-4 carbon fibers in polyphenol sulfide matrix. Four of the composite strips, that are each 1.22 m (4 ft) long, are attached uniformly onto the surface of the rubber sheet, along its longitudinal direction and seven of them, that are each 0.46 m (1.5 ft) long, are attached uniformly onto the surface of the rubber sheet, along the hoop direction, as shown in Figure 5.37. The longitudinal strips are on top of the hoop strips. Each of them has a cross section of 1.27cm x 0.10cm (0.5in x 0.04in). The rubber sheet is fastened, as explained in section 5.3.1 for the hemi-cylindrical flexible model, on a 1.83m x 0.30m (6ft x 1ft) aluminum flat plate.

Photos of the second hemi-cylindrical flexible composite breakwater model are presented in Figures 5.38 and 5.39. Moreover, in Figure 5.40, the hemi-cylindrical rigid and flexible composite breakwater models are presented. Again, the breakwater model was anchored rigidly at the tank floor with steel-nylon cables using four stainless steel pad-eyes placed on the aluminum plate and four hooks permanently connected to the tank bottom. Thus, the model did not float or move when subjected to wave action. We also made sure that there was no contact between the model ends and the wave tank walls during the experiments.

Tests for different wave frequencies and amplitudes, yielding different wave steepnesses, $\frac{H_i}{L}$, were conducted at water depths of 22.5 cm ($z/h = 0.27$) and 27.5 cm ($z/h = 0.40$). We also considered y/h ratios of 0.007, 0.141 and 0.282 at each water depth. All the experimental runs are summarized and presented in Table 5.4. The experimental runs for the hemi-cylindrical rigid model presented in section 5.3 are also included.

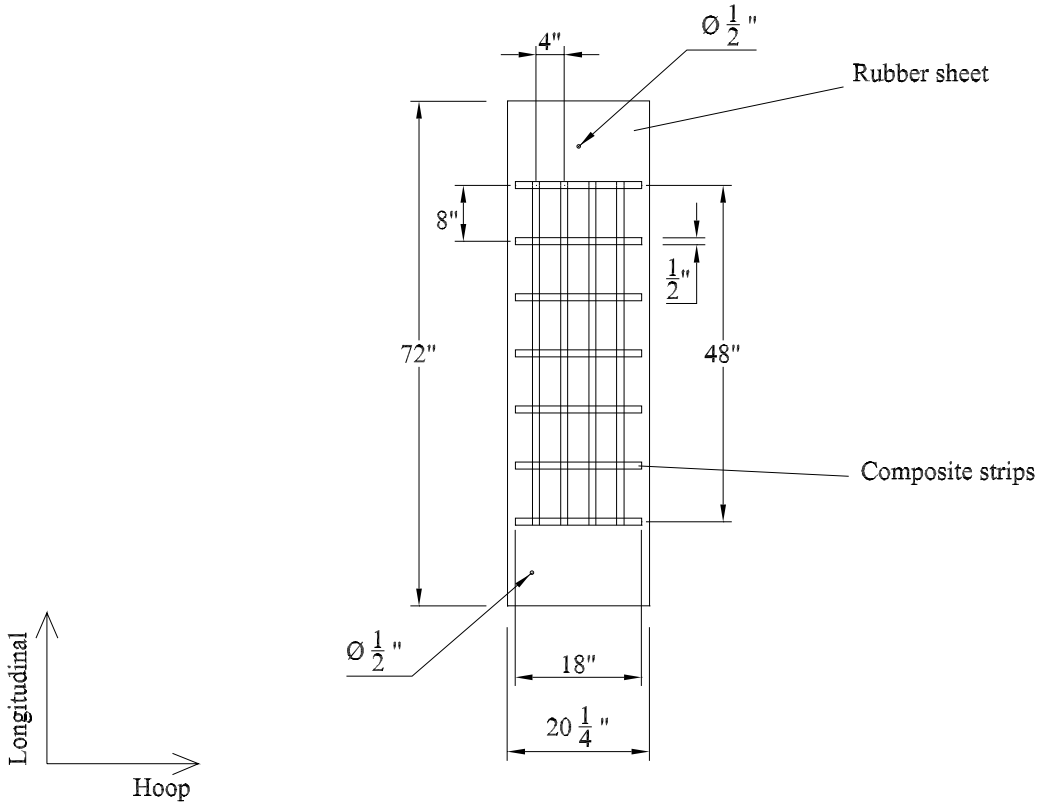

Figure 5.37: Dimensions of rubber sheet and composite strips along its longitudinal and hoop directions.

5.5.2 Results and Discussion

The variation of wave steepness, H_i/L, with kh for all waves, when the water depth was 22.5 cm ($z/h = 0.27$), is shown in Figure 5.41. The wave steepness, H_i/L, increases from 0.010 to 0.035 as kh increases from 0.60 to 1.86. The values for the incident height, H_i, are determined from the wavelet analysis. It is interesting to note that H_i/L values, which are determined from independent experimental runs, are consistent except for $kh = 0.84$, 0.98 and 1.28, where a small difference is noted. This shows the reliability of the analysis technique in obtaining estimates for H_i.

Variations of reflection, transmission and energy loss coefficients with kh, for the conditions shown in Figure 5.41, are given in Figure 5.42. The results show that the reflection coefficient,

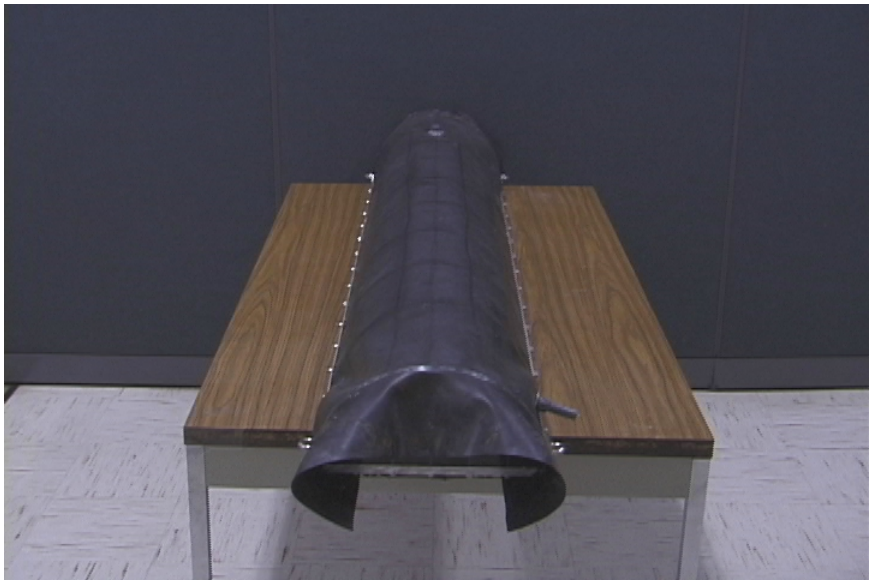

Figure 5.38: Front-view of the second hemi-cylindrical flexible composite breakwater model.

Figure 5.39: Side-view of the second hemi-cylindrical flexible composite breakwater model.

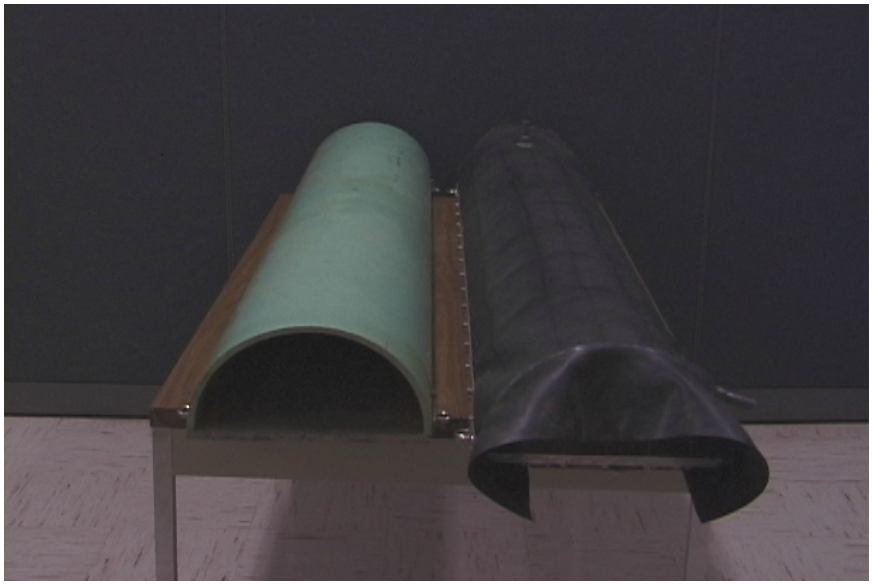

Figure 5.40: Front-view of the hemi-cylindrical rigid and second flexible composite breakwater models.

Table 5.4: Experimental runs for the hemi-cylindrical rigid and second flexible composite breakwater models.

	Water depth (h), [cm]	z/h	y/h	Wavemaker driving frequency, [Hz]
Rigid model	22.5	0.27		0.6, 0.7, 0.8,...,1.4
Rigid model	27.5	0.40		0.6, 0.7, 0.8,...,1.4
Composite model	22.5	0.27	0.007	0.6, 0.7, 0.8,...,1.4
		0.27	0.141	0.6, 0.7, 0.8,...,1.4
		0.27	0.282	0.6, 0.7, 0.8,...,1.4
Composite model	27.5	0.40	0.007	0.6, 0.7, 0.8,...,1.4
		0.40	0.141	0.6, 0.7, 0.8,...,1.4
		0.40	0.282	0.6, 0.7, 0.8,...,1.4

C_r varies around 0.5 with a slight dip near $kh = 1.45$. As for the difference in the reflection characteristics of the rigid and second flexible composite breakwaters, it is found that the average reflection for the rigid model is about 40% for the range of kh studied. For the flexible composite model, C_r is near 59%, 44% and 42% for y/h ratios of 0.007, 0.141 and 0.282, respectively. For the transmission coefficient, C_t, the results show values above 0.60 for the rigid model and flexible composite models with $y/h = 0.141$ and 0.282. As for the flexible composite model with $y/h = 0.007$, the results show that lower wave energy is transmitted throughout the range of kh. In that case, C_t values are above 0.40. The rigid model has an average transmission of about 72%, while the flexible composite model has an average transmission of 54%, 70% and 74% for y/h ratios of 0.007, 0.141 and 0.282, respectively, for the range of kh studied. The results also show that C_L varies near 0.60 for $kh \leq 0.98$ and $kh \geq 1.45$. In between, the values of C_L are lower and vary near 0.40. The corresponding average values for the energy loss for the rigid and flexible composite breakwaters with y/h ratios of 0.007, 0.141 and 0.282 are 55%, 56%, 51% and 48%, respectively.

The variation of wave steepness, H_i/L, with kh for all waves, for the rigid and flexible composite models, when the water depth is 27.5 cm ($z/h = 0.40$), is shown in Figure 5.43. The wave steepness, H_i/L, increases from 0.015 to 0.060 as kh increases from 0.68 to 2.22. The waves considered here are thus steeper than those in a water depth of 22.5 cm. The values for the incident height, H_i, are determined again from the wavelet analysis and they are consistent for the independent experimental runs involving two different internal pressures.

Variations of reflection coefficient, transmission coefficient and energy loss coefficient with kh for $z/h = 0.40$, for the conditions shown in Figure 5.43, are presented in Figure 5.44. The results show that the reflection coefficient, C_r, values are below 0.50 for all models, with a maximum value of 0.68 near $kh = 1.70$ for the flexible composite model with y/h ratio of 0.007. The flexible composite model with $y/h = 0.007$ seems to reflect back the highest wave energy throughout the range of kh. The results also show that the transmission coefficient, C_t, values are above 0.50 for all models. The value of C_t is almost independent of the variations in the models' stiffness for $kh \leq 1.70$. The flexible composite model with $y/h = 0.007$ transmits the lowest wave energy throughout the range of kh. As for the energy loss coefficient, C_L, the results show that it varies near 0.50 for all models.

For the rigid model, the average value of C_r is found to be about 24% and those of C_t and C_L are about 78% and 55%, respectively, for the range of kh studied. For the flexible composite model with $y/h = 0.007$, $y/h = 0.141$ and 0.282 the average values are 43%, 35% and 32% for the wave reflection, 71%, 80% and 83% for the wave transmission and 51%, 46% and 43% for the energy loss.

In order to determine the effect of model width, variations of all three coefficients are discussed at constant submergence depth ratio, z/h, substituting the kh parameter with the model width to wave length ratio, b/L. The model width for both breakwater models is kept constant at 0.30 m and the incident wave length, L, is varied from 0.76 to 2.34 m for the case of $z/h = 0.27$ and from 0.78 to 2.55 m for the case of $z/h = 0.40$. For the case of $z/h = 0.27$, the values of b/L ratio are varied between 0.130 and 0.401. Based on Figure 5.42, the optimum b/L ratio for the flexible composite model with $y/h = 0.007$ is between 0.182 and 0.210, where the wave transmission is low and the wave reflection and wave energy loss are high. Moreover, another optimum b/L ratio for the flexible composite model with $y/h = 0.007$ is between 0.355 and 0.401, where the wave transmission is minimum, the wave reflection is maximum and the energy loss high. For the rigid model, it is not clear which b/L ratio is optimum since its C_t values do not have any significant minimum value. As for the case of $z/h = 0.40$, the value of b/L is varied between 0.119 and 0.392. Based on Figure 5.44, the optimum b/L ratio for the flexible composite model with $y/h = 0.007$ and the rigid model is between 0.344 and 0.392 (maximum wave steepness), where the wave transmission is minimum and wave energy loss maximum. The wave reflection is also high for the flexible composite model and maximum for the rigid model.

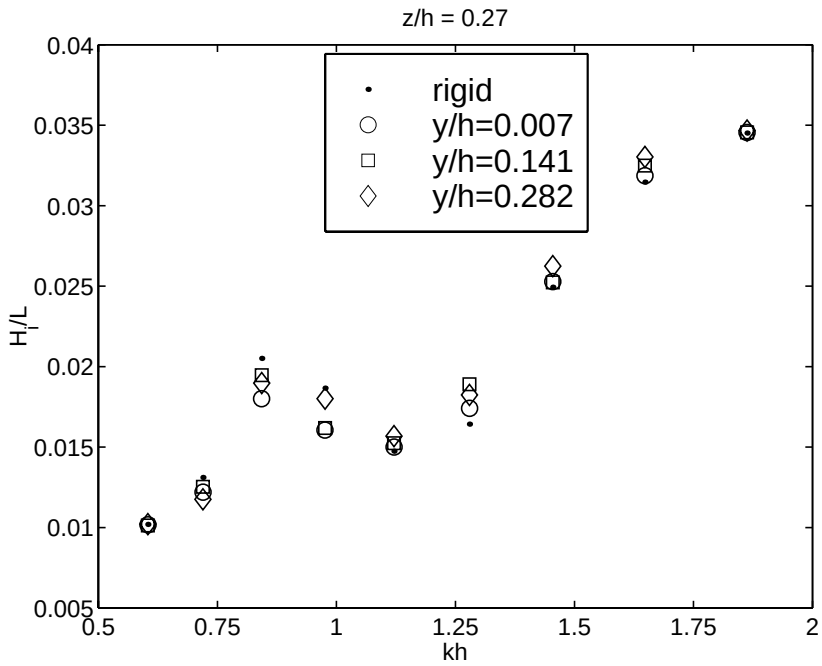

Figure 5.41: Variation of wave steepness with kh for the rigid and second flexible composite models. Water depth 22.5 cm.

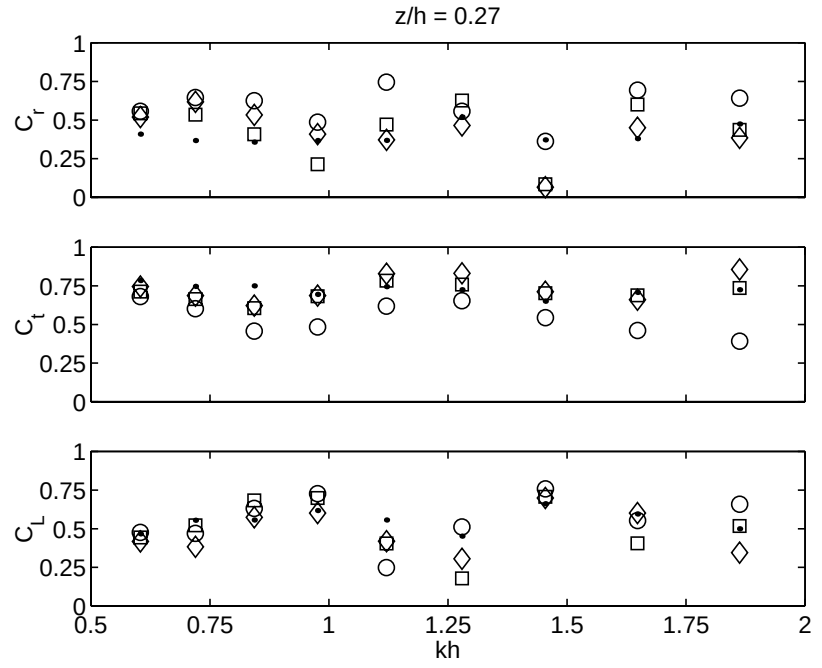

Figure 5.42: Variations of wave coefficients with kh for the rigid and second flexible composite models. Water depth 22.5 cm. For legend see Figure 5.41.

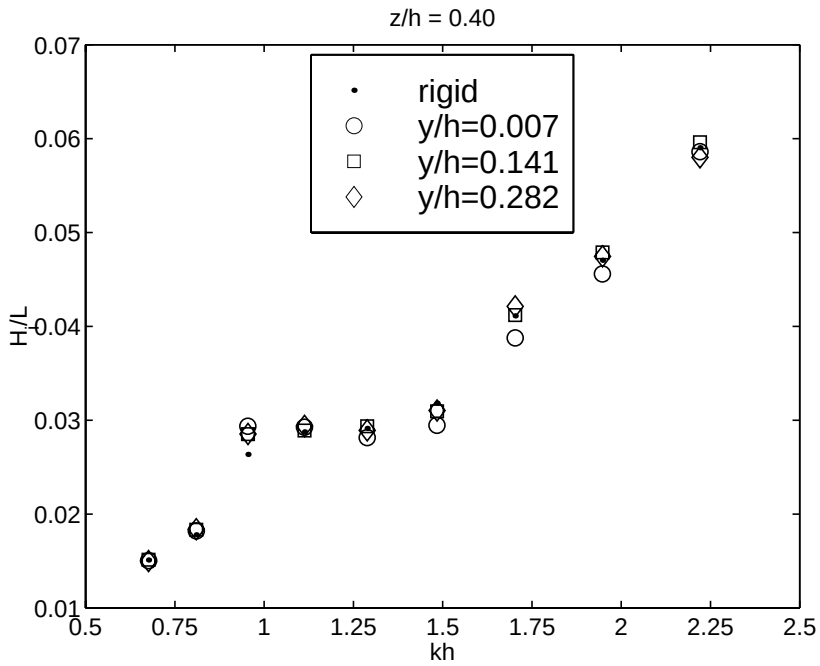

Figure 5.43: Variation of wave steepness with kh for the rigid and second flexible composite models. Water depth 27.5 cm.

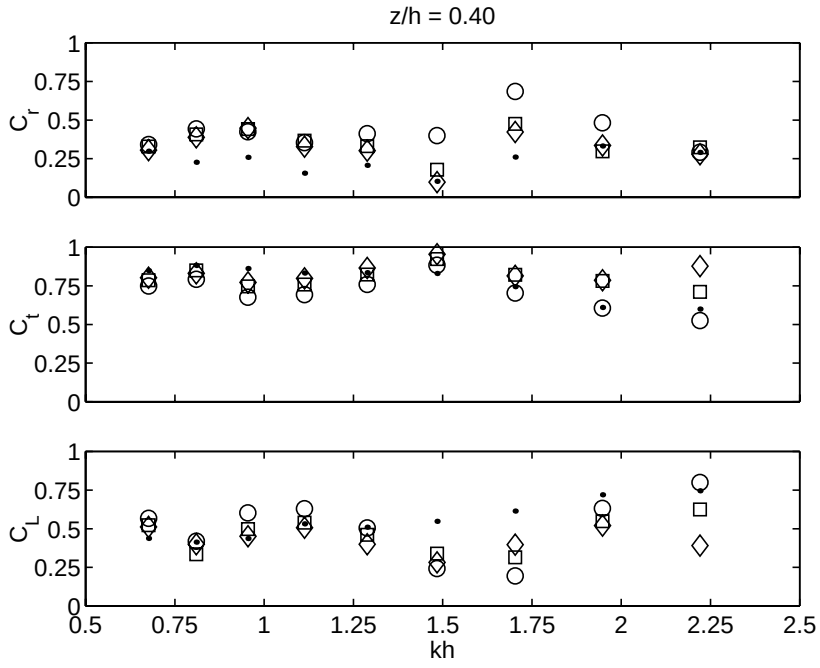

Figure 5.44: Variations of wave coefficients with kh for the rigid and second flexible composite models. Water depth 27.5 cm. For legend see Figure 5.43.

5.5.3 Flow Visualization

Flow visualization has from early times played an important part in research, always yielding qualitative insight, and recently also quantitative results. In this section, we present our flow visualization technique. Generally, in order to visualize a flow, different substances can be introduced in the field to act as tracers of the motion of the fluid. In our technique, white particles were added in the flow field as tracers. The flow was illuminated in order to increase contrast and resolution of the particle images. The resulting flow pattern was captured using a digital video camera recorder.

Two lamps by Berkey ColorTran Inc. were used to provide a white light source. Their maximum power was 1000 Watts. They were hung with cables on the towing carriage of the wave tank. An aluminum prism with dimensions of 0.91m x 0.91m x 0.15m (3ft x 3ft x 6in) was constructed in order to gather the white scaterred light from the lamps into a light sheet. The prism has input and output opening slots of 0.91m x 5.08cm (3ft x 2in) at its top and bottom, respectively, and was hung also on the towing carriage between the lamps and the free water surface. As shown in Figure 5.45, the space between the lamps and the prism was covered with a black box sitting on the prism in order to collect all the light into the input slot and avoid any light escaping in the surroundings. The light sheet is positioned right above the model parallel to the propagating waves and is used to illuminate equally a plane of the flow field as shown in Figures 5.46 and 5.47. In Figure 5.48, we see the light sheet through the water behind the breakwater model.

A major problem of flow visualization in the wave tank is connected with the seeding particles. We wanted some inexpensive particles since most of them are moved far away from the viewing area of interest under the wave's action or totally lost after a few minutes of operation. Moreover, the viewing area of interest was large and thus we wanted large enough particles to cover that area of observation. Moreover, their specific gravity should be around unity to insure neutral buoyancy. PLIOLITE VT resins were used to act as tracers of the motion of the fluid. They follow and capture the paths of flow particles. They are vinyl toluene/butadiene copolymers constructed by Good year. They came in a sack with different diameters. We sieved a big sample of them and we got particles with diameters ranging between 300 μm and

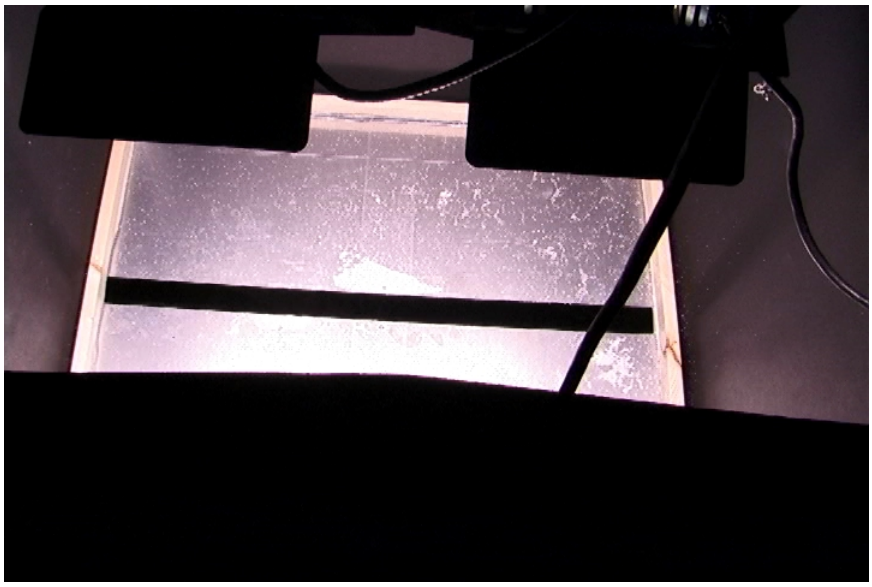

Figure 5.45: Light sheet generation setup.

1000 μm. We used particles only with diameters ranging between 420 to 500 μm. Because of the surface tension and the irregular surface of the particles, they did not suspend but rather floated when we dropped them in the water. Thus, before we used these particles, we mixed them with soap and shook them once in a while for two days in order to reduce the liquid film surface tension. Subsequently, we got rid of the soap, cleaning the particles with water. The temporal evolution of the flow was visualized from the reflection of the light on the surface of the suspended particles.

A DCR-TRV900 model Sony digital video camera recorder was used to capture the particle paths behind the breakwater model. The camera takes a fixed number of 30 frames per second. After several tests and tries we adjusted the exposure and shutter speed settings of the camera at a prescribed value in order to control the amount of light that gets into the camera. The exposure setting defines the size of the diameter of the diaphragm that stays open capturing a single frame. As for the shutter speed, which defines how fast the diaphragm opens and closes, we selected it to be 1/8 sec. Based on that value and the camera's fixed sampling frame rate of 1/30 sec, the camera refreshes the time frame history every four frames. With these settings, a particle that follows the flow is recorded as a streak rather than a single point. The camera was mounted on a tripod in the glass-walled observation pit, located approximately in the middle of the wave tank. It was placed normal to the light sheet plane and was used to acquire a series of

images, which represent the reflections of the particles in the flow. The viewing area of interest was approximately 25.4cm x 17.78cm (10in x 7in), as shown in Figure 5.49.

We propagate regular non-breaking incident waves of frequency 1 Hz at a water depth of 25 cm. The particles suspended in the water are recorded during one period of the motion. Figure 5.50 shows the time frame history with the streaks of the particles representing half of the trajectories of flow particles over $1/2sec$ total real time. Figure 5.51 shows the remaining part of the trajectories of flow particles over the remaining $1/2sec$ real time. Their trajectories are practically ellipses traversed clockwise, circular close to the free surface and flattened toward the bottom. As expected the velocity magnitudes decrease with depth. The direction of the flow locally and the decreasing velocity magnitudes are apparently compatible with the geometry of the hemi-cylindrical model. As shown in most of the Frames in Figures 5.50 and 5.51, the flow due to wave motion conforms with the circular geometry, yielding practically no flow separation. Thus, energy dissipation is mostly due to wave breaking and internal losses for the hemi-cylindrical model.

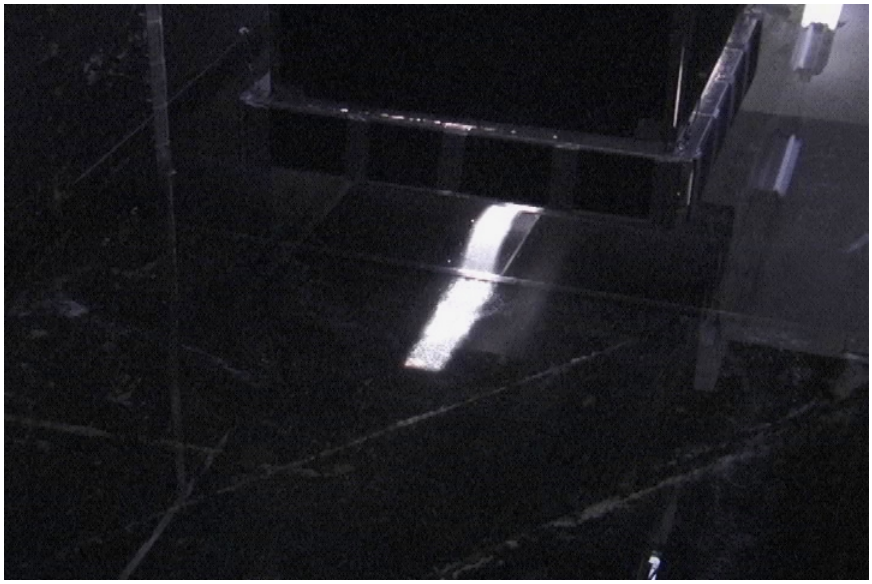

Figure 5.46: Light sheet in front of the second composite breakwater model.

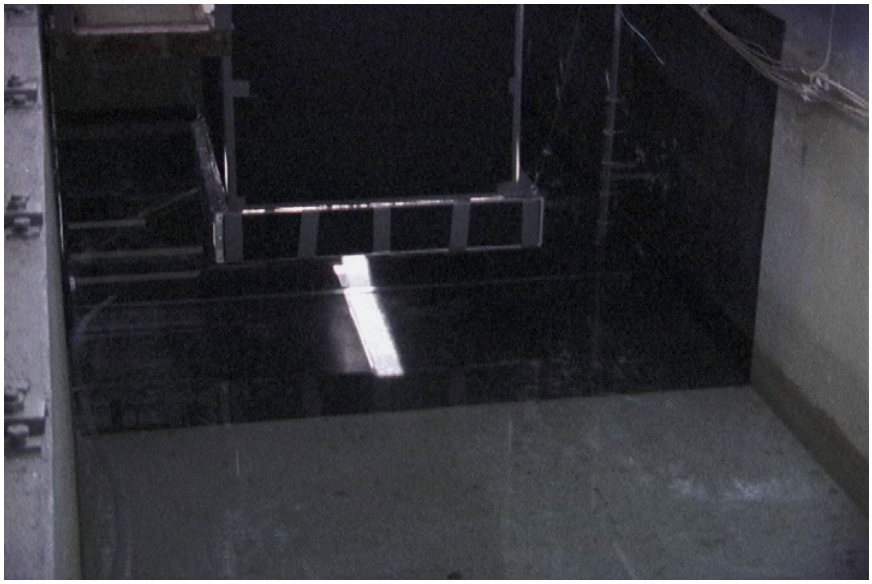

Figure 5.47: Light sheet behind the second composite breakwater model.

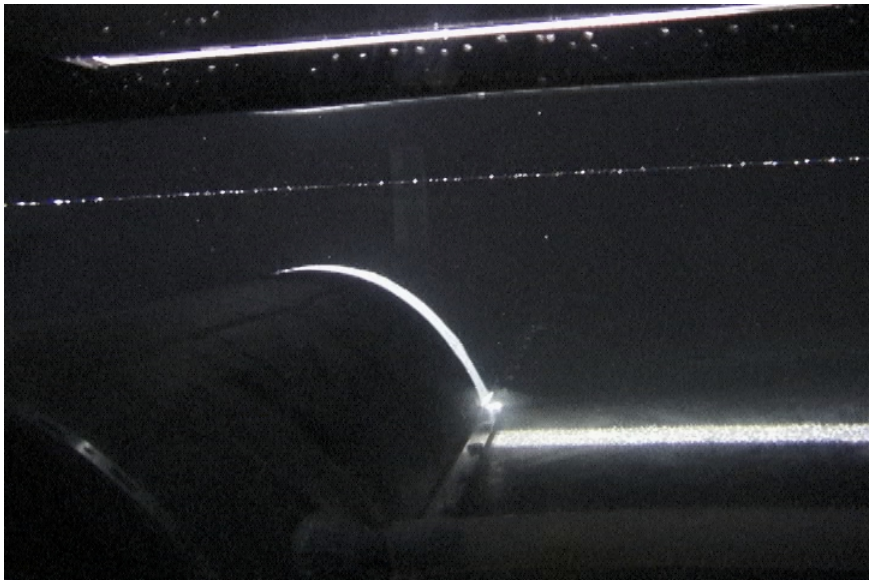

Figure 5.48: Light sheet through the water.

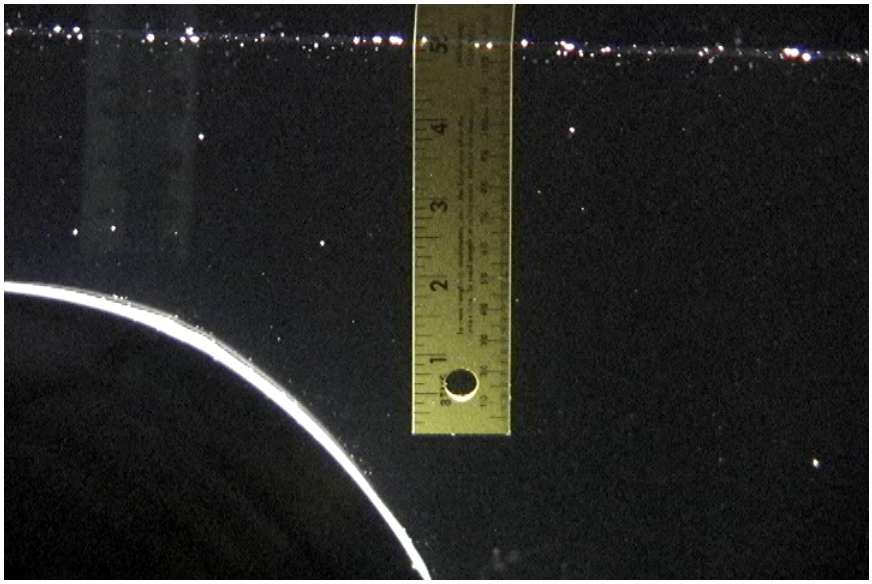

Figure 5.49: Area of interest behind and over the second composite breakwater model.

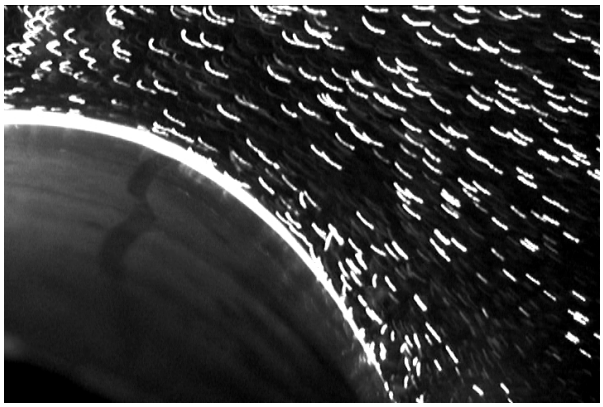

(a) Frame 1: $t = 0.125sec$

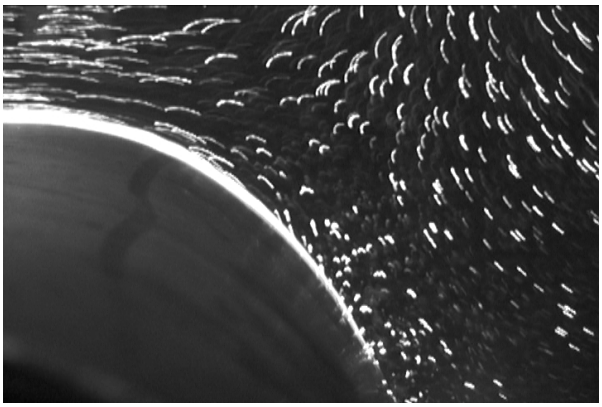

(b) Frame 2: $t = 0.25sec$

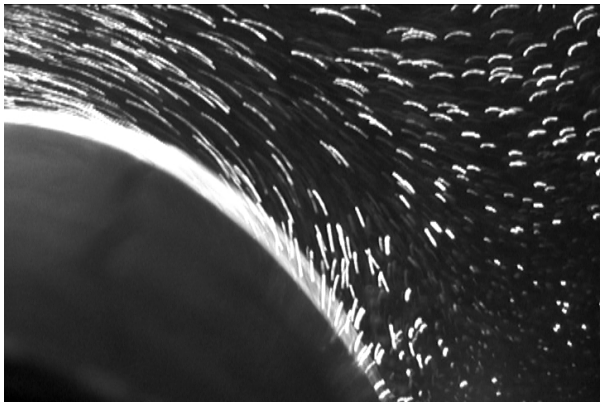

(c) Frame 3: $t = 0.375sec$

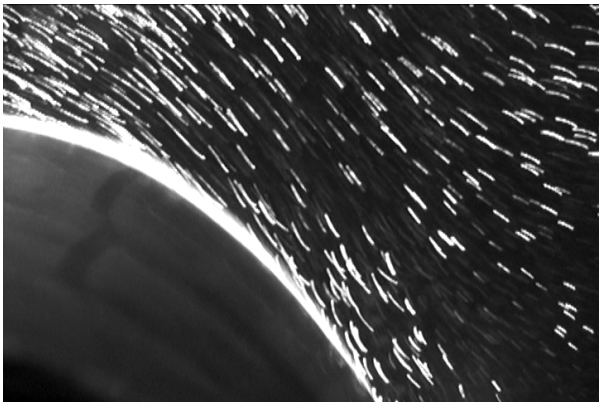

(d) Frame 4: $t = 0.5sec$

Figure 5.50: Particles' streaks behind and over the second flexible composite breakwater model over half period of 1 Hz wave.

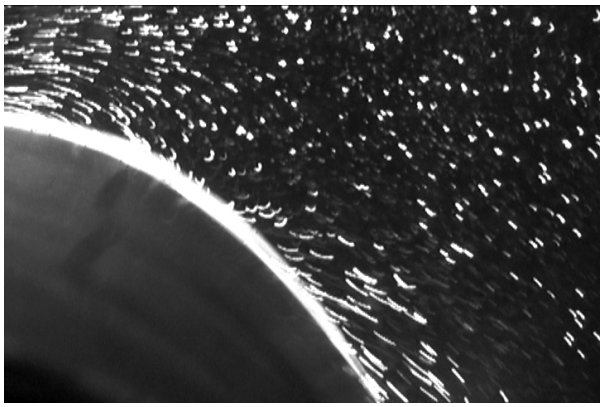

(a) Frame 5: $t = 0.625sec$

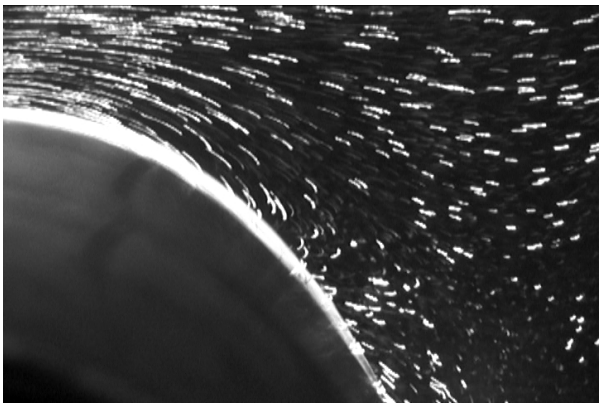

(b) Frame 6: $t = 0.75sec$

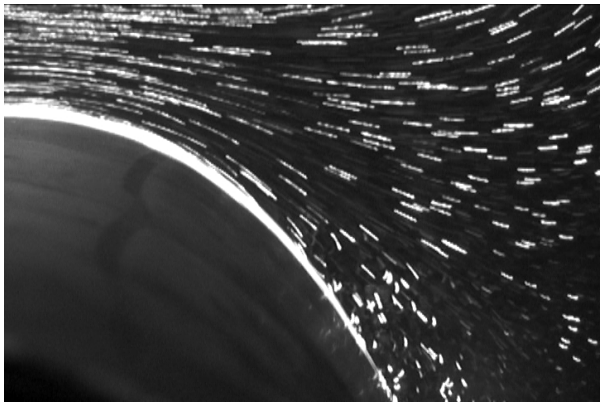

(c) Frame 7: $t = 0.875sec$

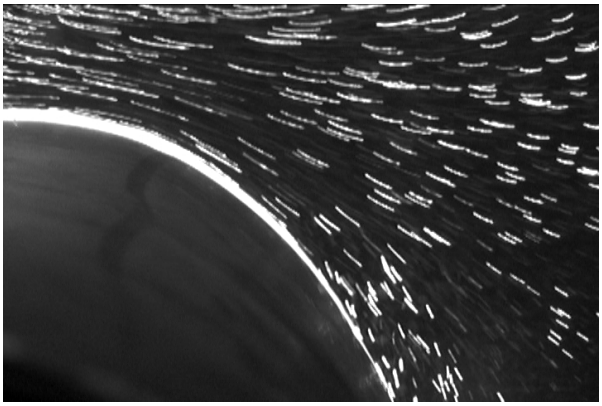

(d) Frame 8: $t = 1sec$

Figure 5.51: Particles' streaks behind and over the second flexible composite breakwater model over the remaining half period of 1 Hz wave.

5.5.4 Conclusions

By comparing again the average values of the wave coefficients for both models and all internal flexible composite models' pressures, it can be concluded that the lower submergence depth ratio, $z/h = 0.27$, causes higher wave reflection, lower wave transmission and higher energy loss than the high submergence depth ratio of 0.40. Analytically, the results show that for a submergence depth ratio of 0.27, rigid and flexible composite models with $y/h = 0.141$ and 0.282 transmit most of the wave energy. As for the flexible composite model with $y/h = 0.0.07$, most of the wave energy is reflected and the remaining almost equally transmitted and dissipated. For a submergence depth ratio of 0.40, most of the wave energy is transmitted for both breakwater models. Based on the order of the average values of transmission coefficient, C_t, and energy loss coefficient, C_L, for both submergence depth ratios, we can conclude that the flexible composite model with $y/h = 0.007$ and the rigid model are the most effective breakwaters. Moreover, this also indicates that the flexible composite models with $y/h = 0.141$ and 0.282 respond to the waves and behave as if they were even stiffer than the rigid model.

Based on the results, the variation in the wave steepness, H_i/L, influences most the variations of the wave reflection for both submergence depth ratios. This is most pronounced for the flexible composite model for all internal pressures as the wave steepness increases. The wave transmission varies significantly with the wave steepness only for the flexible composite model with $y/h = 0.007$ for both submergence depth ratios. According to the results of flow visualization technique, it was found that the flow over a hemi-cylindrical model is free of separation. However, when the model induces breaking of the wave, vorticity is generated which leads to energy dissipation and therefore attenuation of the transmitted wave.

Chapter 6

Conclusions and Recommendations

In the present work a new signal analysis procedure was developed to obtain accurately and conveniently reflection and transmission coefficients over breakwater models in laboratory studies. The method involves a fixed wave probe located ahead of the breakwater models to resolve the partial-standing wave into incident and reflected wave components and thus to estimate the reflection coefficient. The continuous Morlet wavelet transform is used. The reliability of using wavelet analysis to separate a partial-standing wave into incident and reflected wave components was verified by a numerical example. It was also verified by the small variance in the estimates of the incident wave height from independent experimental measurements. Wavelet analysis offers a further advantage. It is not constrained to linear wave theory or Stokes' 2nd order wave theory since we are not using the linear wave dispersion relation to estimate the wave number k. The wavelet analysis can thus provide more accurate estimates of reflection and transmission coefficients for finite amplitude incident waves, which theoretically are covered by higher order wave theories.

To carry out the present work, a wide variety of wave conditions and different models were employed. The main findings of the present effort are summarized below.

In suspended flexible sack model studies it was found that most of the wave energy is transmitted, some is dissipated and the smallest portion is reflected for all submergence depth ratios examined. The performance of the flexible sack breakwater model becomes more effective (i.e., gives lower wave transmission) as the submergence depth ratio decreases. For the case where

the flexible sack grazes the water surface, we observed and captured the formation of a mode of oscillation along the longitudinal direction, which leads to wave breaking. The importance of wave breaking, which leads a great proportion of wave energy to turbulent dissipation, is emphasized by the fact that minimum transmission is not achieved when reflection is maximum but when energy loss is at its peak.

The performance of the bottom-mounted breakwater models increases as the submergence depth ratio decreases. The rectangular breakwater models gave the highest energy loss coefficients resulting in reduction of wave transmission among all the bottom-mounted breakwaters, as shown in Table 6.1 for the rigid models and in Table 6.2 for the flexible models at lower pressure. For all the bottom-mounted breakwaters, the lowest pressurized flexible models are the most effective to reduce the transmitted wave height basically through energy dissipation. For all the lowest pressurized flexible hemi-cylindrical breakwater models, an optimum model width to wave length ratio, b/L, of 0.30-0.40 is achieved depending upon the submergence depth ratio, z/h. The variation in wave steepness influences mostly the wave reflection. The flow visualization technique indicated that the flow conforms with the circular geometry of a hemi-cylindrical breakwater model, yielding no flow separation. Thus, energy dissipation is mostly due to wave breaking and internal losses for the hemi-cylindrical breakwaters.

Table 6.1: Average wave coefficients of rigid bottom-mounted models.

	Water depth (h), [cm]	z/h	C_r	C_t	C_L
Rectangular	22.5	0.24	38%	64%	63%
Hemi-Cylindrical	22.5	0.27	40%	72%	55%
Rectangular	27.5	0.38	40%	69%	57%
Hemi-Cylindrical	27.5	0.40	24%	78%	55%

The following recommended research is the natural continuation of the present work and would significantly contribute to deeper understanding of the phenomena discussed here.

Apply wavelet analysis to non-linear harmonic terms in progressive waves. Extend experimental investigation to irregular water waves which simulate the real situation of the ocean. Perform flow visualization and particle image velocimetry (PIV) techniques to study the interaction

Table 6.2: Average wave coefficients of flexible bottom-mounted models at lower pressure.

	Water depth (h), [cm]	z/h	y/h	C_r	C_t	C_L
Rectangular	22.5	0.24	0.007	32%	35%	87%
Hemi-Cylindrical		0.27		38%	54%	69%
1st Composite		0.27		44%	57%	60%
2nd Composite		0.27		59%	54%	56%
Rectangular	27.5	0.38	0.007	29%	51%	79%
Hemi-Cylindrical		0.40		38%	61%	66%
1st Composite		0.40		41%	70%	54%
2nd Composite		0.40		43%	71%	51%

phenomena of the rigid and flexible rectangular breakwater models with water waves, since they cause a great proportion of the wave energy to dissipate. In studying a device that is to be used as a breakwater, it would be a great idea to extend our experimental study and test one or more of the models mentioned above in the real random wave environment of the ocean. If we want to keep the size of the model relatively small, we can not operate in the ocean, but rather in a location that has similar, but smaller, waves.

Bibliography

[1] Abul-Azm, A. G., "Wave Diffraction Through Submerged Flexible Breakwaters", *Ocean Engineering*, Vol. 23, No 5, pp. 403-422, 1996.

[2] Beji, S., and Battjes, J. A., "Experimental Investigation of Wave Propagation Over a Bar", *Coastal Engineering*, Vol. 19, pp. 151-162, 1993.

[3] Broderick, L. L., *Nonlinear Interaction of Water Waves and Deformable Bodies*, Ph.D Dissertation, Oregon State University, Corvallis, 1991.

[4] Broderick, L. L., and Leonard, J., "Selective Review of Boundary Element Modeling for the Interaction of Deformable Structures With Water Waves", *Engineering Structures*, Vol. 12, pp. 269-276, 1990.

[5] Broderick, L. L., and Leonard, J., "Nonlinear Water-Wave Structure and Interaction", *Computers and Structures*, Vol. 44, pp. 837-842, 1991.

[6] Broderick, L. L., and Jenkins, C. H., "Experimental Investigation of Fluid-Filled Membrane Breakwaters", *Journal of Waterway, Port, Coastal and Ocean Engineering*, Vol. 119, No. 6, pp. 639-656, 1993.

[7] Coastal Engineering Research Center (U.S.), *Shore Protection Manual*, 3rd Edition, Vol. 1, 1977.

[8] Dean, R. G., and Dalrymple, R. A., *Water Wave Mechanics for Engineers and Scientists*, World Scientific, Singapore, 1991.

[9] Dewi, F. D. E., *Three-Dimensional Analysis of Wave Attenuation by a Submerged, Horizontal, Bottom-Mounted, Flexible Shell*, MS Thesis, Virginia Polytechnic Institute and State University, Blacksburg, Virginia, 1997.

[10] Ertekin, R. C., and Becker, J. M., "Nonlinear Diffraction of Waves by a Submerged Shelf in Shallow Water", *Offshore Mechanics and Arctic Engineering Conference*, Vol. I, Part B, ASME, New York, pp. 31-39, 1996.

[11] Frederiksen, H. D., "Wave attenuation by Fluid-Filled Bags", *Journal of the Waterways, Harbors and Coastal Engineering Division*, ASCE, Vol. 97, No. WW1, pp. 73-90, 1971.

[12] Goda, Y., and Suzuki, Y., "Estimation of Incident and Reflected Waves in Random Wave Experiment", in *Proceedings of Coastal Engineering Conference*, Honolulu, Hawaii, Vol. 1, pp. 828-845, 1976.

[13] Ijima, T., Uwatoko, T., and Ushifusa, Y., "Wave Interception by Sea-Balloon Breakwater", *Memoirs of the Faculty of Engineering*, Kyushu University, Vol. 45, pp. 357-392, 1985.

[14] Ijima, T., Uwatoko, T., Ushifusa, Y., and Kojima, H., "Experiments on the Improvement of Wave Interception Effect of Sea-Balloon Breakwater", *Memoirs of the Faculty of Engineering*, Kyushu University, Vol. 46, pp. 193-206, 1986.

[15] Isaacson, M., "Measurement of Regular Wave Reflection", *Journal of Waterway, Port, Coastal, and Ocean Engineering*, Vol. 117, No. 6, pp. 553-569, 1991.

[16] Jenkins, C. H., and Leonard, J. W., "Transient Response of Wrinkled Viscoelastic Membranes", *Developments in Theoretical and Applied Mechanics*, Vol. 16, B. Antar et al., eds., University of Tennessee Space Institute, Tullahoma, TN, pp. II.13.16 - II.13.23, 1992.

[17] Jenkins, C. H., and Leonard, J. W., "Dynamic Wrinkling of Viscoelastic Membranes", *Journal of Applied Mechanics*, Vol. 60, pp. 575-582, 1993.

[18] Kaiser, G., *A Friendly Guide to Wavelets*, Birkhauser, 1994.

[19] Kee, S. T., and Kim, M. H., "Flexible Membrane Wave Barrier. I: Analytic and Numerical Solutions", *Journal of Waterway, Port, Coastal, and Ocean Engineering*, Vol. 122, No. 1, pp. 46-53, 1996.

[20] Kee, S. T., and Kim, M. H., "Flexible Membrane Wave Barrier. II: Floating/Submerged Buoy-Membrane System", *Journal of Waterway, Port, Coastal, and Ocean Engineering*, Vol. 123, No. 1, pp. 82-90, 1997.

[21] Liapis, S. I., Constantine, L. S., and Trowbridge, J. D., "On the Use of a Flexible Structure as a Breakwater", *Offshore Mechanics and Arctic Engineering Conference*, Vol. I, Pt. B, S. Chakrabarti et al., eds, ASME, New York, pp. 41-47, 1996.

[22] Mallayachari, V., and Sundar, V., "Wave Transmission Over Submerged Obstacles in Finite Water Depths", *Journal of Coastal Research*, Vol. 12, No. 2, pp. 477-483, 1996.

[23] Mansard, E. P. D., and Funke, E. R., "The Measurement of Incident and Reflected Spectra using a Least Squares Method" in *Proceedings of 17th Coastal Engineering Conference*, Vol. 1, pp. 154-172, 1980.

[24] Mays, T. W., *Three-Dimensional Analysis of Moored Cylinders Used as Breakwaters*, MS Thesis, Virginia Polytechnic Institute and State University, Blacksburg, Virginia, 1997.

[25] Milgram, J. H., "Forces and Motions of a Flexible Floating Barrier", *Journal of Hydronautics*, Vol. 5, No. 2, pp. 41-51, 1971.

[26] Ohyama, T., Tanaka, M., Kiyokawa, T., Uda, T., and Murai, Y., "Transmission and Reflection Characteristics of Waves Over a Submerged Flexible Mound", *Coastal Engineering in Japan*, Vol. 32, pp. 53-68, 1989.

[27] Rey, V., Belzons, M., and Guazzelli, E., "Propagation of Surface Gravity Waves Over a Rectangular Submerged Bar", *Journal Fluid Mechanics*, Vol. 235, pp. 453-479, 1992.

[28] Ripken, J., "Evaluation Studies of the United States Rubber Company Wave Blanket and Wave Trap", *Project Report* No. 62, St. Anthony Falls Hydraulic Laboratory, University of Minnesota, Minneapolis, MN, 1960.

[29] Stamos, D. G., Lusk, C. P., Hajj, M. R., and Telionis, D. P., "Wavelet Analysis of Reflection and Transmission Characteristics of Submerged Flexible Breakwaters", in *Proceedings of the 3rd ASME/JSME Joint Fluids Engineering Conference*, July 18-23, San Francisco, 1999.

[30] Tanaka, M., Ohyama, T., Kiyokawa, T., Uda, T., and Omata, A., "Wave Control by Flexible Underwater Mound" in *Proceedings of the 22nd Annual Offshore Technology Conference*, Houston, Texas, Vol. 3, pp. 551-558, 1990.

[31] Tanaka, M., Ohyama, T., Kiyokawa, T., Uda, T., and Omata, A., "Characteristics of Wave Dissipation by Flexible Submerged Breakwater and Utility of the Device", *Coastal Engineering 1992*, B. L. Edge, edr, ASCE, New York, Vol, 2, pp. 1613-1624, 1992.

[32] Teolis, A., *Identification of Noisy FM Signals using Non-Orthogonal Wavelet Transforms*, SPIE, Vol. 3078, pp. 590-601, 1997.

[33] Thompson, G. O., Sollitt, C. K., McDougal, W. G., and Bender Jr., W. R., "Flexible Membrane Wave Barrier", in *Proceedings of ASCE Conference on Oceans*, New York, pp. 129-148, 1992.

[34] Thornton, E. B., and Calhoun, R. J., "Spectral Resolution of Breakwater Reflected Waves", *Journal of the Waterways, Harbors and Coastal Engineering Division*, in *Proceedings of ASCE*, Vol. 98, No. WW4, pp. 443-460, 1972.

[35] Wiegel, R. L., Shen, H. W., and Cumming, J. D., "Hovering Breakwater", *Journal of the Waterways and Harbors Division*, ASCE, Vol. 88, No. WW2, pp. 23-50, 1962.

[36] Williams, A. N., "Dual Floating Breakwaters", *Ocean Engineering*, Vol. 20, No. 3, pp. 215-232, 1993.

Vita

Dimitrios G. Stamos

Dimitrios Stamos was born on May 15, 1971 in Athens, Greece. He was awarded a Bachelor of Science degree with distinction in Mechanical Engineering from *National Technical University of Athens* in October of 1995. At the same university he carried out research work in the field of fluid mechanics under the supervision of Prof. Spyros Voutsinas until May of 1996. After working at the *Center for Renewable Energy Sources* in Athens as a research assistant, he enrolled at *Virginia Polytechnic Institute and State University* as a doctoral student of Engineering Mechanics in August 1996. He received the degree of Master of Science of Engineering Mechanics in May 1998. He received the degree of Doctor of Philosophy of Engineering Mechanics in May 2000.